Int. J. Advanced Design and Manufacturing Technology, 2024, Vol. 17, No. 1, pp. 1-6

DOI: 10.30486/admt.2021.1908801.1217 ISSN: 2252-0406 https://sanad.iau.ir/journal/admt

Fabrication, Testing and Analysis of Composite Lattice Panels Under Three-Point Bending Load

Mahdi Farhadi
Department of Mechanical Engineering, Malek Ashtar University of Technology, Tehran, Iran
E-mail: farh14@yahoo.com

Ali Davar
Composite Research Centre, Malek Ashtar University of Technology, Lavizan, Tehran, Iran
E-mail: davar78@gmail.com

Mohsen Heydari Beni
Department of Mechanical Engineering, Malek Ashtar University of Technology, Tehran, Iran
E-mail: mohsenheydari1371@gmail.com

Jafar Eskandari Jam*
Composite Research Centre, Malek Ashtar University of Technology, Lavizan, Tehran, Iran
E-mail: jejaam@gmail.com, eskandari@mut.ac.ir
*Corresponding author

Received: 7 September 2020, Revised: 26 January 2021, Accepted: 22 February 2021

Abstract: Thanks to their high strength-to-weight ratio, lightweightness, and excellent energy absorption, composite lattice panels can be used in the aerospace, marine, automotive, and other industries. These structures can be used as an alternative to string-reinforced structures, honeycomb (core) sandwich panels, and aluminum grid structures. In this paper, a composite lattice panel is first fabricated from glass/epoxy by hand lay-up method using a silicon rubber mold. In this method, a Kagome composite lattice panel with twelve layers of resin-impregnated fibers was fabricated during a continuous process. After fabrication, the test panel was shown under three-point bending and failure modes. Also, a numerical simulation of three-point bending was performed in ABAQUS software. Then, the simulation results were compared with those of the experimental test, indicating a good convergence between the experimental test results and the finite element ones up to the point of failure. Due to changes in directions of force, these structures have a high ability to withstand damage, and therefore, continue to withstand the load after the failure of one or more ribs. Also, there is no sudden and sharp drop in the load-bearing capacity of the structure despite the force being maximized, which can be attributed to the high energy absorption of such structures. Instead, the force decreases slowly with fluctuations, and the structure continues to absorb energy until final failure. Therefore, such lightweight structures can be used in applications where energy absorption is of great importance.

Keywords: Composite Lattice Panel, Glass/Epoxy, Numerical Analysis, Three-Point Bending Test

Biographical notes:* *Mahdi Farhadi *received his MSc in Mechanical Engineering from the University of Malek Ashtar. His field of research is the mechanical analysis of composite materials.* ***Ali Davar*** *is currently an Assistant Professor at the Department of Mechanical Engineering, at Malek Ashtar University, Tehran,*

Research paper

Iran. His current research interests include composite manufacturing and composite structures. ***Mohsen Heydari Beni*** *is currently a PhD student at Malek Ashtar University and his main research interests are composite structures, plates and shell analysis, and nanomechanics.* ***Jafar Eskandari Jam*** *is a Professor of Mechanical Engineering at Malek Ashtar University Tehran, Iran. His current research focuses on composite structures, plates and shell analysis and nanomechanics.*

1 Introduction

The properties of composites depend on various factors, such as the type and percentage of ingredients, the shape and arrangement of the reinforcement, and the connection of the components to each other. Thanks to benefits such as high specific strength, lightness, and corrosion resistance, composite lattice structures are widely used today in the aerospace, missile, and marine industries. A lattice composite structure is created by connecting the composite ribs that form a continuous two-dimensional (or plate-like) or three-dimensional (or spatial) set. This set of ribbons (or ribbons) turns a structure into a lattice, consisting of continuous, tough, rigid, and strong fibers. Therefore, composite lattice structures have more applications than metal structures due to their high strength, lightweight ratio, and design flexibility. The main part of lattice structures is the lattice part, which is made of a series of very thin strips called ribs. The fibers in the ribs must maintain their strength and cohesion. Also, the layers in the ribs should not lose their alignment. Composite lattice panels can be used in structures where stiffness, strength, lightness, and energy absorption are important [1].

For example, composite lattice panels can be used in the bed of solar cells, most of which are now made of aluminum honeycomb with graphite/epoxy coating [2]. Solar cell panels must meet the minimum structural stiffness requirements. The natural frequency is usually considered to be greater than the given value to ensure that the panel vibrations do not lead to a resonance phenomenon on the satellite. Isogrid composite panels are predicted to be more rigid than honeycomb structures at a certain weight [2]. Unlike honeycomb structures, isogrid structures do not have an intermediate core that prevents heat from flowing along the depth of the panel; Therefore, the temperature difference along the depth of isogrid lattice panels is much smaller than honeycomb panels [2]. Composite lattice panels can be used in applications where energy absorption is considered as an important parameter, including car doors and roofs [1] and [3]. For example, it is used on the roof of a Ford Tire (“Fig. 1”).

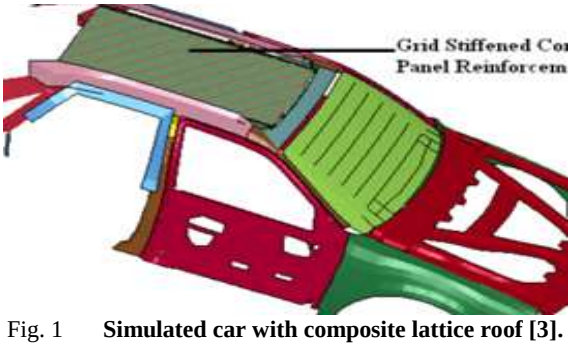

Fig. 1 **Simulated car with composite lattice roof [3].**

Thomas Kim (2000) [2], [4] investigated the method of construction and behavior of cylinders as well as composite lattice plates under compressive force. The results showed that ribs play a vital role in the buckling of these structures, which can withstand structural damage and also remain resistant to compressive forces following the failure of one or more ribs due to multiple load paths. Heibrich et al. [5] proposed two methods for constructing composite lattice structures using developed molds.

Gann and Gibson [6] analytically and experimentally investigated the energy

absorption in a composite lattice structure under transverse loading. The results of tests and simulations showed the excellent impact resistance of the mentioned structures and the highest energy absorption after the initial failure. It has also been observed that the maximum amount of force on the shell face is greater. On the other hand, the absorption of specific energy and displacement range is considerably larger if force is applied to the shell-less face. Fan et al. (2007) investigated sandwich panels with a carbon fiber-reinforced hexagonal lattice core [7]. Experimental results showed that the carbon-fiber-reinforced lattice structure is stiffer and stronger than foam and honeycombs. Ribs are required in at least three different directions to achieve shear strength of the lattice structure; Therefore, a hexagonal lattice structure can be considered as an optimal choice. Matiala conducted a comprehensive study on fabrication, analysis, and testing of composite lattice panels [8]. In this study, eight groups of panels were made, including multilayer, three groups of lattice panels with a different number of fiber bundles, stranded dry and then vacuumed, group 5, the sandwich panel with lattice core, group 6, shell-less panel, group seventh, the sandwich panel with a foam core, and the eighth group, foam without a shell. The results showed a higher impact resistance and a much more focused impact area of the lattice panel compared to the other panels. Prakash Jadaw also conducted a series of studies on increasing the performance of composite lattice plates under transverse loads, the results of which were published in 2007 [1]. The main purpose of this study was to optimize the geometry of lattice structures to increase the absorption of specific energy under a quasi-static and dynamic transverse impact. Fan et al. (10) investigated and compared the bending performance of carbon fiber sandwich composites with lattice core [9]. Ahmadi and Khalili (9) also investigated sandwich panels with lattice core under tensile load [10]. Numerical and laboratory results are compared to obtain a more desirable structure in terms of structural strength against bending and tension. Mahmoudi et al. (11) designed, fabricated, and tested lattice sandwich panels [11]. They were subjected to a three-point bending test to investigate their behavior against transverse quasi-static loads. According to the results of the practical test, the lattice core continued to withstand the load even after the procedures were exhausted, and no cracks were observed between the layers and the core due to the adhesion and proper processing of the resin. Also, it was found that the parameter of increased strength is affected by weight, mostly by changing the fiber material of the surfaces from glass to carbon and not by increasing the thickness of the surfaces.

This study first briefly reviews the method of constructing a composite lattice panel with a hexagonal structure. It is followed by a three-point bending test to evaluate the strength of the panel as well as a comparison between the experimental test results and the finite element results.

2 How to make composite lattice panel

Composite lattice structures can be fabricated using different methods, mainly on the type and material of the mold. Silicone molds are one of the best ways to make composite lattice panels because of the high thermal expansion of the silicone and the ability to easily separate it from the part. The silicone used as a silicone mold for the winding of lattice structures is RTV-2, which is a liquid and is baked in ambient air. To mold silicone, a mold is required to cast the silicon. For this purpose, a plexiglass mold was used (“Fig. 2”). It is made by a laser cutting method and has high dimensional accuracy.

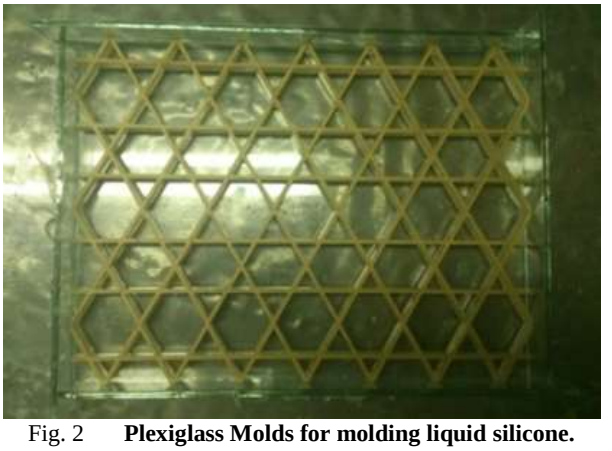

Fig. 2 **Plexiglass Molds for molding liquid silicone.**

After the mold is ready for silicone casting, the silicone and its hardener are mixed in 100 to 3.5 ratios with an industrial mixer for 10 minutes. Twenty-four hours after casting in a silicone mold, the liquid silicone was cured at room temperature and prepared for fiber spinning. Figure 3 shows the final silicone mold after leaving the plexiglass mold.

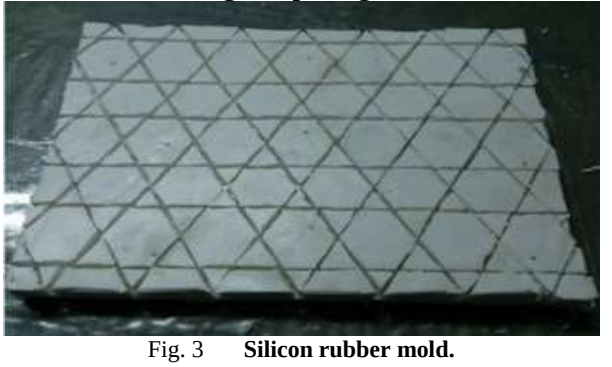

Fig. 3 **Silicon rubber mold.**

The composite lattice panel was fabricated using S-type glass fibers and Araldite LY556 epoxy resin. For this purpose, the fibers were first impregnated with resin in a resin bath and then guided into silicone mold grooves for threading. Twelve layers of fibers are used continuously to fill the silicone mold. The pins embedded in the four sides of the silicone mold were used in the direction of the mold grooves to guide the fiber path. Figure 4 shows the silicone mold filled with fibers and ready for baking. After the grooves were filled, a Teflon strip was placed on the piece, followed by a heavy steel plate so that the fibers were on top of each other, and the resin was spread evenly [5]. Then, an autoclave was used for baking the panel. The filled silicone mold was placed in the autoclave for baking for 4 hours at 80 degrees and 3 hours at 140 degrees. After baking, the lattice panel was removed from the autoclave. The excess was then cut using a composite saw, and finally, the lattice panel and silicone mold were pulled out.

3 Properties of materials

After the samples were fabricated and tested, the volumetric percentage of fibers was measured using the ASTM D2584 combustion test, which was 39%. After determining the volumetric percentage of fibers and the properties of the fibers and resins used, the longitudinal elastic properties and Poisson's ratio were obtained by the law of mixtures and the transverse and shear properties using the Halpin-Tsai equations. “Table 1” shows the properties of the ribs.

Table 1 The elastic properties of ribs

c (kg/m3)ρ	1638
Vf (%)	39
E1(GPa)	22.05
E2=E3(GPa)	7.63
G12=G13(GPa)	2.37
G23(GPa)	3.13
13ν=12ν	0.29
23ν	0.22

Table 2 Strength properties of ribs

SL+(MPa)	645
SL-(MPa)	2038
ST+(MPa)	54
ST-(MPa)	130
SLT(MPa)	46

Also, the strength of the composite was obtained using the micromechanical method, with the results shown in Table 2. Notably, a higher volumetric percentage of fibers does not necessarily mean higher strength [12]. An increase in the volumetric percentage of fibers leads to increased stiffness, while an increase of more than 35% in the volumetric percentage of fibers leads to decreased strength [12]. The properties of ribs are highly dependent on the

parameters of the fabrication process, such as the tensile strength of the fibers, the viscosity of the resin, and the mold used to shape the ribs.

4 Quasi-static transverse loading test

The three-point bending test of the panel was performed using a 15-ton SANTAM universal testing device with an automatic pneumatic jaw. According to "Fig. 4", the two sidebars are fixed and fully attached to their bases, on which the panel is placed, and the third bar is located in the middle on the panel, connected to the upper jaw of the device, through its base. To provide quasi-static conditions, the movable jaw of the device, to which the center bar is attached, moves downwards at a displacement rate of 2 mm/min. The axis distance between the two supports is 255.86 mm, and the load is applied to the middle of the distance between the two supports.

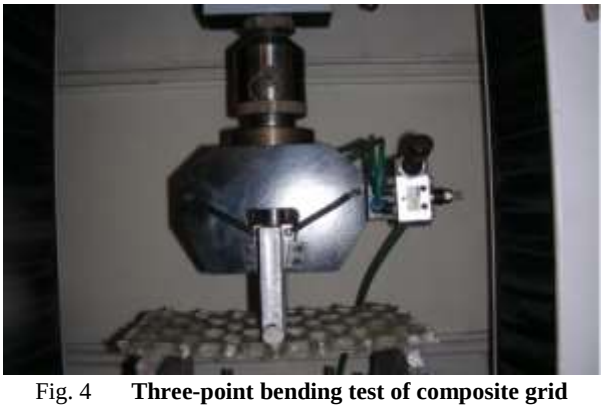

Fig. 4 **Three-point bending test of composite grid panel.**

5 Finite Element Analysis

For the finite element analysis of the composite lattice panel, the SC8R element was used in ABAQUS software, an eight-node linear hexahedral element. The number of elements used is equal to 12640. Figure 5 shows a view of the finite element model used in the analysis.

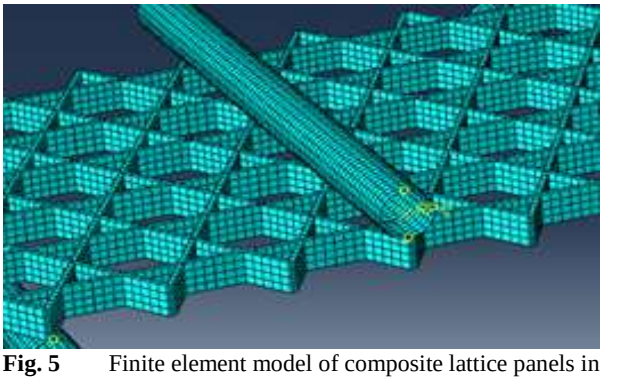

Fig. 5 Finite element model of composite lattice panels in three-point bending.

6 Test results

Figure 6 shows the force-displacement curve of a three-point bending test of a composite grid panel. The maximum force borne by the structure is 3156 N. At a displacement of about 35 mm, the test was stopped, but the structure continued to absorb energy. In this case, the structure failed to achieve complete failure (i.e., panel splitting).

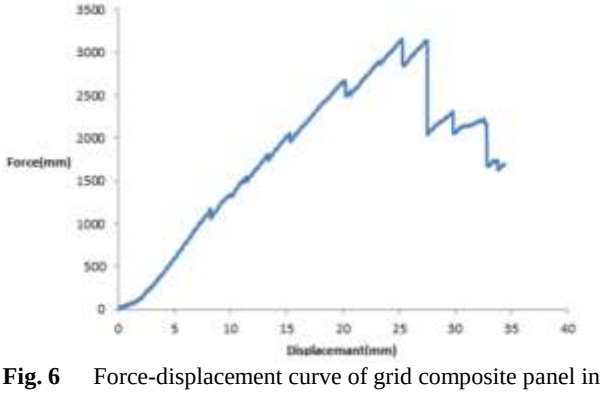

Fig. 6 Force-displacement curve of grid composite panel in three-point bending.

Composite lattice panels without shells have not been fabricated and tested yet. The panels that have been fabricated so far have all been in the form of sandwich structures with two shells and a lattice structure as the core or with one shell on one side of the panel. Deployment of forces on the side of the shell and ribs in these structures induces different behaviors at the maximum tolerable force and also shows the energy absorption of these structures [13]. The maximum force is obtained when force is applied to the shell and not to the ribs, while

more specific energy absorption is achieved by applying force to the ribs.

In the bending test of this fabricated specimen, the first crack sound was heard in the structure after a displacement of approximately 20-21 mm, characterized by a small drop in the curve shown in "Fig. 6". After this small drop, the force curve increased again to a displacement of about 25 mm. However, after this displacement, a sudden drop is observed in a displacement of about 27.5 mm, followed by intermittent oscillations in the curve [6]. Energy absorption continues until the final failure of the structure. As the force increases, the longitudinal tensile stress increases in the underlying layers, leading to their earlier failure compared to other layers ("Fig. 7").

Fig. 7 **Failure in bottom layers.**

Failure modes are different in compression mode. This assumption is proved by observing the difference in longitudinal tensile-compressive strength. As shown in "Fig. 8", the top layers of the panel fail due to the buckling of the fibers due to the longitudinal compressive stress. Nevertheless, the structure has continued to withstand the load after this failure, which occurred in several ribs, due to multiple force distribution paths [2]. Do and Rosen (14) defined the buckling of fibers in the bed of the matrix material as a state of rupture of these materials [14].

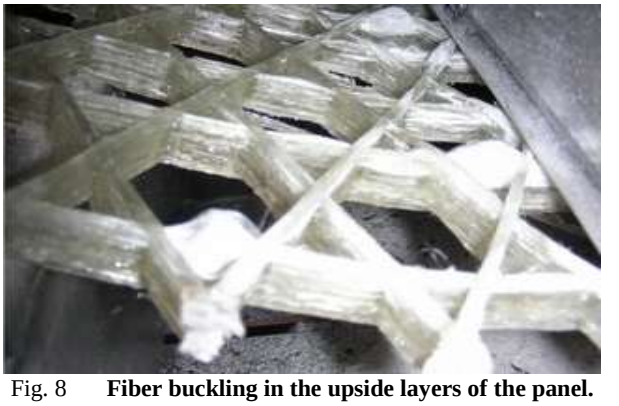

Fig. 8 **Fiber buckling in the upside layers of the panel.**

The final structural failure was not possible due to the limitations of the test device displacement and the maximum force exerted by the tolerance of the fixture.

7 Finite element test results

Figure 9 compares the experimental and finite element test results. As can be seen, there is a good convergence between the finite element test results and the experimental test results up to the point of failure, and the difference in the maximum load tolerance is 5.6%.

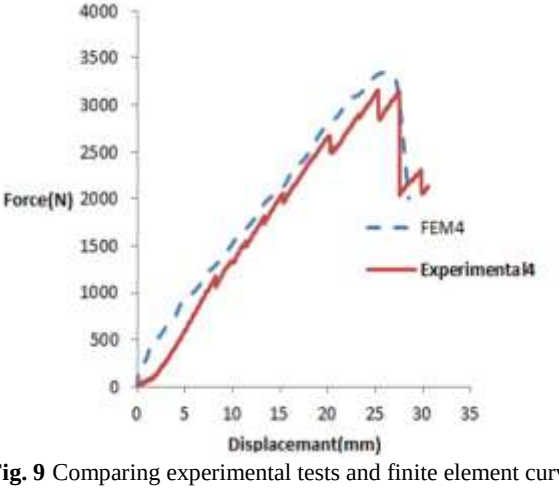

Fig. 9 Comparing experimental tests and finite element curve.

8 CONCLUSIONS

This paper examines composite lattice panels fabricated with S-Glass/epoxy under three-point bending. The main results are as follows:

1. Panels fabricated using silicone molds have very good rigidity and strength.
2. In a three-point bending load, the force decreases slowly and does not decrease sharply at once.
3. The failure process includes the failure of the lower layers of the panel under longitudinal tension and then the buckling of the fibers in the upper layers of the panel under longitudinal pressure. However, the structure continued to withstand the force after the failure of the multilayer fibers. Also, no cracks were observed between the layers.
4. There is an acceptable agreement between the results of finite element simulations and those of experimental tests, indicating the high capability of the software method in bending simulations with damage to the composite lattice structure.

References

[1] Jadhav, P., Mantena, P. R., Parametric Optimization of Grid-Stiffened Composite Panels for Maximizing Their Performance Under Transverse Loading, Composite Structures, Vol. 77, 2007, pp. 353-363.

[2] Kim, T. D., Fabrication and Testing of Thin Composite Isogrid Stiffened Panel, Composite Structures, Vol. 49, 2000, pp. 21-25.

[3] S. S. Shenoy, S. S., Energy Absorption of a Car Roof Reinforced with A Grid Stiffened Composite Panel in The Event of a Rollover, Wichita State University, 2006.

[4] Kim, T. D., Fabrication and Testing of Composite Isogrid Stiffened Cylinder, Composite Structures, Vol. 45, 1999, pp. 1-6.

[5] Huybrechts, S. M., Meink, T. E., Wegner, P. M., and Ganley, J. M., Manufacturing Theory for Advanced Grid Stiffened Structures, Composites Part A: Applied Science and Manufacturing, Vol. 33, 2002, pp. 155-161.

[6] Gan, C. Gibson, R. F., and Newaz, G. M., Analytical/Experimental Investigation of Energy Absorption in Grid-Stiffened Composite Structures Under Transverse Loading, Experimental Mechanics, Vol. 44, 2004, pp. 185-194.

[7] Fan, H., Meng, F., and Yang, W., Sandwich Panels with Kagome Lattice Cores Reinforced by Carbon Fibers, Composite Structures, Vol. 81, 2007, pp. 533-539.

[8] Muthyala, V. D., Composite Sandwich Structure with Grid Stiffened Core, M.Sc. Thesis, Louisiana State University, 2007.

[9] Fan, H., Yang, L., Sun, F., and Fang, D., Compression and Bending Performances of Carbon Fiber Reinforced Lattice-Core Sandwich Composites, Composites Part A: Applied Science and Manufacturing, Vol. 52, 2013, pp. 118-125.

[10] Ahmadi, T., Khalili, M., Analysis of Composite Sandwich Panels with Grid Stiffened Core Under Tensile Load, MSc Thesis, Department of Mechanical Engineering, Khajeh Nasir University of Technology (In Persian).

[11] Mahmoudi, Azarafza, R., and Davar, A., Design Manufacturing and Bending Testing of Composite Sandwich Panels Reinforced with Grid Core, In the 20th International Conference of Mechanical Engineering, 1393 (In Persian).

[12] Vasiliev, V., Barynin, V., and Rasin, A., Anisogrid Lattice Structures–A Survey of Development and Application, Composite structures, Vol. 54, 2001, pp. 361-370.

[13] Jadhav, P., Mantena, P. R., and Gibson, R. F., Energy Absorption and Damage Evaluation of Grid Stiffened Composite Panels Under Transverse Loading, Composites Part B: Engineering, Vol. 37, 2006, pp. 191-199.

[14] Dow, N. F., Rosen, B. W., Evaluations of Filament-Reinforced Composites for Aerospace Structural Applications, DTIC Document, 1965.

Int. J. Advanced Design and Manufacturing Technology, 2024, Vol. 17, No. 1, pp. 7-21

DOI: *ISSN: 2252-0406* *https://sanad.iau.ir/journal/admt*

A Quasi-Analytical Method Algorithm Development in Redesigning the Geometry and Structural Analysis of An Aircraft Propeller and Comparing with the Finite Element Method

Behrooz Shahriari *, Hassan Izanlo
Faculty of Mechanics, Malek Ashtar University of Technology, Iran
E-mail: shahriari@mut-es.ac.ir, Hassanizanlo1998@gmail.com
*Corresponding author

Nedasadat Seddighi
Mechatronic Sanaat Sepahan Co., Isfahan, Iran
E-mail: nsseddighi@gmail.com

Received: 12 October 2023, Revised: 26 November 2023, Accepted: 20 December 2023

Abstract: The aircraft propeller is effective in the performance of the aircraft propulsion system and must have acceptable structural strength. The complex aerodynamic geometry of the propeller makes its analysis more difficult. In this study, dynamic and aerodynamic stresses are calculated using the Finite Element Method (FEM). A structural analysis algorithm based on the quasi-analytical method is developed to evaluate the finite element analysis. In this regard, first, an algorithm is developed to redesign the propeller which performs in a way that by checking the dimensions, the geometry of the quasi-propeller is determined with the same mass and the coordinates of the center of mass. Then, different algorithms are developed to calculate the distribution of mass, moment of inertia, and the cross-section of the quasi-blade geometry. The calculation algorithms of rotational dynamic and aerodynamic stress distribution are developed. The results show that the FEM and the quasi-analytical method are well matched. In this study, the force equivalent to the thrust and the opposite force to the propeller rotation are placed instead of the aerodynamic pressure distribution. The comparison of the results obtained from the quasi-analytical method and the FEM indicates that the overall maximum stress of the system occurs at the root of the propeller and the maximum net stress due to aerodynamic forces occurs in the middle of the propeller geometry. According to the results, the rotational dynamic stress is much higher than the aerodynamic stress. It is also shown that the aerodynamic stress reduces the overall stress of the system.

Keywords: Aircraft Propeller, FEM Method, Stress Analysis, Structural Analysis Algorithm

Biographical notes: Behrooz Shahriari *received his BSc in Mechanical Engineering and MSc and PhD degrees in Aerospace Engineering from Malek Ashtar University of Technology in 2002, 2012, and 2016, respectively. His current research interests are structural optimization and artificial*

Research paper

intelligence. ***Hassan Izanlo*** *received his MSc in Mechanical Engineering from Sharif University of Technology in 2023. His current research interests are artificial intelligence, optimization, robotic nonlinear dynamics, and nonlinear vibration.* ***Nedasadat Seddighi*** *received her MSc in Aerospace Engineering from Malek Ashtar University of Technology. Her field of research is optimization and artificial intelligence.*

1 Introduction

Aircraft propeller, as a main part of the propulsion system, plays an important role in the performance of the aircraft. Today, with the advancement of aerodynamic, structure, and manufacturing technology sciences, aircraft designers are looking for propellers with high aerodynamic, propulsion, and structural efficiency, low weight and noise levels, and higher life and reliability. The airplane propeller is under aerodynamic and rotational dynamic loads. The structural study of this part of the airplane is of particular sensitivity and importance. The stress analysis of this part plays an important role in the overall design and reliability of the aircraft. In this regard, using an efficient method and accurate analysis is an important challenge. In a study, Yeh et al. [1] studied different stresses on the wind turbine blade. They used ANSYS software to analyse the blade stress. One of the deficiencies of their study is the large size of the mesh in the finite element analysis ("Fig.1-a"). According to the figure, a smaller mesh size should be adopted at the blade root. Based on experience, with the reduction of the mesh size, the stress undergoes many changes. In their study, the effect of blade weight is considered.

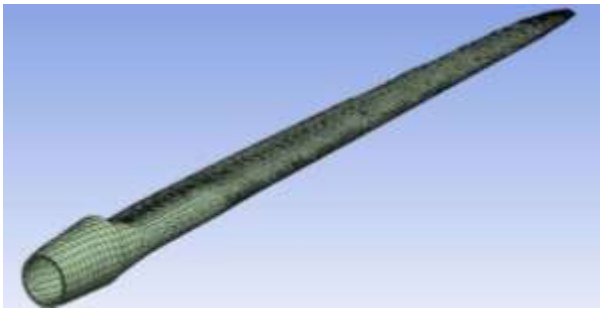

(a)

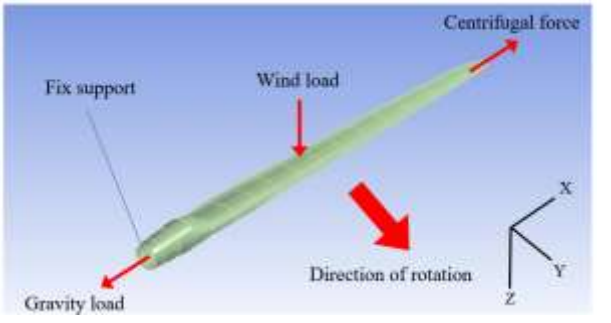

(b)

Fig. 1 **Airplane propeller: (a): system meshing, (b): different forces in stress analysis.**

The size of the wind turbine blades is large and they have a significant weight, and the stress caused by the weight is also important ("Fig. 1-b"), whereas the weight of the airplane propeller is much less and the stress caused by the weight is negligible. In wind turbines, the length of the blade and the surface area are such that the mass of the blade is very large and the stress caused by the weight becomes one of its important parameters. In their study, the maximum stress was 108 MPa. In many rotating equipment that deal with fluids, the maximum stress is at the blade root. In a study, Srivastava et al. [2] showed that for different vane states, the maximum stress is created at the root of the pump vane, and the stresses caused by the fluid pressure on the vanes usually have a small value. Wind turbines usually have the highest stress caused by fluid pressure among similar equipment. Because they have a long length and as a result, significant bending moments are created in the system. Also, due to having a significant surface area, very large aerodynamic forces are created. In another study, Wu and Yang

[3] studied the stresses created in a wind turbine blade. They showed that the stress caused by fluid pressure is equal to 57 MPa. Of course, in their model, this stress is created at a point with a high-stress concentration. This point is located at the root of the blade and many bending moments are created at this point. The amount of this stress is less in the airplane propeller because it has a shorter torque arm length. In another research, Doan et al. [4] obtained the stresses of a wind turbine blade by numerical method. They showed that the maximum stresses are near the blade root. Their finite element model had a large mesh size. They considered centrifugal forces, weight force, and aerodynamic forces. In another similar study, Yeh et al. [5] obtained the stress distribution in a 5 MW wind turbine blade. Also, in a study, Heo et al. [6] studied the structural stresses on a morphing wing airfoils with different internal structures such as honeycomb. They showed that there are stresses of about 270 MPa in the structure, which is significant. Di et al. [7] developed an algorithm for Aeroelastic analysis of horizontal wind turbines. The wind turbines do not have high speed.
In the mentioned studies, there is no suitable method for checking the accuracy of the results. Also, in many of them, there are some problems such as the large size of the element used in the analysis. This issue plays an important role in the final accuracy of the analysis. Also, a precise mathematical model is not used in these studies. The present study deals with the structural analysis of the propeller under rotational dynamic and aerodynamic loads. In this direction, a comprehensive algorithm for redesigning the quasi-propeller geometry and its structural analysis is developed.

2 Introducing the 3D model mathematical model

The three-dimensional model of the propeller has two main parts including the blade and hub and some side parts. Figure 2 shows the 3D model of the propeller. The material of the propeller blade and hub is 2014-T6 aluminium which is presented in “Table 1”. The mass of the rest of the parts which are located inside the hub is insignificant and 1.3 kg in total, and also applied as a point mass and the corresponding moment of inertia. The blade mechanical properties are presented in “Table 2”. The flowchart of FEM analysis is presented in “Fig. 3”.

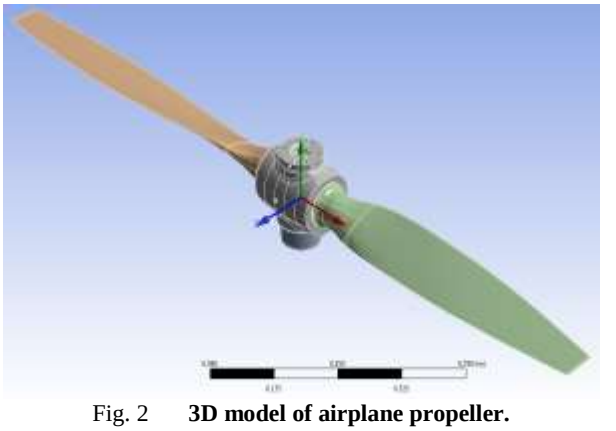

Fig. 2 **3D model of airplane propeller.**

Table 1 **Properties of 2014-T6 aluminum [8]**

Properties	**Value**
density	$2700\,Kg/m^3$
Elastic modulus	$70\,GPa$
Poisson's coefficient	0.33
yielding strength	414 MPa
ε_{P-Y}	0
σ_u	514 MPa
ε_{P-u}	2.08

Table 2 **The mechanical properties of the blade**

Properties	**Value**
Total mass	8.08 kg
Center of mass according to Fig. 2	
X	337.5 mm
Y	31.5 mm
Z	7.15 mm

Numerical modeling of rolling bearings and other propeller components is a difficult task. In many studies, fixed constraints are considered, but this issue makes the model far from reality. In this regard, the mathematical model of the propeller is extracted and analysed. Figure

4 shows the mathematical model of the propeller from two views. In the mathematical model, instead of mechanisms and bearings, equivalent springs are used. The symmetry of springing is respected to create mathematical stability. This work is done in such a way that two springs are applied between two surfaces instead of one spring.

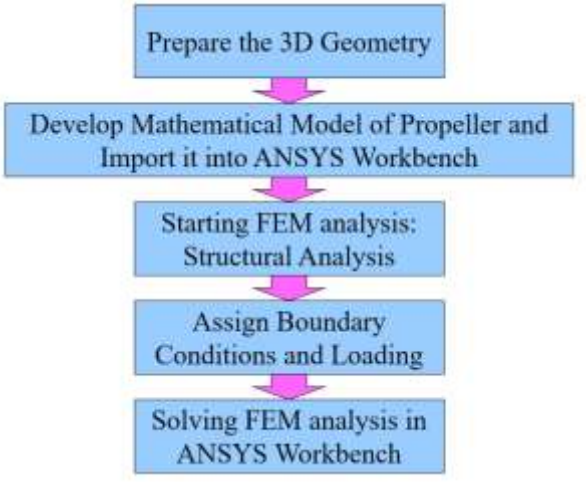

Fig. 3 **Structural Analysis of the blade using FEM.**

The stiffness of these two springs is half of the original spring. This process creates the closest model to reality. The equivalent stiffness of rolling element bearing is about 10^8 [9]. According to this model, the two surfaces of the blade and the hub can have relative movement. In the case of fixed constraint, relative motion is not applied. This work causes a sharp increase in the natural frequencies of the system and ultimately reduces the accuracy of the solution. The equivalent mass of the rolling bearing is also included in the mathematical model.

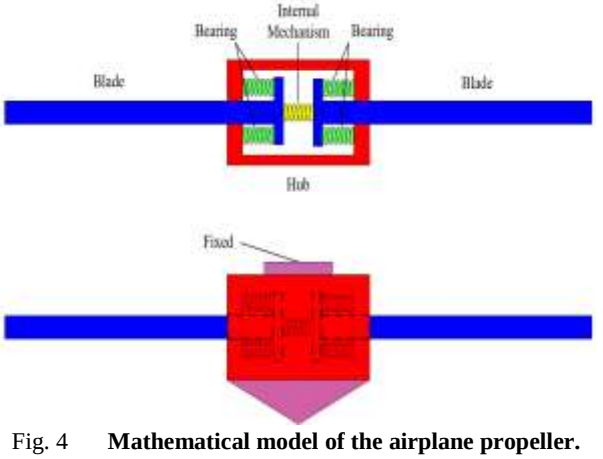

Fig. 4 **Mathematical model of the airplane propeller.**

3 Finite element modeling

Due to the complex geometry of the blade and hub, a tetrahedral element with 4 nodes and 12 degrees of freedom is applied to the system. The complex geometry should be segmented by partition. The blade cannot be partitioned and the hexahedral element cannot be used. The blade geometry is complex due to variable airfoil cross section and also the geometry is twisted. The blade presented in "Fig. 1" does not have any twisting. This element is the best element for sweeping complex geometries such as blades ("Fig. 5"). The elements with more nodes are used for engineering problems with large deformation. The blade structure does not have large deformation during its operation. Therefore, the tetrahedral with 4 nodes is acceptable.

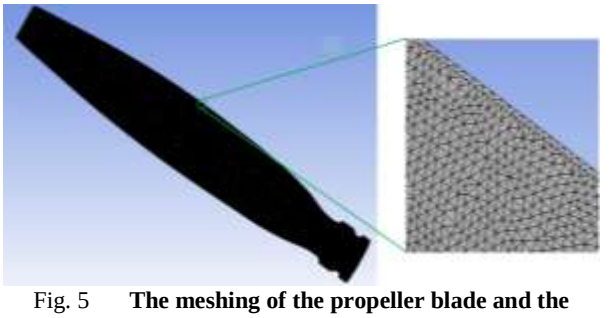

Fig. 5 **The meshing of the propeller blade and the enlarged view of its edge.**

Figure 6 shows the fully meshed propeller model. The element size in the full model of the airplane propeller is 1.026 mm. The mesh dependency study is continued till the computer system capacity and the final size are selected based on this subject. The complete specifications are shown in "Table 3".

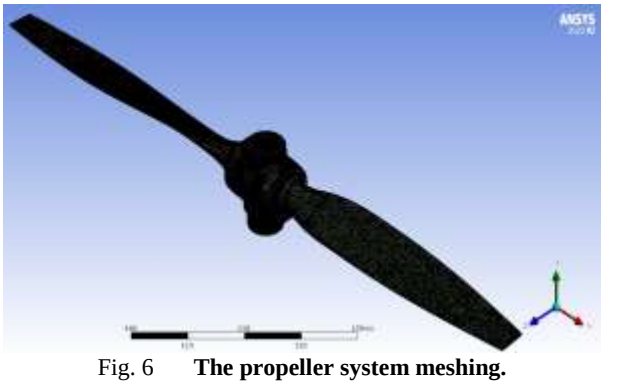

Fig. 6 **The propeller system meshing.**

Table 3 **The final specifications of the aircraft propeller meshing**

Mesh specifications	
Mesh type	Tetrahedron
Mesh size	1.026 mm
Number of degrees of freedom of element	4
Mesh characteristic	linear

Total number of elements	2755528
Total number of nodes	4718270

4 Stress analysis using the finite element method

The stress analysis of the propeller blade is performed based on the input information provided in "Table 4", which is obtained according to the aerodynamic analysis and the propeller user manual.

Table 4 **Input information for structural analysis**

Characteristic	Value
Maximum working rotational speed	2700 RPM
Maximum propulsion force (related to the maximum working rotational speed)	2073 N
Maximum pressure on the blade	200 KPa
Minimum pressure on the blade	100 KPa

The above information is entered into the finite element analysis. For example, the propulsive force is divided into two equal forces and applied to the propeller in the direction of the airplane's movement, and the opposing forces of the propeller rotation are applied to the system as shown in "Fig. 7", so that they are the closest to reality. To increase the reliability factor of the analysis, the forces entering the system are applied slightly more than the reported forces. Analyzing the aerodynamic force in the case of pressure distribution will be much longer. Figure 7 shows the loading and boundary conditions of the analysis. The ANSYS Workbench distributes load vectors across one or more topologies automatically. This option improves the reality of the problem-solving because the aerodynamics loading is distributed. The loading area (red zone) is shown in "Fig. 7" and the force is not concentrated.

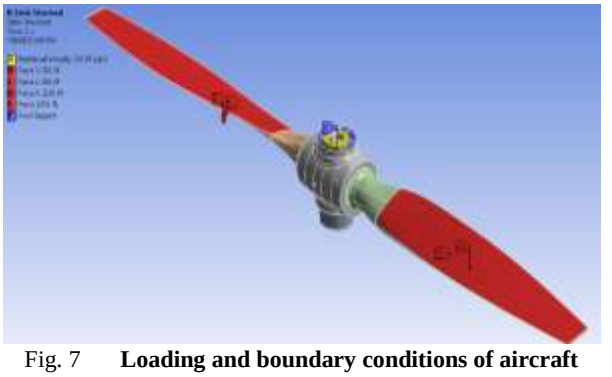

Fig. 7 **Loading and boundary conditions of aircraft propeller analysis**

Applying the rotational speed to solve will be in the form of D'Alembert. In this case, the dynamic problem is transformed into a static one, and its numerical solution will be much easier. The important point is that the propeller has different tensions at different rotational speeds and different working conditions.

The results of structural stress analysis including rotational dynamic and aerodynamic loads using the finite element method are shown in "Fig. 8". According to the figure, the maximum stress is at the blade root. The stress in the middle part of the blade also has a large value and the stress gradient between these two points is almost such that it reaches from one high value to another high value. Therefore, in terms of structure, the middle part of the blade is also of special importance. The tension in the root of the propeller is very high due to the presence of a small groove and the consequent increase in stress concentration. Also, drilling continues up to this part and reduces the resistant cross-sectional area.

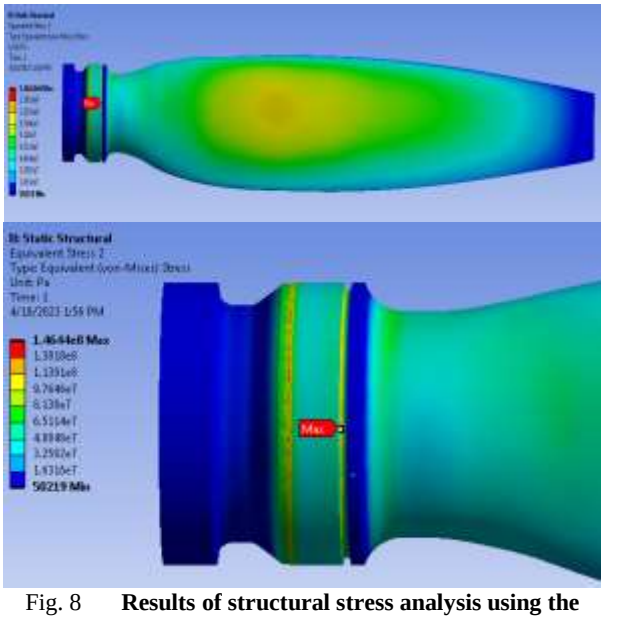

Fig. 8 **Results of structural stress analysis using the finite element method.**

To investigate the effect of rotational dynamic stress and aerodynamic stress, the finite element analysis of each is done separately. Figure 9 shows the rotational dynamic stresses and "Fig. 10" shows the aerodynamic stresses. According to the stress contour in "Fig. 9", the maximum stress of the structure under the rotational dynamic load is at the root of the blade and its value is slightly higher than the cumulative stress of the dynamic and aerodynamic loads. According to "Fig. 10", the maximum aerodynamic stress is in the middle of the blade. At this point, the blade thickness is low. In bending stress, in addition to the applied bending moment, the equivalent moment of inertia is also important. In the center of the blade, the equivalent moment of inertia is much less than the root of the

propeller. The reason for the greater aerodynamic bending stress in the center compared to the root is the same issue. The eccentricity of each cross-section also decreases with the distance from the center of the blade, which reduces the bending moment. This problem will also affect the bending stress created. According to the results of stress analysis, aerodynamic stress is opposed to rotational dynamic stress.

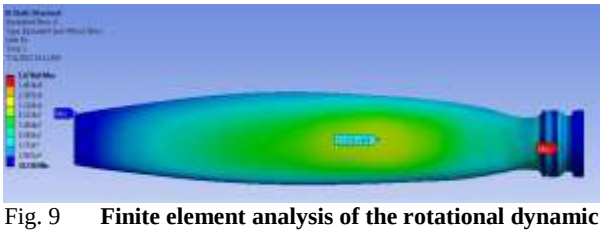

Fig. 9 **Finite element analysis of the rotational dynamic stresses.**

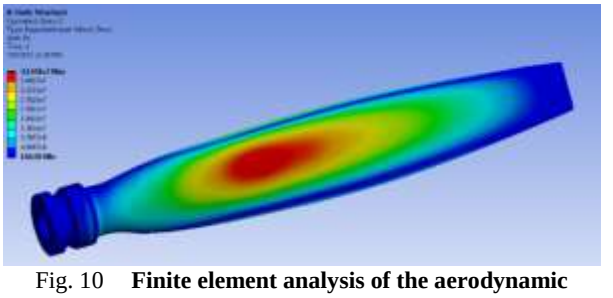

Fig. 10 **Finite element analysis of the aerodynamic stresses.**

To check the tension and its independence from the network and computer limitations, only the size of the blade element is reduced. Figure 11 shows changes in aerodynamic stress and "Fig. 12" shows changes in rotational dynamic stress according to element size. The variation of the stress in "Fig. 12" is negligible.

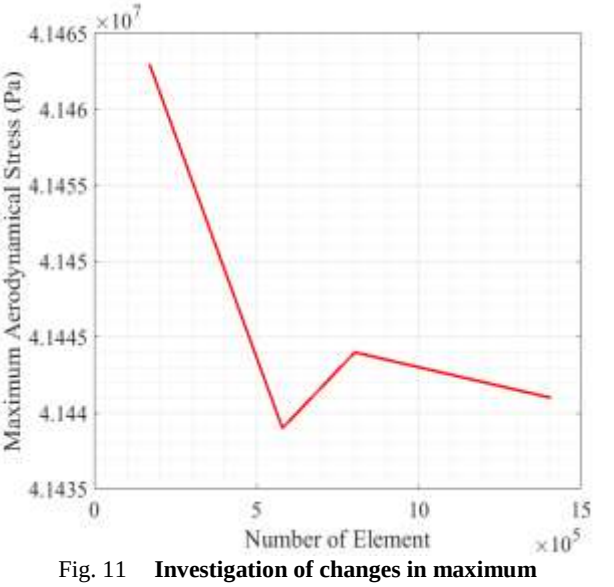

Fig. 11 **Investigation of changes in maximum aerodynamic stress according to the changes in the number of blade elements.**

The minimum value of stress is 158 MPa and maximum value is 168 MPa. This subject shows the convergence in the mesh dependency study.

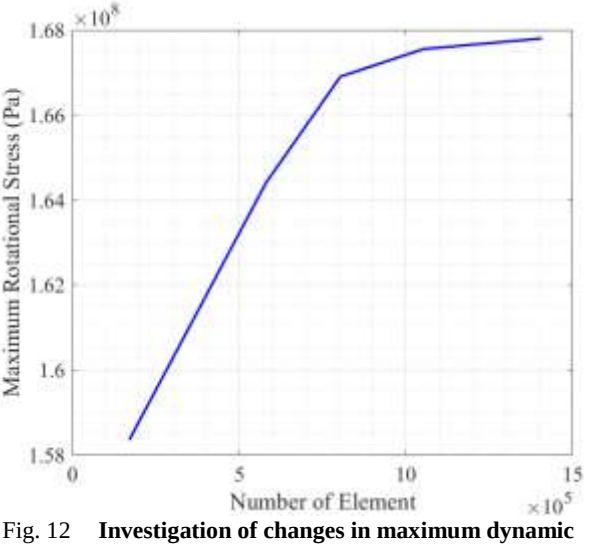

Fig. 12 **Investigation of changes in maximum dynamic rotational stress according to changes in the number of blade elements.**

5 DEVELOPMENTS of a quasi-analytical algorithm

5.1. Development of the Algorithm for Redesigning the Quasi-Propeller Geometry

Considering that the stress analysis by the quasi-analytical method requires having the closest geometry to the propeller to implement stress analysis algorithms,

a quasi-propeller geometry redesign algorithm is developed. The shape of the quasi-propeller system is shown in "Fig. 13".

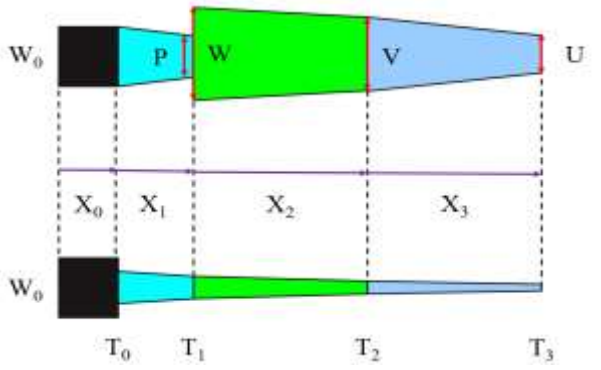

Fig. 13 **The shape of the quasi-propeller system.**

The performance of this method is in this way that a guess interval (such as [13.2-14.1] cm) is applied to the parameters shown in the figure with the help of 3D design software. During the algorithm, the algorithm is stopped by placing 2 numerical conditions of the total mass and the position of the center of mass. In the final selection of parameters, the most accurate mass and the most accurate center of mass will be the criteria. The range of all parameters is divided by a value of N. Therefore, the total number of design events will be equal to NM, where M is the total number of design parameters. The way the algorithm works is that it starts with the first component of the parameter X0 and with all the other components of the other parameters, the geometry is built and this work continues until the applied conditions are fulfilled. The exact mass and position of the center of mass lead to the calculation of the exact centrifugal force. The algorithm is presented in the appendix. Due to the presence of a hole in the root of the blade, in the X0 range, a certain amount of the equivalent area is reduced to fully match the reality.

5.2. Algorithms for Calculating Rotational Dynamic Forces and Stresses

5.2.1. Pure Rotational Forces and Stresses (Tensile Rotational Stress)

Due to the centrifugal force, the components of the propeller are thrown outwards. This problem causes rotational dynamic stresses in the system. The force of each element is calculated according to "Fig. 14". At any point of the blade, the dynamic equivalent stress without considering bending and in tension form is presented in "Eq. (1)".

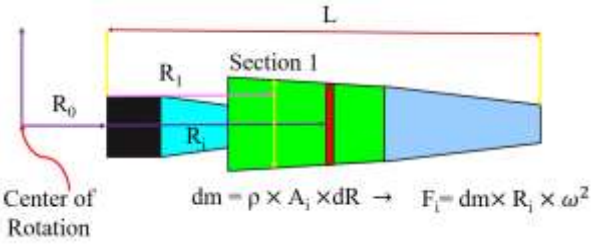

Fig. 14 **Calculating the centrifugal force of each element of the blade.**

$$\sigma_{Dy\,1Section1} = \frac{\int_{R_1}^{L} F_i}{A_{Section1}} = \frac{\int_{R_1}^{L} dm \times (R_i + R_0) \times \omega^2}{A_{Section1}} = \frac{\int_{R_1}^{L} \rho \times dR \times A_i \times (R_i + R_0) \times \omega^2}{A_{Section1}} \quad (1)$$

In this equation, ω is the rotational speed of the propeller, ρ is the metal density of the blade, σ is the stress, A is the cross-sectional area, L is the length of the blade, R_i is the distance of the element from the root of the propeller, and R_0 is the distance of the root from the rotation axis. The important point in the analysis is that the root of the propeller has an initial distance from the center of rotation, which is shown in "Fig. 15". In calculating the stress in the root of the propeller, the lower limit of the integral is set to 0. In the implementation of the main algorithm, SUM is used due to the discreteness of the calculations.

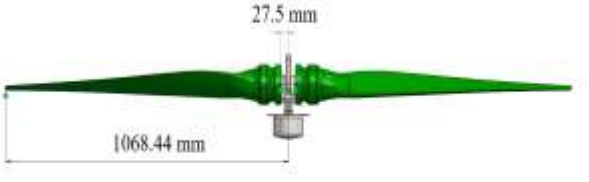

Fig. 15 **The distance between the root of the propeller and the center of rotation.**

5.2.2. Rotational Bending Forces and Stresses

In the previous step, the rotational dynamic net stress was calculated at each section, but each element has an eccentricity from the center line. In this case, an algorithm is

developed to calculate the center of mass of each element for two non-longitudinal directions of the propeller (X is the longitudinal direction of the propeller). First, the characteristics of the center of mass in the Y and Z directions are extracted from the design software. Now, assuming the linear changes of the center of mass, two initial guesses are made for both ends of the hypothetical line, and this process is repeated in so far as the eccentricity is equal to the results of the software ("Fig. 16"). The beginning of the propeller does not have an eccentricity due to its circular nature. In addition to the circular part, the elliptical parts also do not have an eccentricity, and only the parts that are in the shape of an airfoil have an eccentricity. Since the size of the airfoils decreases from the beginning to the end of the blade, these eccentricities lead to the creation of a bending moment, because each element is thrown outward at any point. These eccentricities act like torque arms. The calculation of rotational bending stress is given in "Eq. (2)".

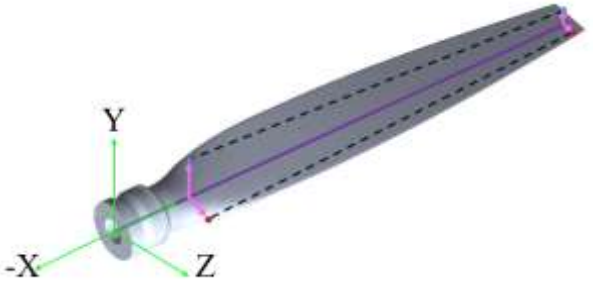

Fig. 16 **Determining the eccentricity of the blade elements.**

$$\sigma_{Dy\,2Section1} = \frac{Moment \times C}{I} = \frac{\int_{R_1}^{L} F_i \times E_i \times TWIST\,(i)}{\frac{I_{Section1}}{C_i}} = \frac{\int_{R_1}^{L} dm \times (R_i + R_0) \times \omega^2 \times E_i \times TWIST\,(i)}{\frac{I_{Section1}}{C_i}} \quad (2)$$

$$= \frac{\int_{R_1}^{L} \rho \times dR \times A \times (R_i + R_0) \times \omega^2 \times E_i \times TWIST\,(i)}{\frac{I_{Section1}}{C_i}}$$

In "Eq. (2)", *I* is equal to the moment of inertia of each sector of the propeller, *C* is the distance from the neutral axes and *TWIST* is the twist angle of the propeller. In each sector, the sum of the bending stresses caused by two eccentricities is added together.

5.3. Algorithm for Calculating Aerodynamic Stresses

One of the most important structural stresses of the blade is aerodynamic stress. In this study, an algorithm is developed to calculate aerodynamic stresses. The algorithm works in such a way that it calculates the pressure difference between the two sides of each element and converts it into the equivalent force of that element and by applying the distance, it becomes its bending moment. Equation (3) shows how to calculate the aerodynamic stress in a section of the propeller. The distribution of pressure will also be in a way that creates the equivalent force of the propulsion. Also, the pressure distribution is such that the maximum pressure is created at a certain distance from the end of the propeller.

$$\sigma_{AERO\,Section1} = \frac{Moment \times C}{I} = \frac{\int_{R_1}^{L} (P_1 - P_2) \times E_i \times TWIST(i) \times (R_i + R_0) \times dR}{\frac{I_{Section1}}{C_i}} \quad (3)$$

Equation (4) is also used to calculate the aerodynamic stresses against the rotational movement of the propeller.

$$\sigma_{AERO2Section1} = \frac{Moment \times C}{I} = \frac{\int_{R_1}^{L} (P_3 - P_4) \times E_i \times TWIST2(i) \times (R_i + R_0) \times dR}{\frac{I2_{Section1}}{C_i}} \quad (4)$$

5.4. Applying Stress Concentration Coefficients

A stress concentration coefficient should be applied to the root of the propeller, which has severe geometric changes and steps. Therefore, the algorithms are written in such a way that a stress concentration factor is applied to them. In the algorithm, a conditional order is executed that if the cross-section distance from the beginning of the propeller root is less than Z_0, the calculated bending stress values are multiplied by 2 and the tensile stress values are multiplied by 1.9. The cross-section area in the root of the propeller is minimum and also there is stress concentration. Figure 17 shows this subject.

6 Results of structural analysis by quasi-analytical method

In this part, the results of the stress analysis of the propeller are presented using the quasi-analytical method. Figure 18 shows the results. The results include the distribution of various structural parameters such as various rotational dynamic forces and moments, different aerodynamic moments, dynamic stresses, and aerodynamic stresses.

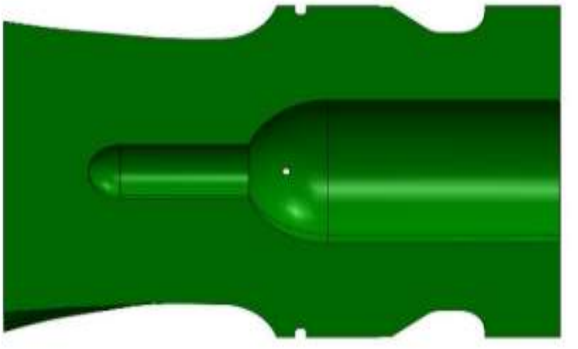

Fig. 17 **Root section of the propeller and cross section area reduction.**

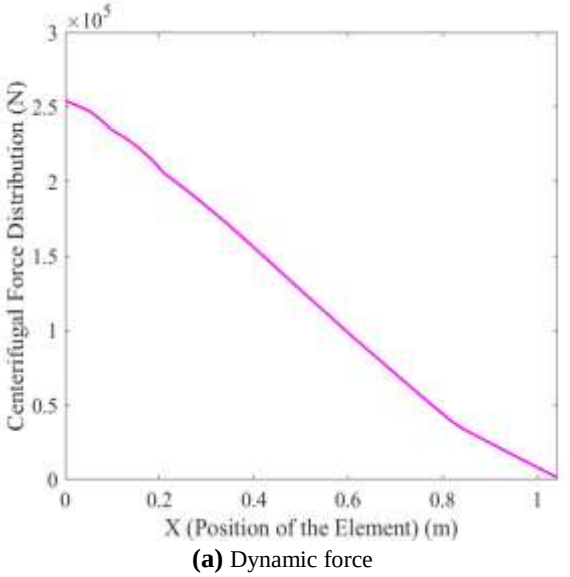

(a) Dynamic force

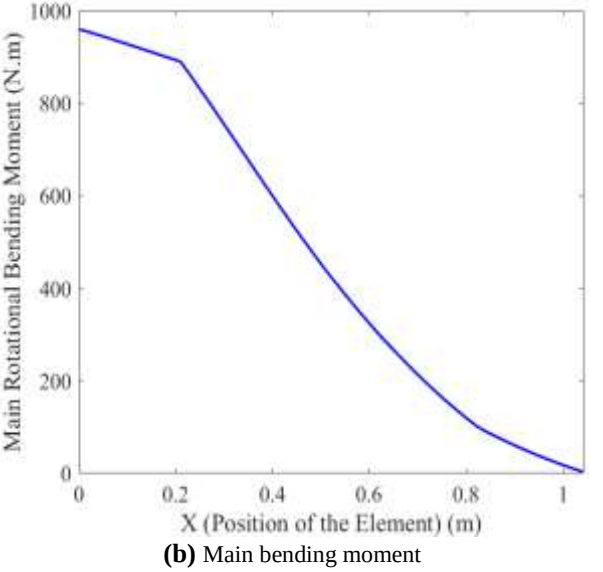

(b) Main bending moment

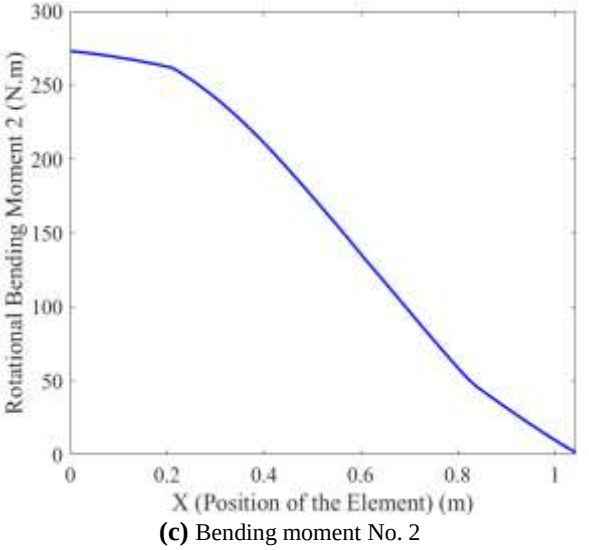

(c) Bending moment No. 2

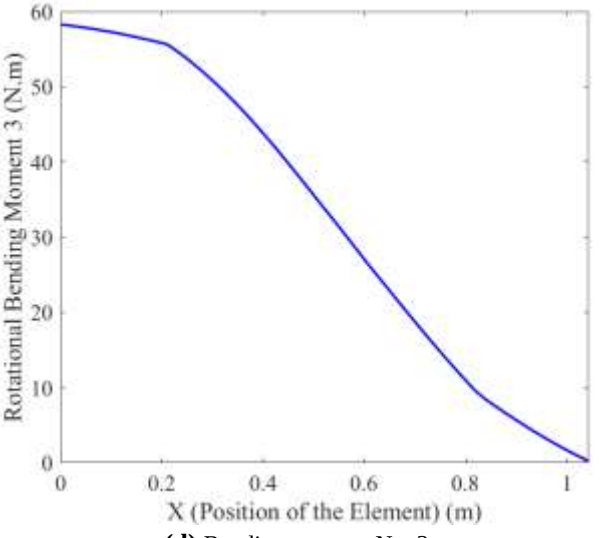

(d) Bending moment No. 3

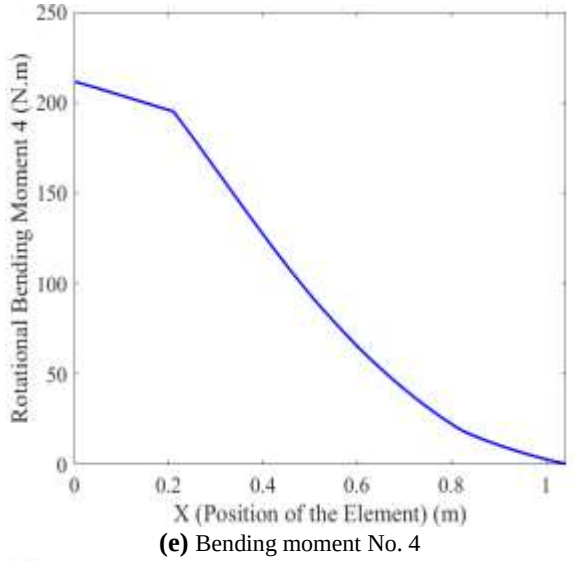

(e) Bending moment No. 4

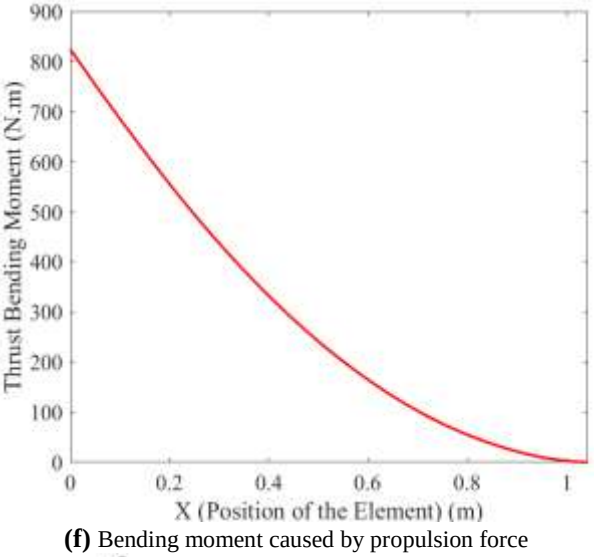

(f) Bending moment caused by propulsion force

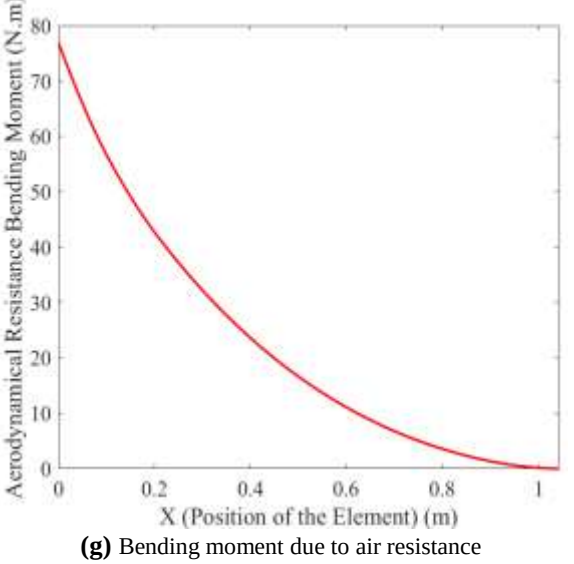

(g) Bending moment due to air resistance

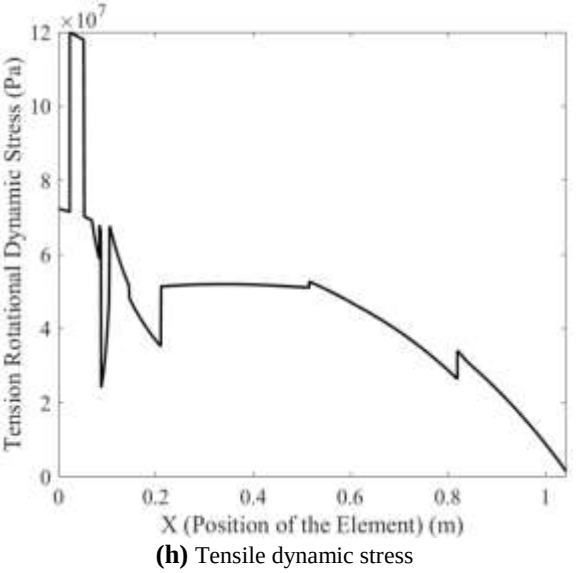

(h) Tensile dynamic stress

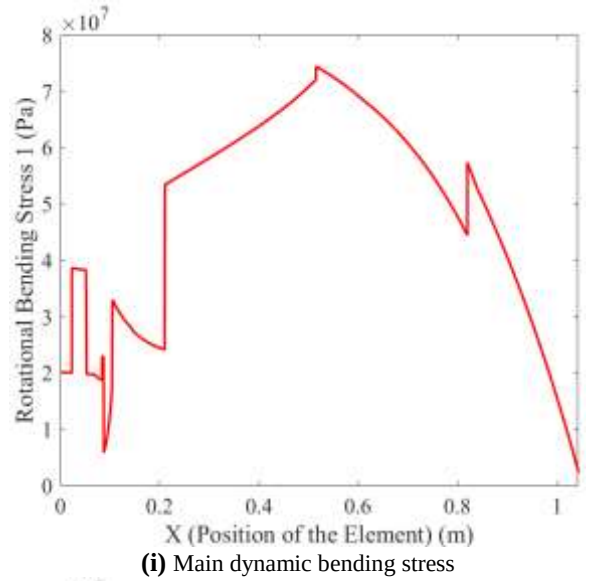

(i) Main dynamic bending stress

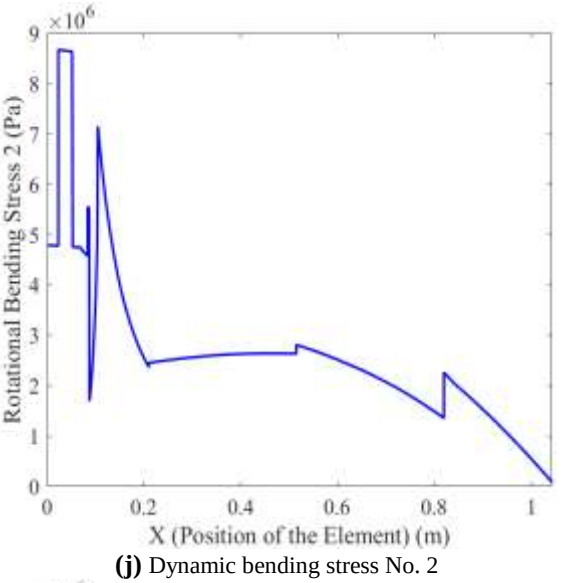

(j) Dynamic bending stress No. 2

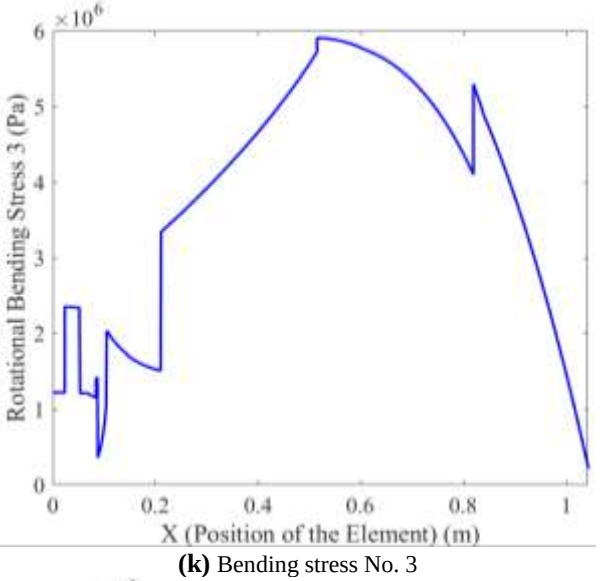

(k) Bending stress No. 3

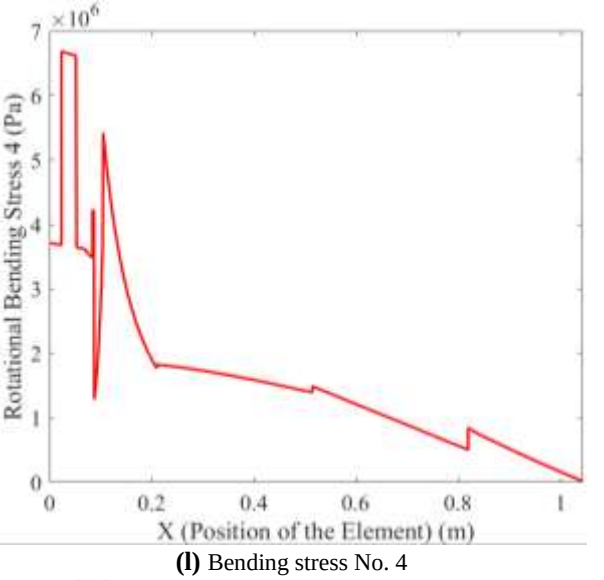

(l) Bending stress No. 4

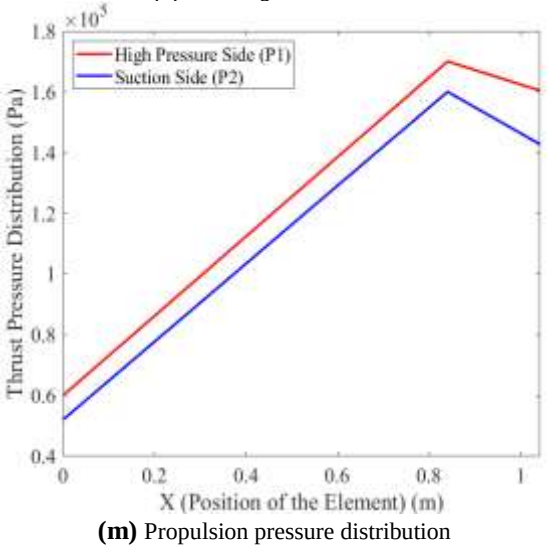

(m) Propulsion pressure distribution

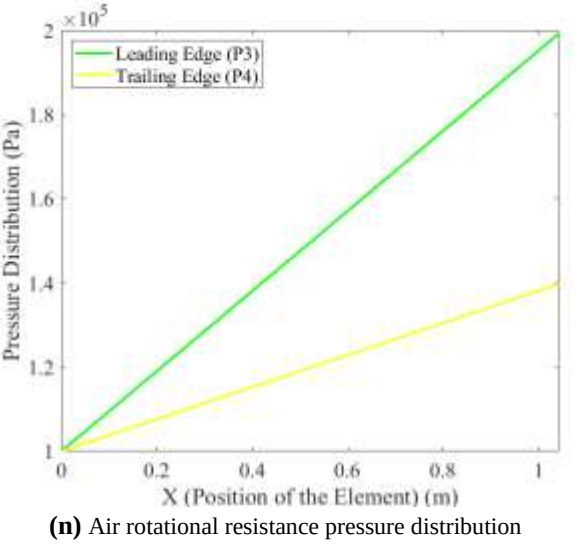

(n) Air rotational resistance pressure distribution

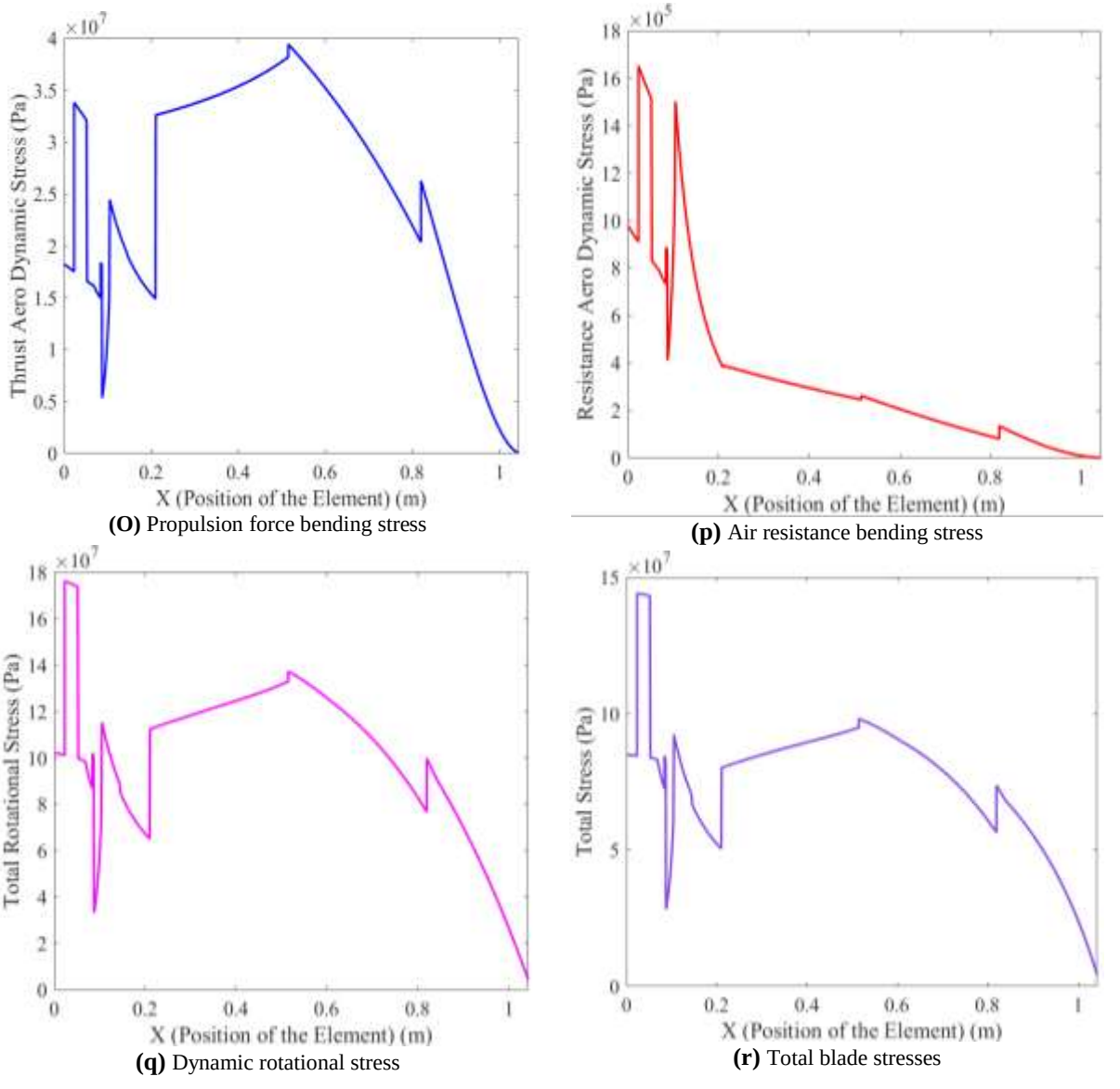

(O) Propulsion force bending stress

(p) Air resistance bending stress

(q) Dynamic rotational stress

(r) Total blade stresses

Fig. 18 Analysis of the propeller structure by quasi-analytical method and distribution of different parameters along the blade length**.**

7 Explain the results of the developed algorithm

According to "Fig. 18 (a)", the maximum centrifugal force is maximum at the root of the blade. All of mass element dynamic force affects these points. Therefore, the maximum tensile force is at the root of the blade. The rotational bending moment is maximum at the root of the blade ("Fig. 18 (b, c, d, and e)") and the aerodynamical bending moment is maximum at the root of the blade ("Fig. 18 (f, g)"). According to "Fig. 18 (h)", the maximum rotational dynamic stress is the root of the blade. There is a considerable jump at the "Fig. 18 (h)". This shows that the cross-section area is significantly reduced at the root point of the blade. This subject increases the dynamic stress at this point. The maximum rotational bending stress and aerodynamic bending stress are at the center of the blade. At this point, the blade thickness is low. In bending stress, in addition to the applied

bending moment, the equivalent moment of inertia is also important. In the center of the blade, the equivalent moment of inertia is much less than the root of the propeller (“Fig. 18 (i, j, k, o, p)”). The cumulative stress is presented in “Fig. 18 (q and r)”. The results of the quasi-analytical method confirm the FEM method.

8 Investigating the causes of overall stress reduction by aerodynamic loads

Figure 19 shows that the bending moment caused by the centrifugal force due to eccentricity and the bending moment caused by propulsion are opposite to each other. Since the rotational dynamic stresses are much more dominant, the stresses caused by the propulsion force reduce the total stresses of the system.

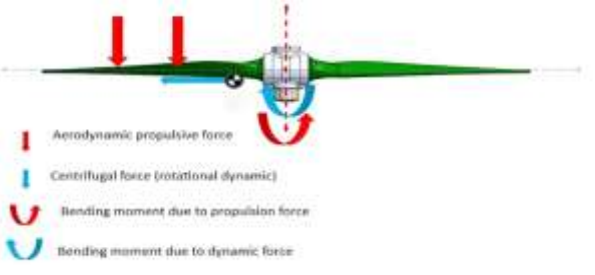

Fig. 19 **Different forces and moments entering the propeller system.**

9 Conclusions

In the present study, a quasi-analytical method algorithm in the geometry redesign and structural analysis of an airplane propeller was developed and compared with the finite element method. According to the results, the maximum structural stress of a propeller under rotational dynamic and aerodynamic loads is at the root of the propeller. In the case that only dynamic rotational loading is considered, the maximum stress of the propeller under dynamic loads is at the propeller root, and when only aerodynamic loading is considered, the maximum stress is at the middle of the propeller. Generally, aerodynamic stresses reduce the overall stress in the propeller because the bending moment caused by the centrifugal force due to eccentricity and the bending moment caused by the propulsion are opposite to each other. The values of rotational dynamic stress are much higher than aerodynamic stress. According to the mentioned cases, in order to increase the reliability of structural analysis, aerodynamic stresses are omitted and only rotational dynamic stresses are considered for structural analysis. Since the geometry of the propeller is constant in different working conditions and only the rotational speed changes, structural analysis can be used in the design in such a way that the maximum stress of the propeller has a direct relationship with the square power of the working rotational speed of the propeller. In this regard, if the propeller rotational speed changes to 80% of the initial speed, the structural stress will decrease to 64%. Of course, the important point is that at the maximum rotational speed, the propulsion force is maximum and at lower rotational speeds, the amount of propulsion force will also decrease. Reducing the propulsion force will reduce the aerodynamic stresses. There is a significant bending moment in the middle of the blade. The middle of blade has a weak moment of inertia relating to the root of the blade. This subject results in bending stress (aerodynamic and rotational dynamic) being maximum in the middle of the blade.

Appendix: Presentation of The Structural Analysis Algorithms Using a Quasi-analytical Method

In order to define blade geometry to structural analysis algorithm, the total geometry redesigned by the quasi-blade redesigning algorithm is presented in “Fig. 20”.

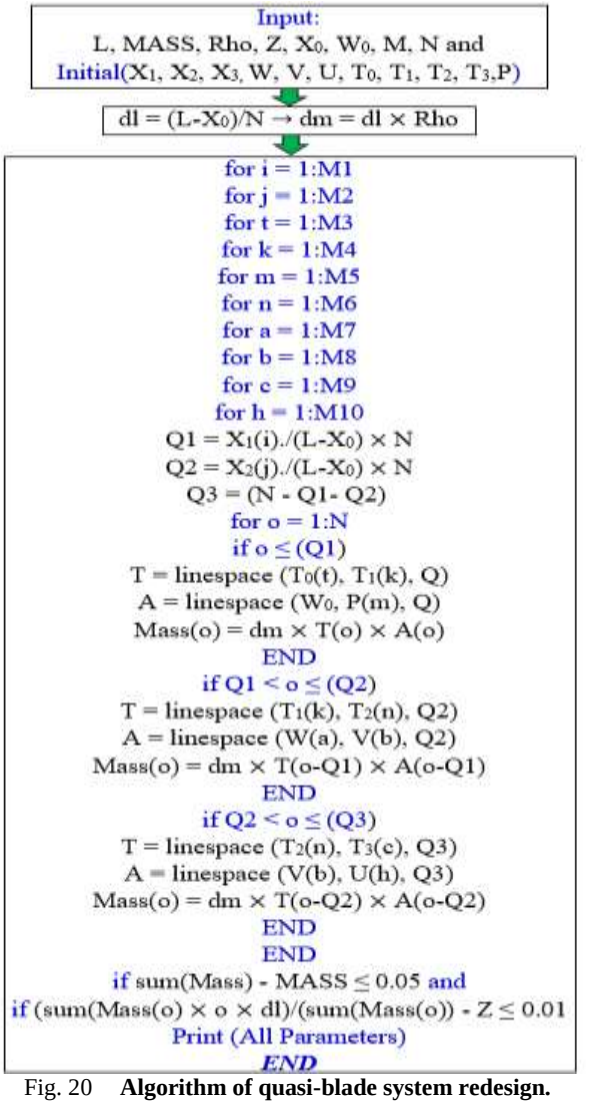

Fig. 20 **Algorithm of quasi-blade system redesign.**

The main dimension in "Fig. 13" is changed by the algorithmic try and error process. In this regard, the dimensions such as X, W, and T has own intervals. The size of each dimension is M, which M is matrix → M = [M1:M10]. The X2 and X3 are dependent on the X and L. The thickness matrix (T) and Area of cross-section (A), the Q1 and Q2 are calculated. T and A matrix construct the Mass matrix. The algorithm continues till the total mass was acceptable.

In order to calculate the cross-section area, mass, and moment of inertia distribution, mass and area-inertia algorithm is developed and presented in "Fig. 21". The root of blade with length of X0 affects the total mass. The Line1 = [X0, X1, X2, X3] and Line2 = [T0, T1, T2, T3]. The root of the blade has a circular cross-section and the other part of the blade has a rectangular (airfoil) cross-section. Therefore, the algorithm consists of two parts, before and after M.

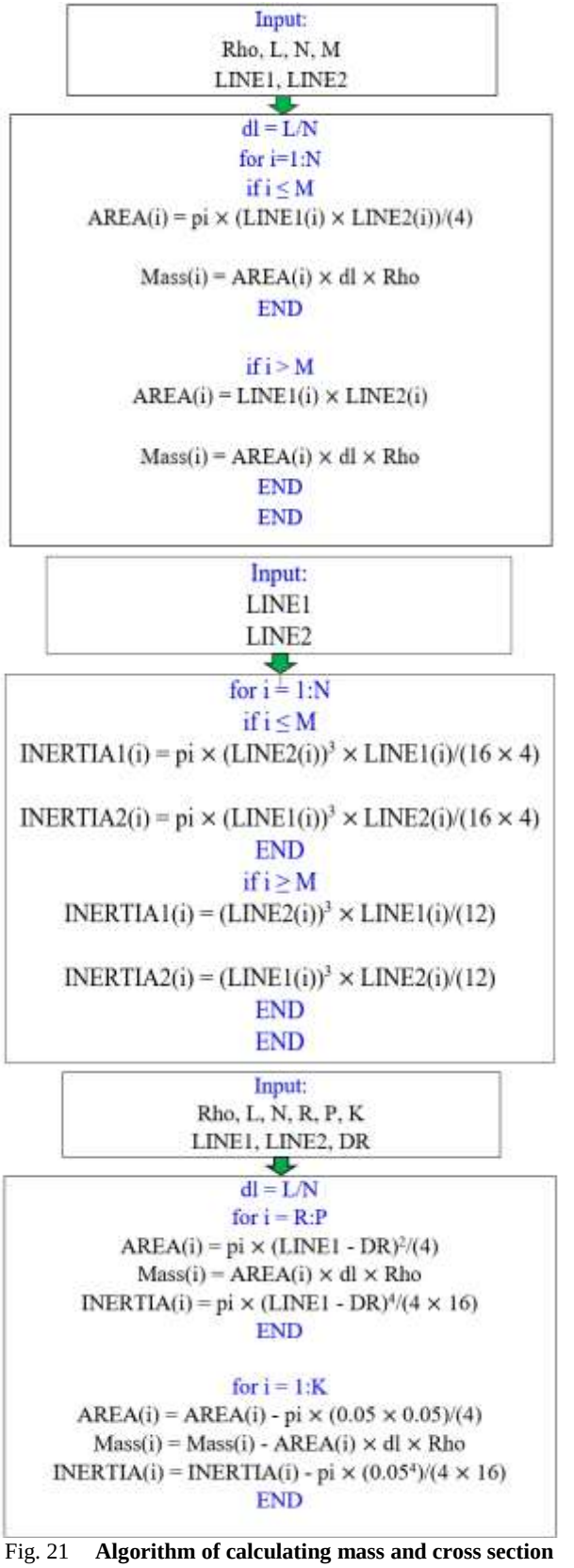

Fig. 21 **Algorithm of calculating mass and cross section area and moment inertia.**

The algorithm of calculating the dynamic force and tensile dynamic stress distribution is presented in "Fig. 22".

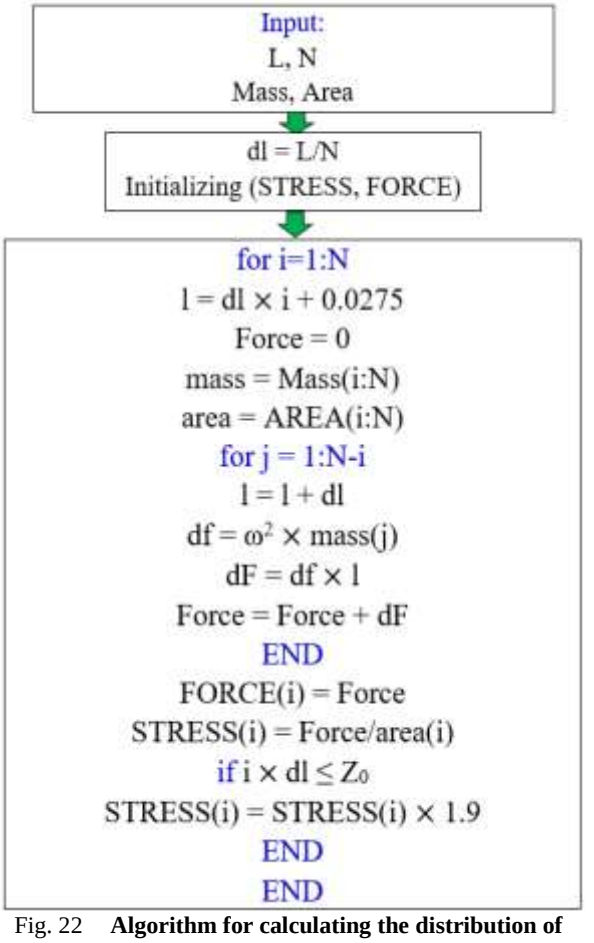

Fig. 22 **Algorithm for calculating the distribution of dynamic force and tensile dynamic stress along the blade length.**

There is one loop for all sections in the blade and there is an internal loop for each section. In each section, all of the element which affects stress must be considered. This subject was used in "Fig. 14" and Equation (1). This algorithm converts the continuous integral to discrete SUM. The distance of each element and center of rotation is calculated by the sum of previous elements lengths and also 0.0275. This subject was showed in "Fig. 15". According to stress concentration at the root of the blade, the algorithm has this section at the end of calculation.

The centrifiugal force also results in the bending moment and bending stress in the each section of the blade. Figure 23 presents the calculation of the bending stress of the blade. This algorithm is based on the previous algorithm ("Fig. 22"). In this algorithm, the dynamic force of each element results in the bending and is a function of dynamic force (df1) and arm of the moment (Eccen). Considering the twisting of the blade, the final moment multiplies the sin(Twist). The excentricity of blade sections is shown in "Fig. 16". According to the stress concentration at the root of the blade, the algorithm has this section at the end of the calculation.

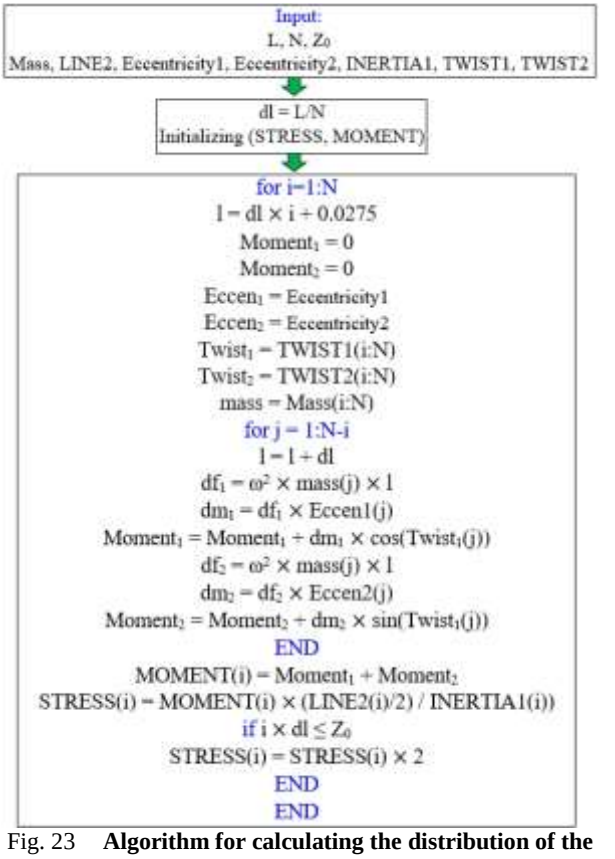

Fig. 23 **Algorithm for calculating the distribution of the dynamic bending moment due to eccentricity in a certain direction from the propeller and the dynamic bending stress along the blade length.**

Figure 24 presents the calculation of aerodynamics stress. This algorithm is similar to the previous algorithm. The difference between these algorithms is the bending moment. The bending moment of aerodynamics load is based on differential pressure. The differential pressure on each element leads to

aerodynamic force. This dynamic force on each element results bending moment along the blade. The Twisting and stress concentration also are considered in this part. The P3 is related to leading-edge pressure, and P4 is related to the trailing edge. The P1 and P2 are differential pressures relating to high and suction pressure zones.

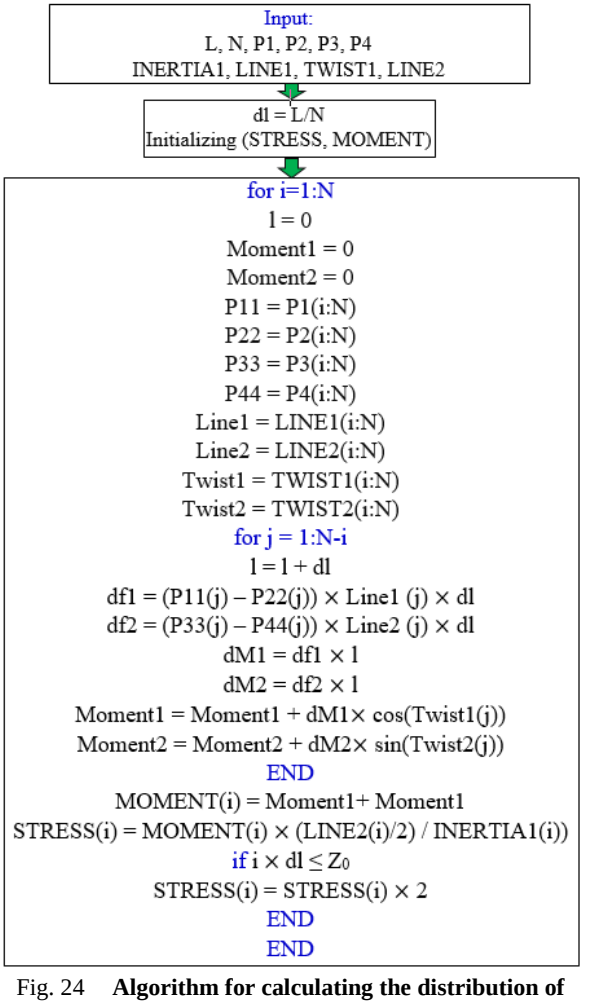

Fig. 24 **Algorithm for calculating the distribution of bending moment due to aerodynamic pressure to produce propulsive force and rotational resistance of air and the resulting bending stresses.**

Referenc es

[1] Yeh, M. K., Wang, C. H., Stress Analysis of Composite Wind Turbine Blade by Finite Element Method, IOP Conference Series: Materials Science and Engineering, Vol. 241, 2017, pp. 12-15.

[2] Srivastava, S., Roy, A. K., and Kumar, K., Design of a Mixed Flow Pump Impeller Blade and Its Validation Using Stress Analysis, Procedia Materials Science, Vol. 6, 2014, pp. 417-424.

[3] Wu, W. H., Young, W. B., Structural Analysis and Design of The Composite Wind Turbine Blade, Applied Composite Materials, Vol. 19, 2012, pp. 247-257.

[4] Duan, W., Zhao, F., Loading Analysis and Strength Calculation of Wind Turbine Blade Based on Blade Element Momentum Theory and Finite Element Method, Asia-Pacific Power and Energy Engineering Conference, IEEE, 2010, pp. 1-4.

[5] Yeh, M. K., Cheng, Y. C., and Wang, C. H., Finite Element Stress Analysis of Wind Blade Structure Under Wind Pressure, Taiwan Wind Energy Conference, Taipei, Taiwan, No. SI_07, 2015 (in Chinese).

[6] Heo, H., Ju, J., and Kim, D. M., Compliant Cellular Structures: Application to A Passive Morphing Airfoil, Composite Structures, Vol. 106, 2013, pp. 560-569.

[7] Di, T., Zhiliang, L., and Tongqing, G., Aeroelastic Analysis of Large Horizontal Wind Turbine Blades, Applied Mathematics and Mechanics (English Edition), Vol. 37(S1), 2016, pp. S97-S104.

[8] Metallic Material Properties Development and Standardization (MMPDS) Handbook, Battelle Memorial Institute, 2019.

[9] Behzad, M., Izanlo, H., Arghand, H., Davoodabadi, A., and Saleh, A., Bearing Housing Looseness Effect on Rotating Machinery Vibration, 29th International Congress on Sound and Vibration, 2023.

Int. J. Advanced Design and Manufacturing Technology, 2024, Vol. 17, No. 1, pp. 23-28

DOI: 10.30486/admt.2023.1968434.1380 ISSN: 2252-0406 https:// sanad.iau.ir/journal/admt

Investigating the Effect of Nanosilica on Compressive Strength of Hard Concrete by Considering Atomic Force Microscopy (AFM) Examinations

Seyed Mohammad Mahdi Shafiei
Department of Mechanical Engineering, West Tehran Branch, Islamic Azad University, Tehran, Iran
E-mail: shafiei.mohammad@wtiau.ac.ir

Mahboobeh Pirizadeh
Department of Civil Engineering, West Tehran Branch, Islamic Azad University, Tehran, Iran
E-mail: pirizadeh.mahboobeh@wtiau.ac.ir

Ebrahim Zolgharnein *
Department of Civil Engineering, North Tehran Branch, Islamic Azad University, Tehran, Iran
E-mail: ezolgharnein@yahoo.com
*Corresponding author

Received: 27 September 2022, Revised: 26 December 2022, Accepted: 10 January 2023

Abstract: This study investigated the compressive strength of hardened concrete and the formation of Calcium Silicate Hydrate (C-S-H) with the addition of nanosilica (SiO2). Compressive strength testing was performed using ASTM C496 to determine stress-strain curves and compressive strength of the materials. The hydration process and formation of C-S-H and Calcium Hydroxide (CH) were examined using Atomic Force Microscopy (AFM) and Fourier Transform Infrared Spectroscopy (FTIR). Results indicate an increase in compressive strength using 1, 3, and 5% of nanosilica to concrete replacement by volume in comparison to the control mix (without nanosilica). The optimum concrete replacement to yield maximum strength was of the 5% nanosilica content. Comparing the 56-day results for the 3 and 5% of nanosilica replacement samples shows the same percentage of C-S-H formation of 83 and 85%, respectively.

Keywords: AFM, Compressive Strength, Concrete, FTIR, NanoSilica

Biographical notes: Seyed Mohammad Mahdi Shafiei is an Assistant Professor at the Islamic Azad University, West Tehran Branch. He received his PhD from Iran University of Science and Technology in 2015. His current research interest is surface engineering. **Mahboobeh Pirizadeh** is an Assistant Professor of civil engineering at the Islamic Azad University, West Tehran Branch. She received her PhD from Tarbiat Modarres University, Tehran, Iran, in 2013. **Ebrahim Zolgharnein** is an Assistant Professor at Islamic Azad University, North Tehran Branch. He received his PhD from the Azerbaijan National Academy of Sciences.

1 INTRODUCTION

A series of chemical reactions takes place during the hydration process of concrete paste. Once water is added

to the cement, the tricalcium aluminate reacts with the gypsum to produce ettringite and heat. Next, the tricalcium silicate is hydrated to produce the C-S-H, lime and heat. Once the gypsum is gone, the ettringite becomes unstable and begins to react with the remaining tricalcium aluminate to form monosulfate aluminate hydrate crystals [1].

During a sulfate deficient solution, the monosulfate crystals become unstable. The crystals then resort back into ettringite during the presence of sulfates. The increase in the crystal size is what causes the cement to crack when subjected to sulfate attack. The belite hydrates to form C-S-H and heat. The C-S-H during this phase generates strength within the concrete. This process has a very slow rate; however, this compound produces the long-term strength of cement concrete. The ferrite goes through two progressive reactions with the gypsum. The first reaction is when the ettringite reacts with the water and gypsum to form ettringite, lime, and alumina hydroxides.

The second reaction occurs when the ferrite further reacts with the ettringite that was formed during the first reaction in order to produce garnets. Hydration kinetics has been modeled by several researchers to better understand the reactions and changes that Portland cement undergoes during the hydration process. Lin and Meyer [2] developed a hydration kinetic model for Portland cement based on the thermodynamics of multiphase porous media. Their model considered the effects of cement fineness, chemical composition, water-cement ratio, pressure, and curing temperature, to analyze the ultimate degree of hydration and develop a corresponding formula. They concluded that their proposed model adequately demonstrates the different experimental results for cement hydration at high pressures and elevated temperatures. Trapote-Barreira [3] conducted a research dissertation on the dissolution kinetics of calcium silicate hydrate gel and the durability of mortar. Examinations were carried out using AFM and Force Microprobe Analyzer (EPMA). Zaki and Ragab [4] conducted testing using 0, 0.5, 0.7, and 1% of nanosilica in concrete along with 20% of silica fume in all mixes. They concluded the optimum amount of nanosilica was 0.5% by weight of cementitious material. Gopinath et al. [5] investigated the effects of nanosilica in normal-strength concrete using 1.5 and 3% of nanosilica to cement replacement by weight; compared to concrete without nanosilica. Their findings portrayed varying results with greater earlier 3-day strength results with 3% of nanosilica and higher 28-day results with 1.5% of nanosilica. Salkhordeh et al. [6] investigated the effects of recycled concrete as an aggregate and nanosilica as cement replacement in Self-Consolidating Concrete (SCC) for 28-day compressive strength. With different percentages of recycled concrete aggregates ranging from 0 to 100 in 20% intervals and nanosilica replacing 10% of cement weight; they found that adding nanosilica to all samples leads to an increase in compressive strength. Elkady et al. [7] investigated the reasons for the inconsistencies in the workability and compressive strength of nanosilica concrete. The research investigated how agglomeration can affect the compressive strength and workability of normal strength concrete due to different methods of deagglomeration. Results showed that sonication proved to be the most significant de-agglomeration method as it enhanced the gain in compressive strength of concrete by 23% using only 1% nanosilica to cement substitution. Givi et al. [8] studied the size effects of SiO2 nanoparticles on compressive, flexural, and tensile strength of binary blended concrete. They specified that the rate of the pozzolanic reaction is related to the surface area existing during the reaction. Thus, it is feasible to add high purity (99.9%) nanosilica with a high Blaine fineness value (60 m2 /g) in order to improve the characteristics of cement. Their results showed that nanoparticles blended with concrete increased the compressive, flexural, and tensile strength at all curing ages. Belkowita and Armentrout [9] also studied the relationships of using different sizes of nanosilica in cement paste. They measured the heat of hydration, the concentration of CH through X-ray diffraction, grain structures through AFM, and compressive strength. Their experimental results showed an increase in compressive strength as the C-S-H became more rigid when the nanosilica particles decreased in size and their size distribution broadened. Bi et al. [10] tested nanosilica in concrete for compressive strength and durability. The nanosilica used was a powder obtained from an extraction process of silica sand. Their results indicated that the combined use of nanosilica with silica fume effectively increases the compressive strength and durability of the concrete. Quercia et al. [11] studied two different types of nanosilica in Self-Compacting Concrete (SCC). Both types of nanosilica, fumed powder silica, and precipitated silica in colloidal suspension have similar particle size distributions; yet, both were produced in different processes. Their results demonstrated that the use of nanosilica in SCC can improve the mechanical properties and durability of concrete. Spectroscopic methods have commonly been used to study the chemistry behind the hydration process of Portland cement. However, the study of cement hydration with the incorporation of nanosilica is an uncommon area of study. The main objective of this study is to investigate the effect of nanosilica in cement on the hydration process of concrete over 56 days. Fourier Transform Infrared Spectroscopy (FTIR) was used to study the complexity of the hydration chemistry of the Portland cement with the addition of nanosilica content. This study investigated the hydration process of Portland cement with increments of nanosilica addition by

cement replacement, monitored by FTIR and AFM. The results of FTIR spectroscopic signatures were compared to the represented samples examined under AFM. An attempt to correlate the spectroscopic features to the development of concrete strength is also determined. Strength testing was carried out by using Forney Universal Testing and MTS machines for compressive strength and stress-strain. This investigation also studied the effects of water curing in comparison to vacuum curing. Concrete cured in airless environments or vacuum curing, is a new area of interest.

2 EXPERIMENTAL METHOD

2.1. Methodology

This experimental study investigated the strength and hydration of Portland cement with nanosilica compared to cement paste without nanoparticles. Compressive testing was carried out using Forney and MTS testing machines. FTIR and AFM were used to monitor and portray the chemical transformations of the cement paste. Approximately 25 specimens were prepared to conduct several tests using 4 in. by 8 in. cylinders and 2 in. cubes. Four (4) mix designs were created. The first mix, M1, was the control mix of the cement paste. The next three mixes, M2, M3, and M4, consisted of 1, 3, and 5% nanosilica by volume of cement, respectively. Nearly half of the specimens created from each mix were cured in water and the other half in the vacuum seal.

$$Fcm = fc + 1.34s + 1.5 \text{ M Pa} \quad (1)$$

$$Fcm = fc + 2.33s - 4 \text{ M Pa} \quad (2)$$

Where, f is pressure strength [2].

2.2. Materials

The materials used in this study were Portland cement Type 1, nanosilica and Polycarboxilate polymer-based superplasticizer. The nanosilica is silicon oxide nanoparticles (SiO_2) synthetic product of porous and nearly spherical particles. The particle size ranges from 15-20 nm, consisting mainly of pure silica (>99%). Figure 1 shows the physical properties of the nanosilica used herein. The nanosilica was obtained from Sky Spring Nanomaterials, Inc., Houston, Texas, while the polycarboxylate was provided by Handy Chemicals Limited, located in Beachwood, Ohio. The Polycarboxylate, also referred to as Megapol is a high performance acrylic based polymer. It's specifically was developed to improve the workability, strength, flexibility, modulus of elasticity, and durability of concrete properties. It is an effective dispersant and High Range Water Reducer (HRWR). The water to cement (w/c) ratio was 0.27 using a superplasticizer. The cement and nanosilica were measured and dry mixed together by hand to reduce the loss of nanoparticles. The polycarboxylate and water were both measured and mixed together. Next, following ASTM Standard C-305, the water with superplasticizer was poured into a rotary mixer bowl (Hobart HL 200, 20-quart mixer). The dry mix of cement and nanosilica was then added to the mixer bowl. Once the materials were in the bowl, they were mixed at a low rate (59 agitator rpm) for 30 sec. After mixing at low speed, the mixing rate was increased to Level 1 (107 agitator rpm) for one minute. After the mixing process concluded, the mixture was carefully poured into cylinder and cube molds. The cylinders and cubes were then ridden, vibrated, and leveled before being stored away for curing. One cylinder from each batch mixture was weighed and measured to obtain the unit weight after mixing. For this experiment, a total of 12 cubes and 13 cylinders, totaling 25 samples, were manufactured for testing. Half of the manufactured specimens were cured in water while the other half were cured in vacuum curing. The cylinders were comprised of plastic molds, 4 inches in diameter and 8 inches in depth, in compliance with ASTM C-470. The cube molds were comprised of brass, exactly 2 inches in size, and able to form three cubic specimens within each mold. Physical properties of the nanosilica are Particle Size (nm): 15-20, Surface Area (m^2 /g): 640, Bulk Density (g/cm^3): 0.08-0.10, Molecular SiO_2, Molecular Weight: 60.08, Porosity (ml/g): 0.6, Morphology: Porous and nearly spherical. Several testing machines were used throughout this experimental study to obtain the required data. The compressive strength data was obtained. The AFM and FTIR were used to analyze the chemistry and microstructure of the testing specimens. The MTS 810 Landmark Servo hydraulic Testing system was used to determine compressive strength and stress-strain curves obtained from testing. These systems include MTS software; Flex Test controls, MTS servo hydraulic technology, and a complete selection of accessories. The testing machine was used to carry out all cylinder testing, including compression and modulus of elasticity. The machine has a 400-kip load capacity and a load rate of 12,000 lbs/min. The high-definition Atomic Force Microscope (AFM EVO LS) made by ZEISS, was used for microstructure characterization and analysis of the hardened concrete specimens. EVO LS has full environmental capabilities to capture nanoscale interactions of samples under various pressures, temperatures, and humidity. The Fourier Transform Infrared Spectroscopy- FTIR (Thermo Scientific Nicolet iS10 FT-IR Spectrometer) was used to monitor the changes in C-S-H as the hydration of cement paste takes place. This FTIR Spectrometer delivers the highest confidence in the verification and identification of materials. With the use of OMNIC Spectra software, the

Nicolet iS10 can manage results and provide accurate and valid answers.

3 RESULTS

3.1. Compressive Strength and Stress-Strain

The Zwick/Roell Z250 Testing Machine was used to conduct all cylinder compressive strength tests. The results from testing are displayed by column graphs in "Figs. 1 and 2". Figure 1 shows the average compressive strengths for all water cured testing cylinders. This figure represents the control, 1 and 3% of nanosilica to cement. As shown, both the 1 and 3% nanosilica samples performed significantly higher than that of the controlled. To compare the cylinder compressive strengths of the reference curing methods, a separate column graph was created to represent the comparison.

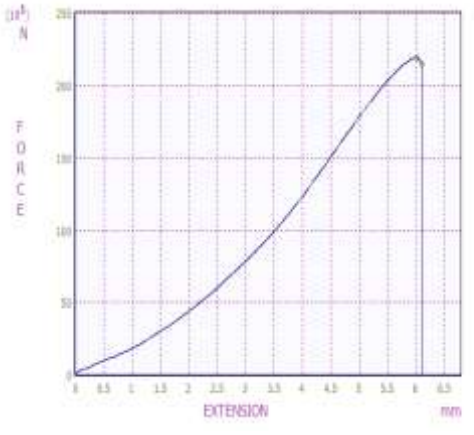

Fig. 1 The average cylinder strength of the 0% controlled samples.

The stress-strain curves display partial results, while the graphs displaying the methods with the change in nanosilica content were developed but not shown here due to page limitations of the manuscript. Figure 2 displays the stress-strain curves for the control samples. As seen the stresses were around 405 Mpa for the reference samples and over 480 Mpa for the control samples. This Figure also shows the stress-strain relationship of the samples for all testing. However, with the incorporation of nanosilica, the stresses at all testing are shown to be much greater than that of the control samples. The stresses for the 5% nanosilica samples range between 480 Mpa.

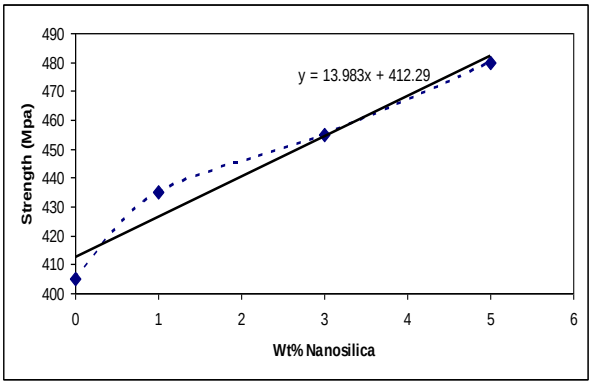

Fig. 2 Compressive strength for different curing methods.

3.2. Atomic Force Microscope (AFM)

The AFM was used to obtain microscopic images of the tested specimens during all testing. From the images obtained, a further analysis using MATLAB was conducted to filter the images using a Gaussian filter and to determine the percentages of chemical products for which that image portrays. The MATLAB program was used to filter the AFM images and generate histograms outlying the major constituents of the hydrated cement. Backscatter used in AFM allows grey-level identification of the chemical elements. This grey-level identification will distinguish the different phases of the hydrated cement products. Four main phases can be identified, which are: Porosity (P), Calcium Hydroxide (CH), Calcium Silicate Hydrate (C-S-H), and Unhydrated Products (UP). Other products such as limestone and other hydrated products were not distinguished. Using the MATLAB analysis, it was expected to produce histograms with three or more peaks for all testing samples. The various peaks help distinguish the thresholds that separate the phases from the grey-level images. Once the grey-level images were filtered, a colored image was generated portraying each phase with a specific color. For this study, the following phases were assigned with the specified color: P-Blue, C-S-H-Green, CH-Red, and UP-Black. Changes to the thresholds were expected to be seen in the adjusted histogram after running the MATLAB script once again. Figure 3 shows the original AFM image of the hardened cement paste sample containing 1% nanosilica after water curing and testing. Figure 3, shows the same sample after filtered using the Gaussian filter. Features from this image are lighter and more distinguished.

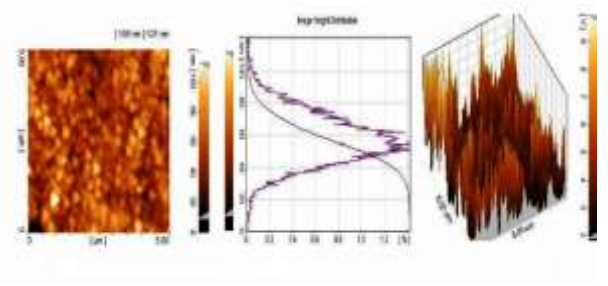

Fig. 3 AFM image-colored phases.

From the results gathered from the MATLAB analysis of all samples, a figure was generated to portray the results obtained. Figure 2 shows the water cured averages of porosity, calcium silicate hydrate and calcium hydroxide for all testing days under changes in nanosilica content. Results from "Fig. 2" show an increase in C-S-H formation from 3-day to 56-day results for the control and all nanosilica mixtures. Results show a maximum amount of C-S-H formation in the 5% nanosilica samples than that of the 1 and 3% nanosilica samples. Also, at all testing ages, samples with nanosilica outperformed or contained more C-S-H content than the control. The 14-day test results performed poorly due to an experimental error, resulting in obscure data results that do not follow the trend of the results obtained. For this reason, several of the 14-day results collected were removed from the analysis and figures thereof. For data that has been removed from the following figures, the cell block will display "OUT". Similar results were obtained for vacuum curing.

3.3. Fourier Transform Infrared Spectroscopy (FTIR)

In this study, FTIR spectrum was used for each sample under water and vacuum curing and for each percentage of nanosilica. The process starts with displaying the reference spectrum for the anhydrate dry cement. It was observed two major peaks occur around the wavelength numbers of 877 and 1100 cm^{-1}. From the chemical composition of Portland cement and from past literature for possible assignment for peaks observed on the cement spectrum; the peaks can possibly be assigned to the CaO and the SiO_2 for the two peaks respectively. There was a large peak in the area of 3400 cm^{-1}, which can be associated with hydrogen bond (O-H) or capillary water within that region. This comparison shows that the optimum nanosilica to cement replacement for curing is 1%. Results also indicate about a 5% difference in the control mix compressive strength. When comparing the control samples to that of the samples containing nanosilica, a significant increase in C-S-H formation during all testing days with all additions of nanosilica was noticed. With the increase in C-S-H formation, results signify an increase in strength with the hardened cement samples containing nanosilica than the control samples without nanosilica. Also, AFM results show a greater increase in C-S-H formation in the samples containing 5% nanosilica to cement replacement in comparison to the 1 and 3% nanosilica samples. The percentage of C-S-H found in the 5% nanosilica samples was slightly higher than the 3% nanosilica samples through both methods of curing. These results should indicate a greater increase in compressive strength with the 5% nanosilica samples; however, the compressive strength results show the 5% nanosilica samples portraying lower strength values when compared to the 1 and 3% nanosilica tests. The reasoning behind the dissimilarities could be due to the area in which the AFM image data was gathered and collected to determine the amount of C-S-H or hydrated products. The AFM images only look into one location under 1300 x magnification within a specific sample. Thus, the area examined under the AFM is a small representation of the sample and therefore provides an estimate of the full sample strength. When comparing the water and vacuum curing methods of the AFM results, the percentage of C-S-H within the samples is very similar for each testing day. For instance, when looking into the 56-day results, the control water and vacuum samples show approximately 70 percent C-S-H formation. Similarly, when comparing the 56-day results for the 3 and 5% of nanosilica replacement samples shows the same percentage of C-S-H formation of 83 and 85%, respectively. From these results, the curing methods performed identically in the curing of the samples and formation of C-S-H.

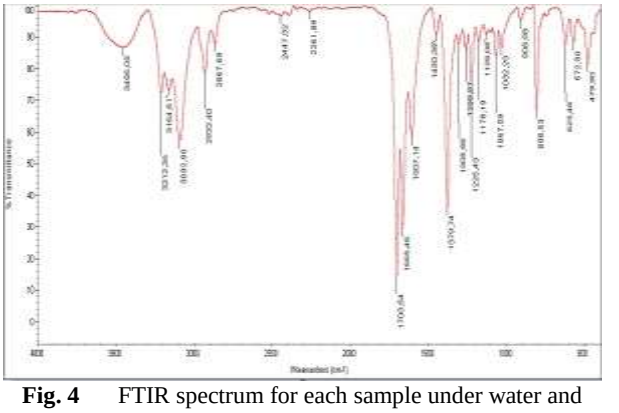

Fig. 4 FTIR spectrum for each sample under water and vacuum curing and each percentage of nanosilica.

4 CONCLUSIONS

In this study, the hydration process of Portland cement with additives of nanosilica has been monitored. With the use of AFM and FTIR, signatures of C-S-H which produce most of the concretes' strength, have been determined and examined with age. Also, using Forney

and MTS testing equipment, the overall strength of the hardened cement pastes was determined and recorded for analysis. The objective of this report was to demonstrate how FTIR and AFM can give more insight into the hydration of cement, with and without the incorporation of nanosilica, during the later ages or stages of hydration. From this study and the results obtained, several conclusions have been drawn:

• The area of possible formation of C-S-H was determined to show an increase with respect to time; signifying the increase in strength with age
• In comparing water and vacuum curing methods, the vacuum cured samples perform identically to that the water cured when monitoring the hydration. Results indicate similar increases with age between both methods
• Nanosilica in all percentages of cement replacements showed a significant increase in compressive strength in all ages of testing. When comparing the amount of nanosilica replacement, results show the optimal percentage of cement replacement is 1%, followed closely by 3% nanosilica addition. 5% nanosilica replacement results portrayed a decrease in strength in comparison to the 1 and 3% additions.
• Water curing proved to be a beneficial form of curing by displaying higher overall strength values than that of the vacuum cured method. Yet, the compressive strength of vacuum cured specimens showed a small reduction in compressive strength (usually within 5%), when compared to the water cured samples

REFERENCES

[1] Belkowitz, J., Armentrout, D., The Investigation of Nano Silica in The Cement Hydration Process, ACI Special Publication, 2019.

[2] Bi, J., Pane, I., Hariandja, B., and Imran, I., The Use of Nanosilica for Improving of Concrete Compressive Strength and Durability, Applied Mechan. Mater., Vol. 204, 2012, pp. 4059-4062, DOI: 10.4028/www.scientific.net/AMM.204-208.4059.

[3] Elkady, H., Serag, M., and Elfeky, M., Effect of Nano Silica De-Agglomeration and Methods of Adding Super Plasticizer on The Compressive Strength and Workability of Nano Silica Concrete, Civil Environ, Res., Vol. 3, 2013, pp. 21-34.

[4] Givi, A. N., Rashid, S. A., Aziz, F. N. A., and Salleh, M. A. M., Experimental Investigation of The Size Effects of SiO2 Nano-Particles on The Mechanical Properties of Binary Blended Concrete, Composites Part B: Eng., Vol. 41, 2010, pp. 673-677, DOI:10.1016/j.compositesb.2020.08.003.

[5] Gopinath, S., Mouli, P. C., Murthy, A., Iyer, N., and Maheswaran, S., Effect of Nano Silica on Mechanical Properties and Durability of Normal Strength Concrete, Archives Civil Eng., Vol. 58, 2012, pp. 433-444, DOI: 10.2478/v.10169-012-0023.

[6] Lin, F., Meyer, C., Hydration Kinetics Modeling of Portland Cement Considering the Effects of Curing Temperature and Applied Pressure, Cement Concrete Res., Vol. 39, 2019, pp. 255-265, DOI: 10.1016/j.cemconres.2009.01.014.

[7] Quercia, G., Spiesz, P., Husken, G., and Brouwers, J., Effects of Amorphous Nano-Silica Additions on Mechanical and Durability Performance of SCC Mixtures, Proceedings of the International Congress on Durability of Concrete, (CDC' 12), 2012.

[8] Salkhordeh, S., Golbazi, P., and Amini, H., The Improvement of 28-Day Compressive Strength of SCC Made by Different Percentages of Recycled Concrete Aggregates Using Nano-Silica, Trapote Barreira, A., 2015.

[9] Dissolution Kinetics of CSH Gel and Durability of Mortar, Materials, 19: 01-01. Winter, N. B., Understanding Cement: The Fast Star User-friendly Insight into Cement Production, Cement Hydration and Cement and Concrete Chemistry, 1st Edn., WHD Microanalysis Consultants Ltd., ISBN-10: 0957104529, 2012, pp. 206.

[10] Zaki, S. I., Ragab, K. S., How Nanotechnology Can Change Concrete Industry, Proceedings of the International Conference Sustainable Built Environment Infrastructures in Developing, (EID' 09), 2019, pp. 407-414.

[11] Wang, L. E. I., Jin, M., Guo, F., Wang, Y. A. N., and Tang, S., Pore Structural and Fractal Analysis of The Influence of Fly Ash and Silica Fume on The Mechanical Property and Abrasion Resistance of Concrete, Fractals, 2020, pp. 29.

Numerical and Experimental Investigation of Natural Frequency and Damping Coefficient of Flexible Cellular Lattice Structures

Amir Hosein Samimi, Mohammad Reza Karamooz-Ravari*, Reza Dehghani
Faculty of Mechanical and Materials Engineering
Graduate University of Advanced Technology, Iran
E-mail: amirhshs73@gmail.com, m.karamooz@kgut.ac.ir, r.dehghani@kgut.ac.ir
*Corresponding author

Received: 11 June 2023, Revised: 26 August 2023, Accepted: 10 October 2023

Abstract: Cellular lattice structures encompass a class of metamaterials characterized by the arrangement of interconnected struts and/or plates, offering an adaptable microstructure that enables a broad range of property control. These structures have garnered significant attention for their distinctive properties and have found widespread application across industries such as aerospace, medical, pharmaceutical, automotive, defense, and safety. This study seeks to explore the impact of geometric parameters on the natural frequency and damping coefficient of cellular lattice structures. Samples featuring BCC and OCTET architectures with varying porosities were initially produced using fused deposition modeling (FDM). Subsequently, both experimental and numerical analyses were conducted to assess the first natural frequency and damping coefficient of these materials. Comparison of the numerically obtained results with experimental data revealed a strong agreement. The findings indicate that, for both BCC and OCTET lattices, an increase in porosity is associated with a decrease in both natural frequency and damping coefficient.

Keywords: Finite Element, Lattice Structures, Natural Frequency, Vibration

Biographical notes: ***Amir Hosein Samimi*** *received his MSc in Mechanical Engineering from Graduate University of Technology, Kerman, Iran, in 2021.* ***Mohammad Reza Karamooz-Ravari*** *and* ***Reza Dehghani*** *received their PhD in Mechanical Engineering from Isfahan University of Technology (IUT), Isfahan, Iran, in 2015 and 2010, respectively. They are currently associate professors at the Graduate University of Advanced Technology, Kerman, Iran, in the field of additive manufacturing and vibrations, respectively.*

1 Introduction

Cellular materials refer to a group of materials that consist of a network of struts and/or plates in three-dimensional space. These materials provide special properties such as high energy absorption, high strength-to-weight ratio, low heat transfer (thermal insulation), low relative density, high sound absorption capability, and low weight [1-2]. Cellular materials can be classified into two groups, including lattice structures and porous materials. In contrast to porous materials, cellular lattice structures have regular

structures so that their mechanical properties are highly controllable. Due to their unique properties, these materials have found many applications in various industries, including pharmaceuticals, military, and aerospace [3]. Vibration of mechanical systems is one of the most important causes of failure that might have irreversible effects. In examining the vibrational response of a system, natural frequency is of great importance. The natural frequency of a system depends mainly on its modulus of elasticity, density, and geometry. Accordingly, in order to change the natural frequency of a desired part, its geometry and/or material might be changed. However, in most cases, it is not possible to change the geometry of the part due to the limitations and application constraints. On the other hand, since the modulus of elasticity-to-density ratio of many metals is almost identical, changing the bulk material would not lead to favorable results. Given the above, the use of cellular materials, whose modulus of elasticity and density can be changed and adjusted, is a good option for controlling the vibration response of mechanical systems [4-6].

When human body is exposed to the vibrations of a machine, it can suffer from serious damages to the joints and brain. Accordingly, reducing the amplitude of vibrations, imposed on the occupants of a vehicle, can be very important [7]. Lattice structures are good choices to reduce transmitted vibrations so that it is important to study their vibrational behavior, i.e., natural frequency, mode shapes, and damping coefficient, which might be obtained using the modal analysis. Modal analysis is a method for determining dynamic properties of a structure subjected to dynamic loads. It can be utilized as a tool for determining natural frequency, damping response, and mode shapes, known as modal parameters, as a mathematical function called Frequency Response Function (FRF) [8-10].

Several experimental, numerical, and theoretical studies have been performed in order to obtain the aforementioned modal parameters. Using the definition of joint stiffening element, Dong and Zhao [11] investigated the effect of these joints on the stiffness of the lattice structures made by additive manufacturing and found that the stiffness of the model considering these connections is closer to the experimental results compared to those without these considerations. Kim et al. [12] investigated the effect of debonding embedded between the face-layer laminates and the honeycomb core on the stiffness and natural frequency of sandwich honeycomb beams. Their studies showed that by increasing debonding, the natural frequency decreases. Lou et al. [13] studied the free vibration of sandwich beams under several typical boundary conditions. They also examined the effects of material properties and geometric parameters on natural frequencies. Monkova et al. [14] investigated the effect of cell size and volume ratio on the damping and compression properties of BCC lattice structure made of ABS polymer. The obtained results show that the stiffness and frequency increase with increasing cell thickness.

To enhance the mechanical vibration isolation properties of a machine frame, Syam et al. [6] presented the design, analysis and experimental verification of strut-based lattice structures. They found that a trade-off needs to be made between the frame's natural frequency and its compressive strength in order to achieve high efficiency of vibration isolation. Niu et al. [15] proposed a two scale optimization method in order to find the optimal configuration of cellular lattice structures with maximum structural fundamental frequency. Lopatin et al. [16] theoretically studied the vibrational behavior and frequency response of composite lattice cylindrical shells under clamped-free boundary conditions. Using homogenization approach, Lou et al. [17] modeled a sandwich structure with a pyramidal truss core made of stainless steel under simply-supported

boundary condition and investigated the effect of length, radius and inclination angle of the struts on the frequency response of the structure.

By combining the Euler–Bernoulli and Timoshenko beam theories, Xu et al. [18] studied the effects of geometrical and material parameters on the natural frequency of composite sandwich beams with lattice truss core. The effect of the strength of the cellular lattices produced by additive manufacturing technology on their vibration responses was performed by Azmi et al. [19]. They found that the stiffer the lattice is, the higher the frequency would be. Using a combined design and optimization method, Anderson et al. [20] studied the effect of structural irregularities on the fundamental frequency in order to maximize the first eigenfrequency. Utilizing Timoshenko beam elements, Samimi et al. [7] investigated the effects of dimensional inaccuracies, which is an intrinsic characteristic of additive manufacturing of cellular lattice structures, on their natural frequency.

Braun et al. [21] used numerical simulations to assess the effect of the damage percentage, cell type, cell size, and material on the frequency and modal responses of the sandwich plates. Scalzo et al. [4] investigated the influence of the experimental setup of modal analysis on the modal parameters of different SLM AISI 316L lattice structures. In another work [5], they used experimental and numerical investigations in order to assess the dynamic behavior of lattice structures in the medium-high frequency range. Yi et al. [22] used the finite element approach to calculate the axial vibration characteristics of pyramid lattice cylindrical structure and assessed the effects of different parameters on its damping capability.

Tempelman et al. [23] studied the broadband vibration absorption characteristics of three different latices, i.e., simple-cubic, diamond and octet-truss, using experimental and theoretical methods. Wei et al. [24] carried out finite element numerical simulation and modal testing of the dynamic damping performance of steel-based Kelvin lattice structures fabricated by indirect additive manufacturing. They found that the natural frequency and damping ratio might be regulated by changing the lattice porosity. Zhang et al. [25] investigated the frequency response and damping ratio of IWP-type triply periodic minimal surfaces (TPMS) lattice structures by dynamic vibration transfer rate tests. They concluded that the stiffness and inherent frequency of the lattice structure are directly and inversely proportional to the volume fraction and the cell size, respectively. Liu et al. [26] proposed a multiscale topology optimization framework for maximizing the natural frequency of multi-morphology lattice structures (MMLSs). Multi-morphology lattice unit cells with smooth characteristics were achieved using the Kriging-assisted morphological post-process and sigmoid function-based hybrid transition strategy. Since the flexible TPU polymers have high intrinsic damping capability, TPU cellular lattice structures would be good candidates for vibration isolations. In this paper, two different cellular lattice structures, i.e., BCC and OCTET, with different values of porosity are additively manufactured using TPU flexible polymers. Then, the first natural frequency as well as damping coefficient is obtained by experimental measurements. In addition, a solid finite element model is developed in order to predict the above-mentioned modal parameters. The obtained results show a good agreement between experimental and numerical findings. Moreover, it is concluded that the natural frequency as well as damping coefficient decreases as the porosity of the structures increases.

2 Materials and Methods

This section begins with a brief overview of the lattices under consideration, followed by an explanation of how the samples were fabricated. It then introduces the approach used for setting up and conducting the experiments, as well as the finite element modeling and three-dimensional representation of the samples. The section concludes with a comprehensive explanation of the methods used to estimate the damping coefficient of the samples, incorporating both numerical and experimental data.
In this paper, two different cellular lattice structures, i.e., BCC and OCTET, are chosen for experimental and numerical analysis. Figure 1 (a) and (b) respectively demonstrate the schematic representation of the unit cells corresponding to BCC and OCTET lattice structures.

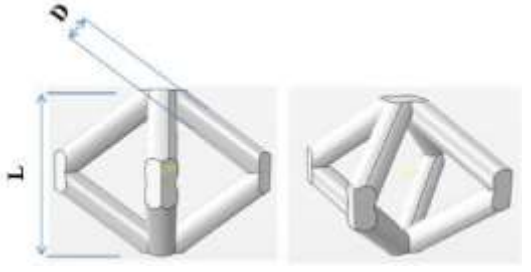

(a)

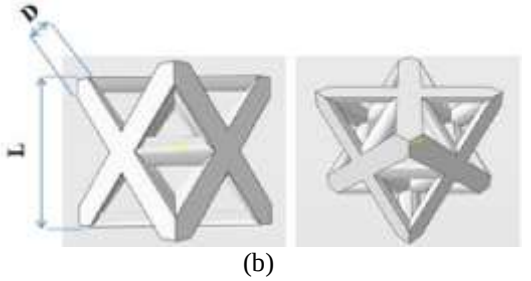

(b)

Fig. 1 **Schematic representation of the unit cell corresponding to the lattice structure: (a): BCC, and (b): OCTET. Here D is the struts' diameter and L is the unit cell size.**

As can be seen, the BCC unit cell contains 8 diagonal struts connecting 6 vertices while the OCTET unit cell is comprised of 14 vertices connected by 36 struts. Considering *s* as the number of struts, and *v* the number of vertices, the Maxwell number, *M*, might be introduced as [27-28]:

$$M = s - 3v + 6 \tag{1}$$

If $M < 0$, the lattice is considered as bending-dominated structure, while for $M \geq 0$, the axial deformation mechanism is the main one so that the lattice is called stretch-dominated. Using Equation (1), the Maxwell number of BCC and OCTET lattices is equal to -4 and 0, respectively. Accordingly, BCC lattice structure is bending-dominated while OCTET is stretch-dominated.

2.1. Sample Fabrication

In this paper, Fused Deposition Modeling (FDM) is used for fabrication purposes. To do so, a three-dimensional model generated through ABAQUS finite element package, is exported as STL format and used as the input of the FDM machine. Quantum 2025 3D printer, manufactured by Persia 3D Printer Company, is utilized to produce the lattices. Using this machine, a part with the dimensions of 20, 20, and 25 cm respectively in directions of x, y, and z-axes, can be fabricated. The utilized process parameters are presented in "Table 5".

Table 5 **Process parameters used for fabrication purposes**

Parameter	Value	Unit
Initial Layer thickness	0.25	*mm*
Layer height	0.2	*mm*
Shell thickness	0.8	*mm*
Bottom/Top thickness	0.6	*mm*
Fill Density	100	*%*
Print speed	25	*mm/s*
Retraction speed	27	*mm/s*
Travel speed (Nozzle speed)	27	*mm/s*
Printing temperature	200	$^{\circ}C$
Bed temperature	40	$^{\circ}C$

All the samples are fabricated from TPU flexible polymer filaments, produced by YS Company. The filament has the diameter of 1.75 mm, and its operating temperature is in the range of 200 to 245 degrees Celsius. The physical properties of the material that are required for the simulation of frequency response are elastic modulus of 4 *GPa*,

density of 1200 Kg/m^3, and Poisson's ratio of 0.47.

Due to the limitations of the utilized machine, the unit cell size, *L*, is supposed to be 17 *mm* and the struts' diameter are chosen in a way that the desired porosity can be obtained. The porosity values of BCC lattices are considered to be 65 and 85 percent, which are related to the strut's diameter of 5 and 3.1 *mm*, and the values of 65 and 75 percent are chosen for OCTET lattice structures, corresponding to the strut's diameter of 3.25 and 2.65 *mm*. Notice that for OCTET lattice structure with a porosity of 85%, the struts' diameter would be about 2 *mm* which cannot be produced with a good quality by the utilized printing machine. Thus, 75% porosity is considered instead of 85%.

2.2. Experimental Measurements

In order to calculate FRF, first, a vibratory excitement is generated in the structure by applying a certain force to a specific point and the vibration response, which is the output-to-input ratio, is measured at another point. To do so, three major steps, including preparing test setup, measuring frequency response by applying excitation force, and data processing must be followed. The excitation force is applied to the structure at a suitable range by various devices such as modal hammer [4], [9], which is equipped with several hammerheads, accelerometer sensor and a handle. Hammerheads are made of different materials such as plastic and steel, each of which is attached to the hammer according to the bulk material of the component being tested. The accelerometer sensor is the most important part of the hammer machine that measures the acceleration of the component being tested and displays it at the outlet. The accelerometer should be firmly attached to the desired part; however, this is not possible in practice which can affect the accuracy of the measurements; so that, the firmer the connection base, the more accurate the result would be. The accuracy of this sensor depends on various factors such as rigidity of the boundaries, air temperature, and humidity [9]. As shown in "Fig 2", the fabricated samples are supposed to be clamped at one end and free at the other. In order to create this type of boundary conditions, Zipper glue is used to attach the samples to a chipboard, and the clipboard to the wall. Since the sensor can be attached to the desired location of the parts using magnets, it is necessary to attach a piece of steel at that site. As shown in "Fig 2", a circle-shaped piece of steel, with the diameter of at least 2.54 cm, which is equal to the loadcell diameter, is glued to the center of the samples for attaching the sensor.

The fundamental frequency and damping coefficient are obtained experimentally using modal analysis. To perform modal analysis and data processing, Vib V4 Pro vibrometer equipped with piezoelectric accelerometer sensor and modal hammer fabricated by Delta Sanat Sharif Company is used. This device could be applied for several types of condition monitoring, including dynamic balance of surfaces, measurement of vibrations and natural frequency, and speed analysis. It is important to note that the cable connected to the hammer should be connected to channel 1 of Vib V4 Pro and loadcell cable should be connected to channel 2. After connecting these two devices, the other end of the loadcell should be connected to the circle-shaped steel attached to the desired structure. Due to the short time interval between the start time of the test and hitting time, the modal hammer is kept close to the component, so that a low impact was done immediately after the test started. In this way, the amplitude was displayed graphically in terms of frequency. Accordingly, damping was obtained using half-power bandwidth method, which will be briefly introduced in the next sections.

2.3. Finite Element Modeling

ABAQUS finite element package is utilized for three-dimensional modeling as well as

numerical simulations. To do so, a Python script is developed in order to generate the three-dimensional model of the unit cell of the lattices. The program receives the coordinates of the vertices of the structures, the connection matrix, struts' diameter (D), and unit cell size (L) to produce the unit cell of the lattices. The unit cell is then repeated along different perpendicular directions to construct the whole structure of concern.

(a)

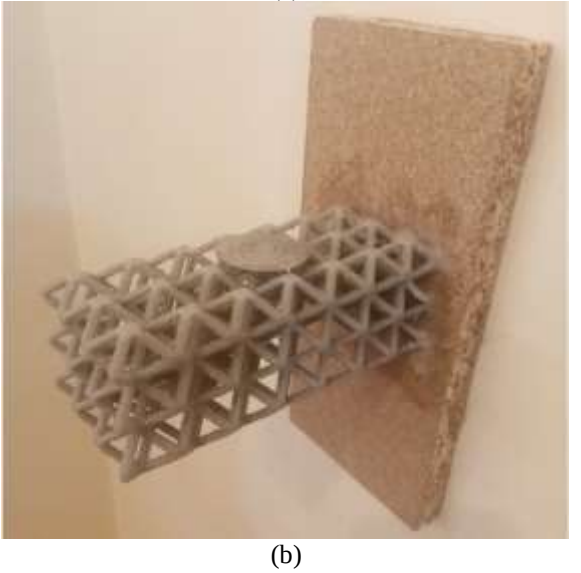

(b)

Fig. 2 **Preparing the clamped-free boundary conditions for: (a): OCTET65%, and (b): BCC85%.**

The lattices are meshed using 10-node quadratic tetrahedron elements denoted by C3D10 in ABAQUS. A mesh sensitivity analysis is then performed, by reducing the mesh size by a factor of 0.5, until the difference between the natural frequencies of two successive simulations is smaller than 10 percent.

In order to compare the results, the boundary conditions of all the samples are considered to be identical. In this paper, in accordance with the experimental tests, one side of the specimen is completely constrained, so that:

$$U_1 = U_2 = U_3 = 0 \tag{2}$$

Where U_1, U_2, and U_3 are the translational degrees of freedom in the x, y, and z directions, respectively.

Given that natural frequency is the intended output, no applied load is considered. However, impact loading was applied in a short period in damping analysis stage in order to accurately simulate the experimental test of modal analysis. "Table 6", presents how the load was applied during the analysis period.

Table 6 The applied load history during the simulation of damping of the structure

Load Magnitude	Time (s)
0	0.0
0	0.05
1	0.10
0	0.15
0	0.2
0	1

2.4. Frequency and Damping Analysis

This section explains how to determine the intended output and calculate the fundamental frequency and damping, numerically and experimentally.

In order to perform the damping analysis, the subspace solution method is utilized along with the modal dynamic approach to obtain the displacement response of the desired point of the lattice, as shown in "Fig 3".

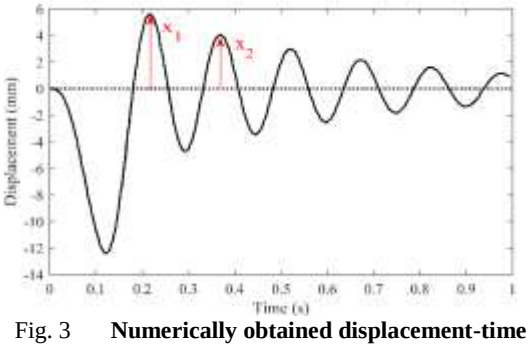

Fig. 3 **Numerically obtained displacement-time response.**

In this context, the analysis time is defined as 1 second divided into 1000 segments. The greater the number of these segments are, the more accurate the analysis response would be. However, the computation time is drastically depended on the number of these segments.

Damping ratio, ξ, can be calculated considering the two successive peaks of the graph shown in "Fig. 3" and using Equation (3) [10]:

$$\xi = \sqrt{\frac{\delta^2}{\delta^2 + 1}} \tag{3}$$

Where:

$$\delta = \frac{1}{2\pi} \ln\left(\frac{x_i}{x_{i+1}}\right) \tag{4}$$

In which x_i is the displacement at the i-th peak. The data obtained from the experimental test performed by the vibrometer are analyzed in MRS3000 software which can magnify the graphs. The frequency amplitude graph in the software is logarithmic in db. Therefore, the graph was taken out of logarithmic state in order to use half-power bandwidth method. As shown in "Fig. 4", the half-power bandwidth method assumes that the frequency response is approximately symmetric, with respect to vertical axes at natural frequency in the amplitude-frequency graph.

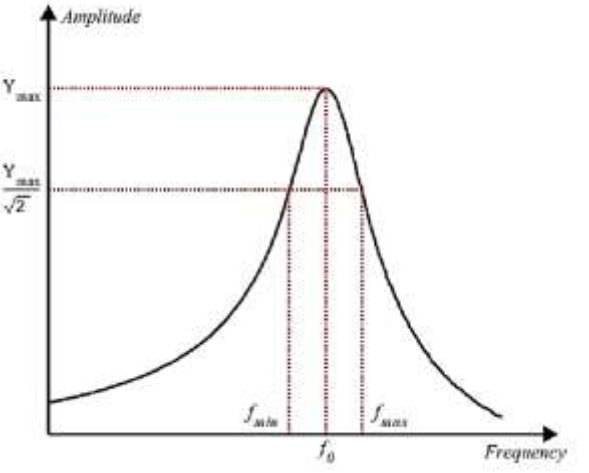

Fig. 4 **Schematic representation of half power bandwidth method.**

The graph peak indicates the desired frequency and the value corresponding to this point is displayed on the vertical axis as Y_{max}. Then, this value is divided by $\sqrt{2}$ and the obtained value is marked on the vertical axis. Afterwards, a hypothetical line parallel to the horizontal axis is drawn to determine the points colliding with the frequency response graph and the frequencies f_{min} and f_{max} are obtained. The damping ratio can then be determined using the following Equation [20]:

$$\xi = \frac{f_{\max} - f_{\min}}{2 f_0} \tag{5}$$

3 Results and Discussion

In this section, we begin by presenting the results obtained from frequency analysis, both from numerical simulations and experimental measurements, followed by a discussion on the comparison between these results. Subsequently, we present the findings from the damping analysis, and provide a comparison between the results obtained from numerical simulations and experimental observations.

The experimental and numerical analysis are performed on samples comprised of 3*3*7 cells in 3 orthogonal directions. Each experimental measurement is repeated twice

and the average outputs are used for calculations. In the case of finite element modeling, after mesh sensitivity analysis, a mesh size of 8 mm and 12 mm is obtained for the BCC and OCTET cellular lattice structure, respectively. By applying this mesh sizes to the structures, the BCC structure with 65% and 85% porosity, and OCTET structure with 65% and 75% porosity contains respectively 202046, 211735, 234921, and 164939 elements.

3.1. Simulation Results for Fundamental Frequency

"Table 3" presents the simulation results of the first three modes in ABAQUS software for BCC structure with 65% and 85% porosities and OCTET structure with 65% and 75% porosities.

Table 7 **Results of frequency analysis for the first 3 modes**

Structure Type	Porosity (%)	Mode number	Diameter (mm)	Natural frequency (HZ)
BCC	65	1	5	12.27
BCC	65	2	5	12.53
BCC	65	3	5	45.90
BCC	85	1	3.1	6.6
BCC	85	2	3.1	6.9
BCC	85	3	3.1	24.55
OCTET	65	1	3.25	16.594
OCTET	65	2	3.25	16.597
OCTET	65	3	3.25	45.21
OCTET	75	1	2.65	14.75
OCTET	75	2	2.65	14.76
OCTET	75	3	2.65	41.85

According to the results obtained for the first mode of the structures, it can be concluded that the natural frequency decreased by increasing the structure porosity, the reason for which could be attributed to the reduced stiffness due to the decreased strut diameter. In addition, at the same value of porosity, the fundamental frequency of the OCTET lattices is almost 35% higher than that of BCC structure.

3.2. Experimental Results for Fundamental Frequency

Figures 5 and 6 indicate the amplitude at an acceptable bandwidth as a function of frequency for BCC and OCTET cellular lattice structures, respectively. Two tests were taken from each structure, and the average values are reported. Using these two figures, the fundamental natural frequency is obtained and presented in "Table 4". It can be observed that the numerically obtained results are in good agreement with the experimentally measured ones. The maximum error is about 15.71 percent which is associated with OCTET cellular lattice structure with 75 percent porosity.

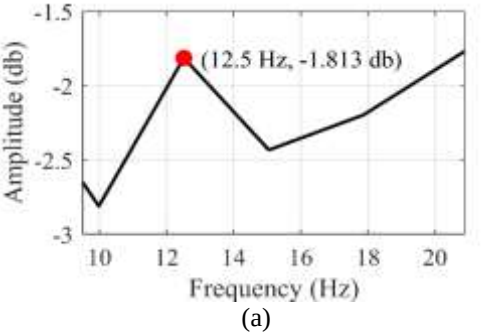

(a)

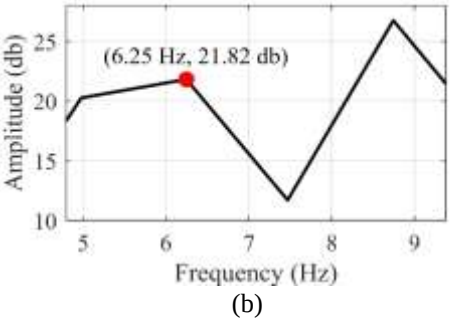

(b)

Fig. 5 **The amplitude at an acceptable bandwidth as a function of frequency for BCC cellular lattice structure with: (a): 65% porosity, and (b): 85% porosity.**

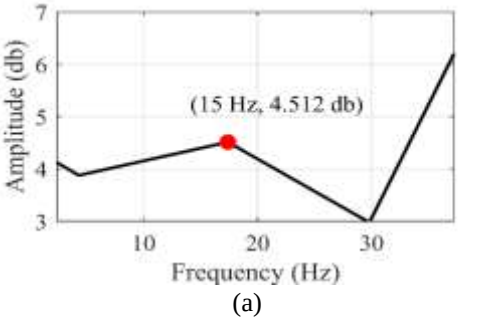

(a)

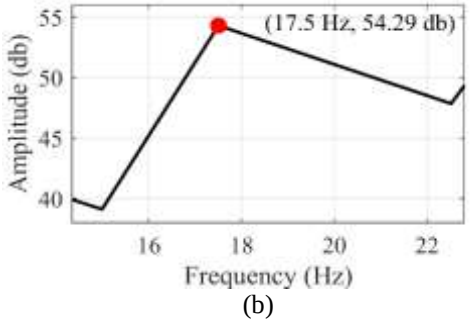

(b)

Fig. 6 **The amplitude at an acceptable bandwidth as a function of frequency for OCTET cellular lattice structure with: (a): 65% porosity, and (b): 75% porosity.**

Table 8 **Comparison of the experimentally (exp) and numerically (FEM) obtained fundamental natural frequency as well as damping coefficient. Here, err stands for the error between the numerical and its corresponding experimental value**

Lattice	Porosity (%)	Fundamental frequency (Hz)		Damping coefficient	
		exp	FEM [err %]	exp	FEM [err %]
BCC	65	12.5	12.27 [1.84]	0.1838	0.1958 [6.5]
BCC	85	6.25	6.6 [5.6]	0.45	0.1052 [76]
OCTET	65	15.0	16.59 [9.58]	0.319	0.266 [16.6]
OCTET	75	17.5	14.75 [15.71]	0.2272	0.2112 [7.0]

3.3. Damping Analysis Results

Referring to the results presented in Section 3.2, the damping ratio is calculated and the results for the four structures are given in "Table 4". Given that calibration should be performed in order to obtain numerical damping, an explanation of calibration and how it should be done is provided. Then, results of experimental and numerical tests are presented and compared.

In numerical investigations, either Rayleigh or structural damping might be used to evaluate damping coefficient of the lattices. However, since there is no available source about structural damping as well as damping degree of the utilized bulk material, Rayleigh damping method was employed in which [10]:

$$\xi = \frac{\alpha}{2\omega} + \frac{\beta\omega}{2} \quad (6)$$

In order to calibrate α and β parameters, different logical values are assigned to the parameters and damping coefficient is calculated through amplitude-displacement graph as mentioned earlier. When the calculated value became equal to the experimentally obtained damping coefficient for BCC structure with 65% porosity, values of α and β coefficients are considered as the parameters associated with the bulk material. These values are then attributed to the bulk material for all other simulations. Using this approach, $\alpha = 0.02$ and $\beta = 0.005$ are obtained.

Figures 7 to 10 show the displacement at the accelerometer sensor installation site as a function of time for BCC lattice structures with 65 and 85% porosity and OCTET structures with 65 and 75% porosity, respectively. These curves are used to calculate the damping coefficient of the lattices.

The numerically obtained damping coefficient along with the error from experimental findings is calculated and presented in "Table 4". Comparing these results shows that, except for the BCC structure with 85% porosity, the numerical and experimental results are well consistent.

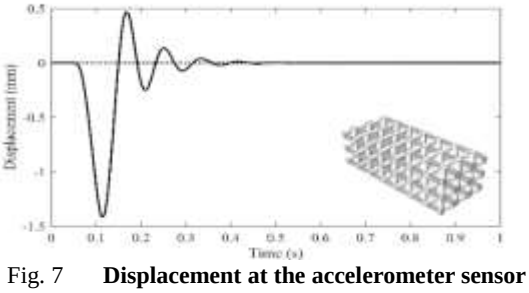

Fig. 7 **Displacement at the accelerometer sensor installation site as a function of time for BCC lattice with 65% porosity.**

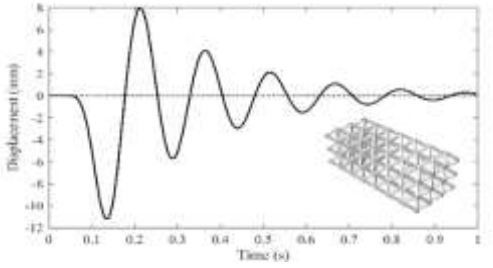

Fig. 8 **Displacement at the accelerometer sensor installation site as a function of time for BCC lattice with 85% porosity.**

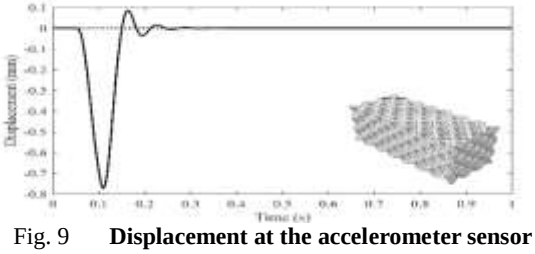

Fig. 9 **Displacement at the accelerometer sensor installation site as a function of time for OCTET lattice with 65% porosity.**

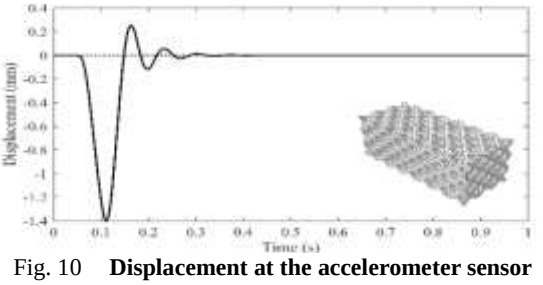

Fig. 10 **Displacement at the accelerometer sensor installation site as a function of time for OCTET lattice with 75% porosity.**

The reason for the discrepancy of experimental and numerical damping for this structure can be low accuracy of the device for this range of natural frequency and low mass and stiffness of the structure, which causes a lot of vibration in the structure with the slightest impact. In addition, it can be concluded that the damping ratio decreases as the porosity increases. Moreover, the value of damping coefficient of OCTET lattices is 36% higher than the damping coefficient of BCC lattices with the same value of porosity.

4 CONCLUSIONS

This paper presents a comprehensive examination of the natural frequency and damping coefficient of two cellular lattice structures, namely BCC and OCTET, through both numerical simulations and experimental investigations. The results demonstrate a strong correspondence between the numerical and experimental data, with the largest frequency error occurring in the OCTET cellular lattice structure with 75% porosity, amounting to 15.7%. The study reveals that as the porosity of the structure increases, both the natural frequency and damping coefficient decrease, attributed to the reduced stiffness resulting from the decrease in strut diameter. Furthermore, the OCTET structure exhibits higher natural frequency and damping coefficient compared to the BCC structure.

References

[1] Ashby, M. F., et al., Metal Foams: A Design Guide, Elsevier, 2000.

[2] Banhart, J., Manufacturing Routes for Metallic Foams, Jom, Vol. 52, No. 12, 2000, pp. 22-27.

[3] Meisel, N. A., Williams, C. B., and Druschitz, A., Lightweight Metal Cellular Structures Via Indirect 3D Printing and Casting. in 2012 International Solid Freeform Fabrication Symposium, University of Texas at Austin, 2012.

[4] Scalzo, F., Totis, G., and Sortino, M., Influence of the Experimental Setup on the Damping Properties of SLM Lattice Structures. Experimental Mechanics, Vol. 63, No. 1, 2023, pp. 15-28.

[5] Scalzo, F., et al., Experimental Study on The High-Damping Properties of Metallic Lattice Structures Obtained from SLM, Precision Engineering, Vol. 71, 2021, pp. 63-77.

[6] Syam, W. P., et al., Design and Analysis of Strut-Based Lattice Structures for Vibration Isolation, Precision Engineering, Vol. 52, 2018, pp. 494-506.

[7] Samimi, A. H., Karamooz-Ravari, M. R., and Dehghani, R., Investigation of the Effects of Dimensional Inaccuracies on the First Natural Frequency of Cellular Lattice Structures, ADMT Journal, Vol. 15, No. 3, 2022, pp. 109-117.

[8] Døssing, O., Structural Testing: Modal Analysis and Simulation, Brüel & Kjær (Ed.), Vol. 2. 1988.

[9] Brown, D. L., Passing the Torch-Structural Dynamics/Modal Analysis

from Here to Sound and Vibration, Vol. 34, No. 1, 2000, pp. 6-7.

[10] Fu, Z. F., He, J., Modal Analysis, Elsevier, 2001.

[11] Dong, G., Zhao, Y. F., Numerical and Experimental Investigation of The Joint Stiffness in Lattice Structures Fabricated by Additive Manufacturing, International Journal of Mechanical Sciences, Vol. 148, 2018, pp. 475-485.

[12] Kim, H. Y., Hwang, W., Effect of Debonding on Natural Frequencies and Frequency Response Functions of Honeycomb Sandwich Beams, Composite Structures, Vol. 55, No. 1, 2002, pp. 51-62.

[13] Lou, J., et al., Free Vibration Analysis of Lattice Sandwich Beams Under Several Typical Boundary Conditions, Acta Mechanica Solida Sinica, Vol. 26, No. 5, 2013, pp. 458-467.

[14] Monkova, K., et al., Mechanical Vibration Damping and Compression Properties of a Lattice Structure, Materials, Vol. 14, No. 6, 2021, pp. 1502.

[15] Niu, B., Yan, J., and Cheng, G., Optimum Structure with Homogeneous Optimum Cellular Material for Maximum Fundamental Frequency, Structural and Multidisciplinary Optimization, Vol. 39, No. 2, 2009, pp. 115-132.

[16] Lopatin, A., Morozov, E., and Shatov, A., An Analytical Expression for Fundamental Frequency of The Composite Lattice Cylindrical Shell with Clamped Edges, Composite Structures, Vol. 141, 2016 pp. 232-239.

[17] Lou, J., Ma, L., and Wu, L. Z., Free Vibration Analysis of Simply Supported Sandwich Beams with Lattice Truss Core, Materials Science and Engineering: B, Vol. 177, No. 19, 2012, pp. 1712-1716.

[18] Xu, M., Qiu, Z., Free Vibration Analysis and Optimization of Composite Lattice Truss Core Sandwich Beams with Interval Parameters. Composite Structures, Vol. 106, 2013, pp. 85-95.

[19] Azmi, M. S., et al. Vibration Analysis of FDM Printed Lattice Structure Bar, In Proceedings of SAKURA Symposium on Mechanical Science and Engineering, 2017.

[20] Andresen, S., Bäger, A., and Hamm, C., Eigenfrequency Maximisation by Using Irregular Lattice Structures, Journal of Sound and Vibration, Vol. 465, 2020, pp. 115027.

[21] Braun, M., vanez, I., and Aranda-Ruiz, J., Numerical Analysis of the Dynamic Frequency Responses of Damaged Micro-Lattice Core Sandwich Plates, The Journal of Strain Analysis for Engineering Design, Vol. 55, No. 1-2, 2020, pp. 31-41.

[22] Yi, R., et al., Axial Elastic Wave Propagation Characteristics of Pyramid Lattice Cylindrical Structure, Chinese Journal of Theoretical and Applied Mechanics, Vol. 54, No. 10, 2022, pp. 2717.

[23] Tempelman, J. R., et al., Experimental Investigations into Broadband Vibration Absorption of Metastructures with Lattice Designs. in ASME 2019 International Design Engineering Technical Conferences and Computers and Information in Engineering Conference, 2019.

[24] Wei, Y., et al., Damping Behaviors of Steel-Based Kelvin Lattice Structures Fabricated by Indirect Additive Manufacture Combining Investment Casting, Smart Materials and Structures, Vol. 29, 2020, pp. 055001.

[25] Zhang, C., et al., Vibration Characteristics of Additive Manufactured IWP-type TPMS Lattice Structures, Composite Structures, Vol. 327, 2024, pp. 117642.

[26] Liu, X., Gao, L., and Xiao, M. Multiscale Topology Optimization Framework for Natural Frequency Maximization of Multi-Morphology Lattice Structures, Composite Structures, Vol. 328, 2024, pp. 117720.

[27] Maconachie, T., et al., SLM Lattice Structures: Properties, Performance, Applications and Challenges, Materials & Design, Vol. 183, 2019, pp. 108137.

[28] Phani, A. S. and Hussein, M. I., Dynamics of Lattice Materials, Wiley, 2017.

Int. J. Advanced Design and Manufacturing Technology, 2024, Vol. 17, No. 1, pp. 39-49

DOI: *ISSN: 2252-0406* *https:// sanad.iau.ir/journal/admt*

Nd:YAG Laser Processing of Thick NiTi Wires to Locally Alter Transformation Properties Towards Achieving Multiple Memory Shape Memory Alloys

Amin Alipour, Mahmoud Kadkhodaei*, Ehsan Foroozmehr

Department of Mechanical Engineering,
Isfahan University of Technology, Isfahan 8415683111, Iran
E-mail: alipoor68@gmail.com, kadkhodaei@iut.ac.ir, eforoozmehr@iut.ac.ir
*Corresponding author

Received: 11 November 2023, Revised: 12 January 2024, Accepted: 14 February 2024

Abstract: Every commercial NiTi (Nitinol) Shape Memory Alloy (SMA) has its own transformation temperatures, which may cause limitations in ever-growing demands for the application of these alloys in novel engineering designs. Among various methods proposed to achieve multiple functional characteristics, laser processing offers effective solutions in locally controlling the transformation properties of NiTi parts. The current work describes the application of laser technique followed by post-processing to locally alter transformation temperatures and impose phase transition for thick NiTi wires. To this end, various laser parameters are applied, and the influences of peak power and pulse width on the functional, microstructural, and mechanical properties of laser processed samples are studied. A four-sided laser processing protocol is proposed to process almost the whole cross section of thick Nitinol wires. It is also shown that post-processing heat treatment is required to recover the shape memory properties of as-processed Nitinol specimens. The transformation temperatures of the final processed Nitinol wire increase by about 50 °C compared to those of the unprocessed base material.

Keywords: Multiple Memory Shape Memory Alloy, Nd:YAG Laser, Post-Processing

Biographical notes: Amin Alipour received his PhD in Mechanical Engineering from Isfahan University of Technology, Isfahan, Iran, in 2022. **Mahmoud Kadkhodaei** is a Professor of Mechanical Engineering at the Isfahan University of Technology. He received his PhD in Mechanical Engineering from Isfahan University of Technology in 2007. His current research focuses on Smart Materials, Additive Manufacturing, Biomechanics, and Metal Forming. **Ehsan Foroozmehr** received his PhD in Mechanical Engineering from Southern Methodist University, Dallas, Texas, in 2009. He is currently an Associate Professor at the Department of Mechanical Engineering, Isfahan University of Technology. His current research interest includes Laser Material Processing, Additive Manufacturing and Fiber Optic Sensors.

Research paper

1 INTRODUCTION

The unique responses of Shape Memory Alloys (SMAs), including Shape Memory Effect (SME) and Pseudoelasticity (PE), make them an ideal option to be widely applied in various high tech. industries. SME is the ability to eliminate the residual strains after the loading cycle upon heating whereas, based on the PE effect, a large amount of strains can be spontaneously recovered through a mechanical loading/unloading cycle. Due to better strength, corrosion resistance, ductility, stability of transformation temperatures, and biocompatibility, NiTi is the most well-known and applicable shape memory alloy [1]. The extraordinary features of SME and PE depend on the composition and processing history of Nitinol alloys [1-2]. Since these characteristics are uniform through commercial NiTi elements, they pose only one set of transformation properties leading to the so-called single memory SMAs. However, new engineering demands urge promoting functionality and enhancing design adjustability of applied components. One way to address this issue is embedding more transformation properties by locally controlling the microstructure and/or composition of NiTi-based SMAs. Consequently, various approaches have been so far proposed to locally tune the properties of monolithic Nitinol alloys.

As one of the first attempts, Miura et al. [3] used different Direct Electric Resistance Heat Treatment (DERHT) for each section of an orthodontic wire. Hence, each section experienced a distinct processing history and, consequently, achieved varying transformation properties. Gradient annealing of SMA wires using tube furnace [4], joining of dissimilar SMA wires [5], inducing gradient heat treatment over an SMA wire by Joule Heating [6], establishment of a triple-SME applying R-phase [7], applying geometric gradient [8-12], and compositionally grading NiTi plates via surface diffusion of Ni through the plate thickness [13] can be mentioned as the reported attempts to enhance the functional properties of NiTi SMAs. Khan [14] introduced a laser induced controlled vaporization technique to manage the transformation temperatures of SMAs. Employing the high power density of an Nd:YAG laser, they could impart variations in the alloy's chemical composition resulting from the preferential vaporization of Nickel. Moreover, they studied the influences of laser parameters (pulse time, peak power, and the number of pulses per spot) on microstructure, transformation temperatures, and mechanical properties of laser-processed monolithic sheets [14]. This technique was utilized to produce various multiple memory NiTi-based devices [15-18]

Although NiTi based SMAs are vastly utilized in various smart structures in the form of wire or ribbon, major investigations on laser processing have been concentrated on sheets [1-2], [19-21]. There are limited works dedicated to study the processing of NiTi in the form of wires. As one of these attempts, Michael [22] applied pulsed Nd:YAG laser to process Nitinol wires. They focused on the superior vaporization of Ni in the course of laser processing and developed a model to predict changes in Ni concentration of the processed samples in terms of peak power and laser pulse duration. Moreover, Panton [23] studied the thermomechanical fatigue properties of NiTi laser welded joints. To this end, a NiTi wire containing a single laser-processed spot was investigated. They also explored the characterization of laser-processed NiTi wires. Based on their analysis results, a thermomechanical treatment was presented to enhance the properties of the products. Additionally, Pequegnat [24] investigated the use of pulsed Nd:YAG laser processing accompanying post-processing to adjust the local SME as well as PE properties of uniform NiTi wires. They utilized this technique to induce various memories in a desired section of a monolithic NiTi linear actuator. Deformation of the product was further characterized and compared with that of a single memory actuator. In another part of their work, microstructure and composition of the processed material were determined to uncover the influences of laser processing accompanied by cold working and heat treatment. Besides laser processing, there are several works regarding the effects of laser welding on the shape memory properties of Nitinol wires [25-28].

All the wires applied in the previous studies [22-24] were very thin with a diameter no bigger than 700 μm, commonly used for medical devices. However, for thicker NiTi wires, the energy required to process the wire as well as laser processing conditions would change. Although only one-sided laser processing was considered and studied in previous works, due to the small sizes of wires, more than one-side processing may be required to reach almost full penetration in rather thick wires. Therefore, distinct investigations are required to study the laser processing of such thick Nitinol wires.

The current research is dedicated to the utilization of Nd:YAG laser processing together with post heat treatment to alter local transformation temperatures and induce phase conversion in thick NiTi wires. To this end, various laser parameters are examined on a relatively thick Nitinol wire, and the thermal, microstructural, and compositional properties of the processed samples are investigated via characterization analyses. The effects of pulse width and peak power are investigated in order to impart changes in the transformation properties of the monolithic NiTi wire and induce phase transition. A four-sided laser processing pattern is presented to fully penetrate into the whole cross-section of the wire. Then, annealing is applied to recover the shape memory

property of the as-processed specimen. Finally, a laser-processed NiTi wire is successfully produced with new transformation temperatures so that the product shows SME at room temperature, unlike the as-received base material which exhibits PE properties.

2 MATERIALS AND METHODS

A 1.35 mm diameter Nitinol wire manufactured by Small Parts; Inc. was employed in this study. The samples were treated by the provider to exhibit pseudoelasticity at room temperature. The nominal chemical composition of the purchased alloy was 49.3 at. % (44.2 wt.%) Ti and 50.7 at. % (55.8 wt.%) Ni. The wires were cut into 60 mm length samples, and only 35 mm of the central length of each sample was laser processed. To eliminate a dark oxide layer developed during the process, the wires were acid pickled in a solution containing HNO3, HF, and H2O with volume percentages of 20%, 7.5%, and 72.5%, respectively, for 40 seconds before the laser processing. Then, any probably remaining contaminants were removed by cleaning the wires with Ethanol and de-ionized water.
A 400 W pulsed Nd:YAG laser system with a wavelength of 1.06 μm, a nominal spot diameter of 1.3 mm, and a square profile was utilized. The laser power was measured by a Gentec-EO pronto-500 power meter. As illustrated in "Fig. 1", the Nitinol wires were relied on a flat base plate, and two clamps held down their both ends to avoid any movement during laser processing.

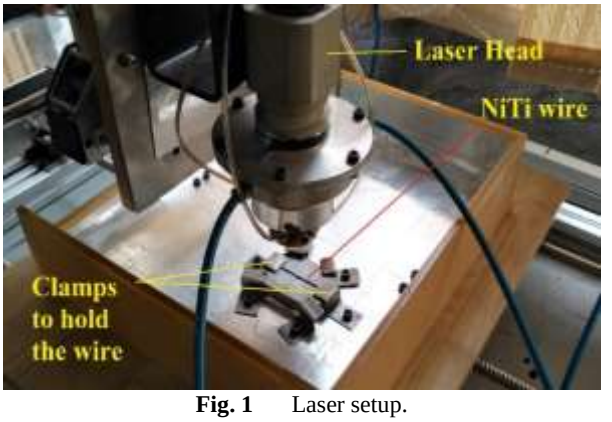

Fig. 1 Laser setup.

A 3-axis CNC machine provided controlled movement of the NiTi wires while the laser processing was done. The laser spots were overlapped by 60% to optimize the surface finish in the course of removing a brittle terminal solidification region. The wire was surrounded by a plastic chamber according to "Fig. 2". This chamber, filled with argon at the onset of laser processing, shielded the wire to minimize oxidation during the process. The flow rate of 10 lit/min for Argon shielding gas was found enough to avoid oxidation.

Fig. 2 Plastic chamber designed to avoid oxidation.

Differential Scanning Calorimetry (DSC) analysis at a controlled heating and cooling rate of 5°C/min was performed using a Mettler Toledo, DSC1 system equipped with a Refrigerated Cooling System (RCS). The chemical composition of the processed specimens was determined using EDAX Octane Elite system equipped with FEI Quanta 450 microscope. Santam universal testing machine model STM 50 equipped with a thermal chamber was employed to evaluate deformations of the as-received and the laser-processed wires. Tensile samples had a gauge length of 35 mm and were loaded at a strain rate of 1.5×10-3 1/s. The Effects of strain rate for a special kind of SMA [29] and gauge geometry in tensile test [30] were investigated previously. Tensile tests were carried out at the ambient temperature (25 °C). In order to investigate the microstructure of the processed specimens, metallographic samples were cross-sectioned, cold mounted in epoxy, and mechanically polished. Prior to mechanical polishing with colloidal alumina suspension, grinding with sequential sand paper of 400 to 1200-fine grit was performed. Finally, to reveal their microstructure, the samples were etched in a 3 mL HF, 14 mL HNO3, and 82 mL H2O solution for about 30 s.

3 RESULTS AND DISCUSSION

To investigate the influence of laser processing on the transformation temperatures of the NiTi specimens, first, the unprocessed base Nitinol wire was needed to be characterized. Figure 3a shows the DSC results for the as-received material.

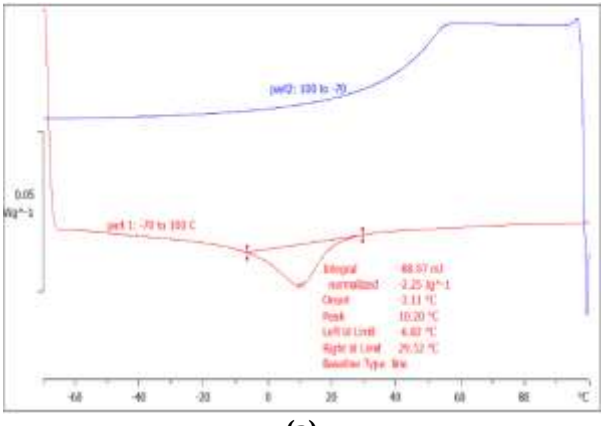

(a)

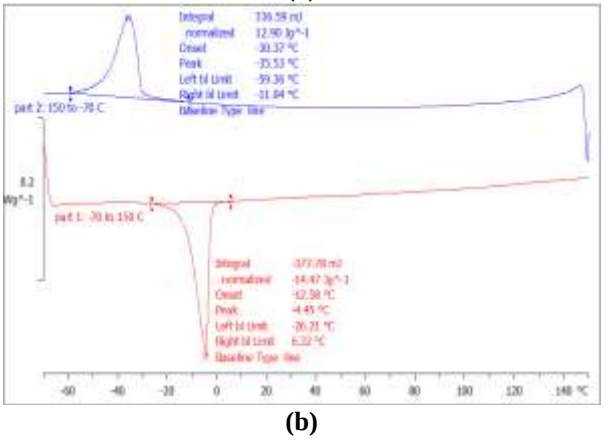

(b)

Fig. 3 DSC results for: (a): as-received material, and (b): HBM.

Table 1 Critical temperatures of HBM

	Transformation and Peak Temperatures, °C					
Sample	M_f	M_s	A_s	A_f	M_p	A_p
HBM	- 59.4	- 11	- 26.2	6.3	- 35.5	- 4.5

Due to thermomechanical processes in the course of wire fabrication, broad temperature peaks occur in the cooling cycle that do not allow for identifying the transformation temperatures. To remove such effects and to suppress the possible formation of R-phase, the as-received NiTi wire was heat treated at 800 °C for 1 hour followed by water quenching [1]. This heat-treated base material is referred to as HBM in the rest of this study. The DSC curves for HBM are plotted in "Fig. 3b". As observed, intense DSC peaks are obtained for HBM so the critical temperatures can be easily measured. These critical temperatures for HBM are listed in "Table 1" and are considered as the reference temperatures for the rest of the work. Referring to an SMA phase diagram [31], M_s, M_f, A_s and A_f are transformation temperatures and respectively represent the onset and the end of forward and reverse transformations in stress-free conditions.

Since these transformation temperatures depend on how the tangents to the DSC curves are taken, two other parameters as the peaks of forward and reverse martensitic transformation temperatures are also considered for comparative analyses. These two parameters, known as martensite peak temperature (M_p) and austenite peak temperature (A_p), can be derived by the DSC graphs where the first derivative is zero and are more reliable for comparison purposes.

Inspired by the laser parameters used in previous analyses for sheets and thin wires [14], [22-24], two initial sets of laser parameters are defined according to "Table 2". The Nitinol wires processed by these laser parameters are referred to as LP 1 and LP 2, respectively. As shown in "Table 2", a 10 ms pulse width with a 10 1/s frequency is similarly used for both parameter sets. However, two amounts of 1 kW and 1.2 kW are respectively applied as the peak power for LP 1 and LP 2. It is worth mentioning that these amounts of peak power are the highest ones that can be applied to preserve the material integrity for these certain values of pulse width and frequency.

Table 2 Two initial sets of laser parameters

	Laser Parameters		
Sample	Pulse width, ms	Peak Power, kW	Frequency, 1/s
LP 1	10	1	10
LP 2	10	1.2	10

To analyze the influence of laser processing with mentioned parameters on the transformation temperatures, a DSC test was conducted for LP 1 as well as LP 2 samples. The DSC results are illustrated in "Fig. 4", and the corresponding critical temperatures are summarized in "Table 3". By comparing the data of "Table 3" and "Table 1", it can be inferred that the laser processing has not affected the critical temperatures, especially the transformation peak temperatures, of LP 1 and LP 2 compared to those of the reference HBM sample. It has been shown that the composition change is the primary mechanism responsible for the alteration of SMA transformation properties via laser processing [1]. The high energy density of the laser can induce vaporization in SMA elements. Due to the larger vapor pressure of Nickel compared to that of Titanium, more Nickel vaporizes during laser processing resulting in a composition change in the material. Hence, no change in the transformation temperatures of LP 1 and LP 2 can be due to insufficient power provided by these laser parameters which cannot raise the temperature highly enough for element vaporization and composition change.

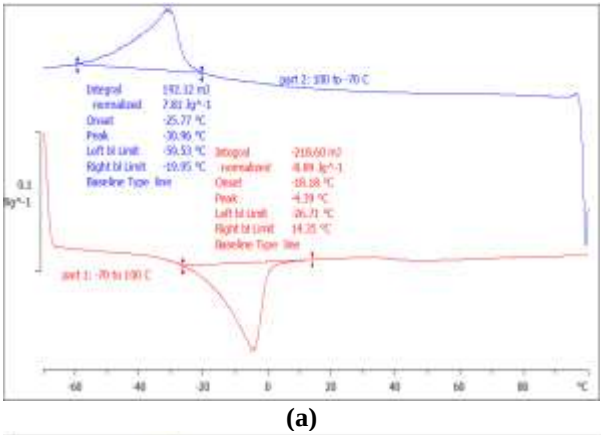

(a)

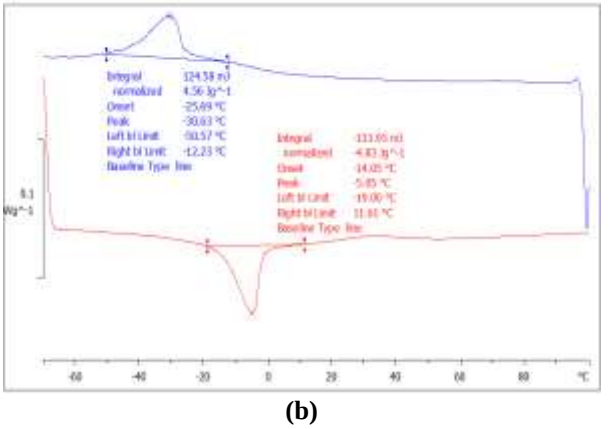

(b)

Fig. 4 DSC results for: (a): LP 1, and (b): LP 2.

I. **Table 3** Critical temperatures of LP 1 and LP 2

	Transformation and Peak Temperatures, °C					
Sample	M_f	M_s	A_s	A_f	M_p	A_p
LP 1	- 59.5	- 20	- 26.7	14.4	- 31	- 4.4
LP 2	- 50.6	- 12.2	- 19	11.6	- 30.6	- 5.1

Table 4 Second sets of laser parameters

	Laser Parameters		
Sample	Pulse width, ms	Peak Power, kW	Frequency, 1/s
LP 3	7	1.5	10
LP 4	8	1.5	10

Relative changes in material composition during laser processing mostly depend on a balance between the dilution of the molten pool and the vaporization flux of alloy elements [32-33]. Since these two issues are strongly associated with laser processing parameters [1], it is essential to study the effects of both pulse duration and peak power, as the key laser parameters, on the resultant transformation temperatures.

To investigate the effect of higher peak power, the amount of peak power was increased, and two new sets of processing conditions as LP 3 and LP 4 were defined according to "Table 4".

In contrast, the amount of pulse width was decreased slightly to avoid any breakage of the wire while processing. The samples LP 3 and LP 4 were subjected to DSC analysis, and the results are shown in "Fig. 5".

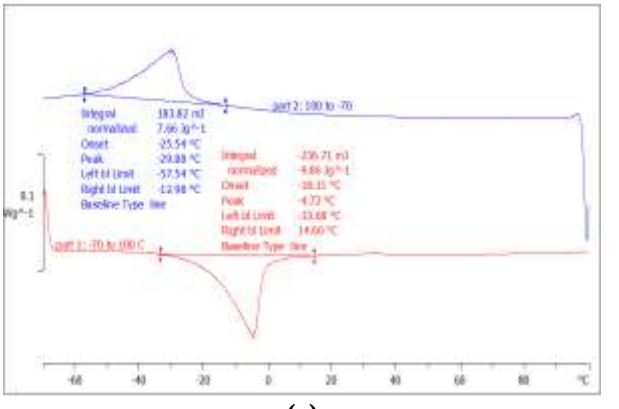

(a)

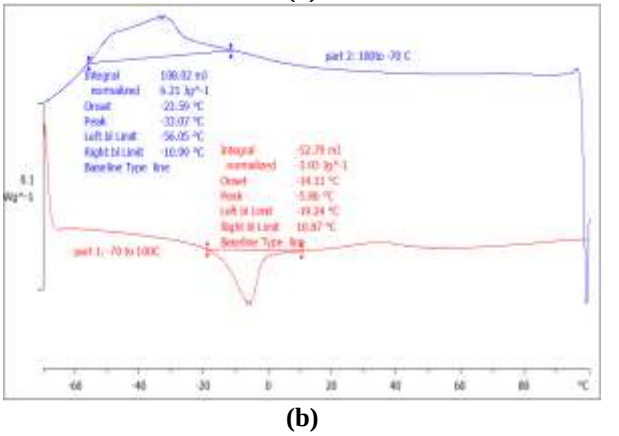

(b)

Fig. 5 DSC results for: (a): LP 3, and (b): LP 4.

The critical temperatures are extracted and reported in "Table 5". As noted, the transformation temperatures of the newly processed wires do not considerably vary compared to the reference temperatures. In depth comparison of transformation temperatures showed that, while M_f and M_s temperatures were almost the same as the reference temperatures, A_s showed a different approach for each of the two processed samples, and A_f showed a slight increase for both cases. As mentioned above, this inconsistency is attributed to the method of deriving the transformation temperatures and depends on how the tangents to the DSC graphs are taken. However, the transformation peak temperatures for HBM, LP 3, and LP 4 are closer than the one observed for the transformation temperatures, especially much closer for A_p values, which presents a difference of less than 2 °C. Consequently, all the transformation temperatures can be considered unchanged compared to the reference ones.

Table 5 Critical temperatures of LP 3 and LP 4

	Transformation and Peak Temperatures, °C					
Sample	M_f	M_s	A_s	A_f	M_p	A_p
LP 3	- 57.5	- 13	- 33.7	14.6	- 29.9	- 4.7
LP 4	- 56	- 11	- 19.2	10.8	- 33.1	- 5.9

The effect of higher pulse width, as another key parameter of laser processing, can be studied in the next step. Additionally, referring to a map of laser profiles presented by Michael [22], as seen in "Fig. 6", it is suggested that a longer pulse width results in better penetration while preserving the material integrity.

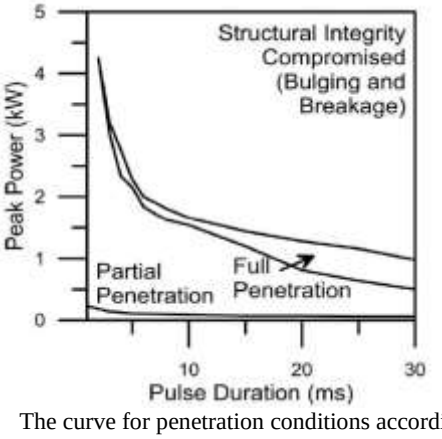

Fig. 6 The curve for penetration conditions according to the amount of peak power and pulse duration [22].

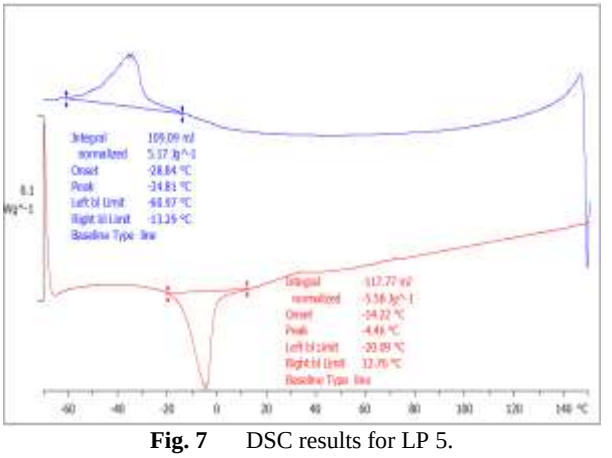

Fig. 7 DSC results for LP 5.

To this end, a new set of laser parameters with higher pulse width is introduced. This new set has a pulse duration of 20 ms, and a peak power of 0.5 kW with a 10 1/s frequency, which is referred to as LP 5 in the remainder of this study. It is worth mentioning that the amount of peak power adopted for this processing condition is lower than the one suggested by Michael map [22] ("Fig. 6"). However, it was observed that, for a 20 ms pulse width, the peak power of 0.5 kW is the highest value that preserves the material integrity of the current NiTi wire. Thermal analysis was carried out for the LP 5 specimen, and the DSC curve is exhibited in "Fig. 7".

The corresponding critical temperatures are derived and listed in "Table 6". Once more, it can be noted that the critical temperatures, especially the transformation peak temperatures, of the new sample LP 5 have almost not varied compared to the reference ones. This is in good agreement with previous empirical results [1] and is because of the fact that vaporization occurs during the initial instances of laser processing and significantly decreases by increasing the pulse time [1]. Therefore, while the vaporization flux decreases, the volume of the molten pool increases by increasing pulse width resulting in small changes in the transformation temperatures of Nitinol wires.

Table 6 Critical temperatures of LP 5

	Transformation and Peak Temperatures, °C					
Sample	M_f	M_s	A_s	A_f	M_p	A_p
LP 5	- 61	- 13.3	- 20.1	12.8	- 34.8	- 4.5

To investigate whether such laser processing is capable of vaporizing the alloy elements and changing its composition, LP 5 sample is subjected to EDX analysis. As shown in "Fig. 8", EDX scan analysis was performed across a surface line including both the processed and the unprocessed parts of the sample. According to this figure, Nickel reduction can be detected whereas the average unprocessed Nickel content (55.8 wt.%) was significantly higher than that of the processed section of Nitinol wire. Thus, compositional analysis results confirmed that preferential Ni vaporization occurred due to laser processing. However, since EDX analysis was performed on the outer surface of the specimen, to examine the depth of these composition changes and to uncover the laser penetration, the cross-section of the processed wire must be microstructurally studied.

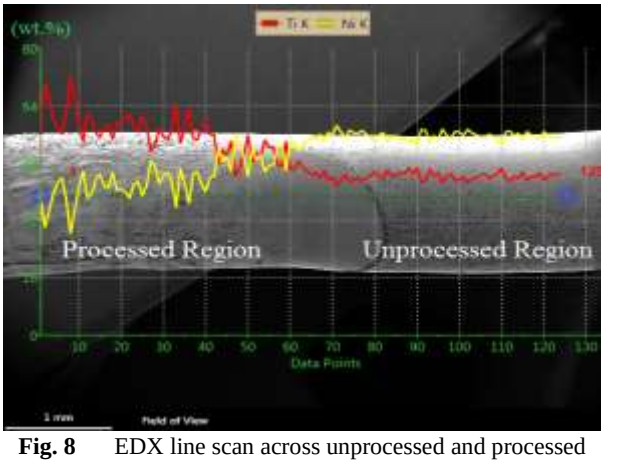

Fig. 8 EDX line scan across unprocessed and processed regions of LP 5.

The metallographic examination was conducted on the cross section of LP 5 specimen to better recognize the effect of laser processing on the microstructure and the amount of laser penetration through the thickness of NiTi wire. Optical micrographs showing the cross section of the processed wire after etching are provided in "Fig. 9".

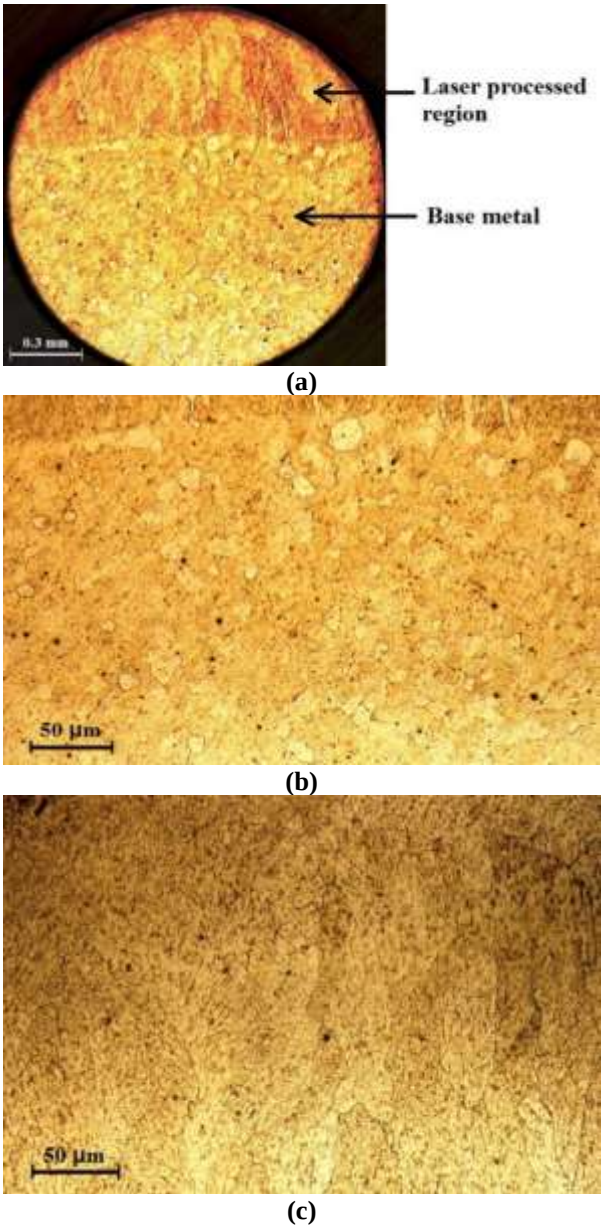

Fig. 9 Microstructure of cross-sectioned LP 5 sample: (a): whole cross section, (b): magnified image of the base metal, and (c): magnified image of the laser processed region.

According to "Fig. 9a", the wire cross section can be divided into two distinct parts. Referring to higher optical magnification of each part, "Fig. 9b" and c, it can be concluded that the main part of the wire shows an equiaxed B2 austenite grain structure which is attributed to unprocessed base material. However, the upper part of the wire exposed to laser spot shows columnar dendritic microstructure, which is typical for processed NiTi wires [24]. Therefore, the laser beam can only process the smaller section of such thick Nitinol wires and the larger part remains unprocessed.

It is worth mentioning that, to cover the whole surface of the wire by laser spot, the spot diameter must be approximately the same as the wire diameter. Due to the relatively large sizes of the wires in the current study, the laser spot diameter (1.3 mm) is at least two times greater than the maximum spot diameter (600 µm) employed for processing thin NiTi wires [22-24]. Since the amount of laser energy applied in the present work is relatively in the same order as those for thin wires, the efficient energy density decreases to at least one-quarter. The low energy density of the laser beam leads to the fact that full penetration cannot be attained in the case of thick NiTi wires by only one-sided laser processing.

To overcome this challenge, a four-sided laser processing technique is proposed to process almost the entire thick NiTi wires and can alter transformation properties compared to those of the reference sample. According to this approach, the laser is irradiated in four equally angel sides of the wire. When the processing of one side has been completed, the wire is rotated by 90 degrees and the new side is processed. This procedure is repeated for each of the four sides of the wire. The four-sided laser-processed NiTi wire, which has the same laser parameters as LP 5 sample, is called LP 6 in the rest of the work. Thermal analysis reveals that DSC peaks of LP 6 become shallow and wide, as depicted in "Fig. 10".

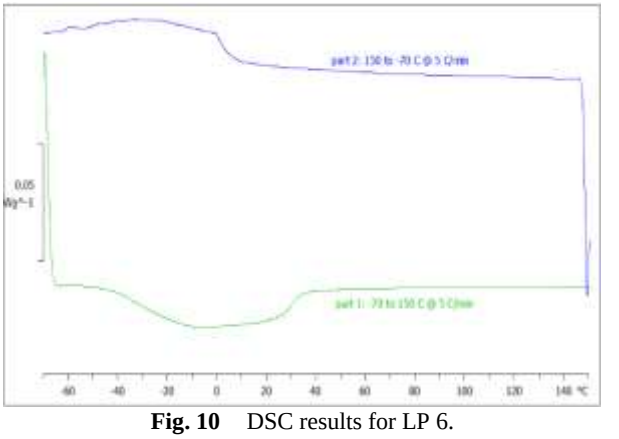

Fig. 10 DSC results for LP 6.

In other words, the laser processing caused the shape memory properties of LP 6 to be weakened. This may be attributed to rapid solidification of the molten metal after laser processing. This event can lead to inhomogeneity through the fusion zone, which is itself because of micro segregation of the alloy's elements while the solidification front is growing [23]. Due to this

inhomogeneity, internal strain/stress fields form in the alloy. These internal fields prevent the mobility of the crystals in the course of the heating and cooling cycles [34] and can even suppress the phase transition. Moreover, LP 6 sample becomes very brittle and can be easily broken when imposed to smooth bending. This brittleness may be attributed to the creation of brittle intermetallic compounds including Ti2Ni [14].

Taking all of the above into consideration, it can be inferred that a thermomechanical treatment needs to be employed to recover the shape memory effect and the ductility of the processed specimen. Annealing at 1000 °C for 1 hour followed by slow furnace cooling was found to be the best option to address all the aforementioned issues. The annealing treatment at this temperature eliminates the internal strain/stress fields from the material, improves material ductility, and also homogenizes the microstructure. The LP 6 sample which is heat treated according to the aforementioned pattern is referred to as HLP 6.

The DSC curve for HLP 6 is plotted in "Fig. 11". As illustrated, annealing heat treatment decreases the width of the transformation peaks and recovers the shape memory properties of the specimen. The critical temperatures are extracted and listed in "Table 7".

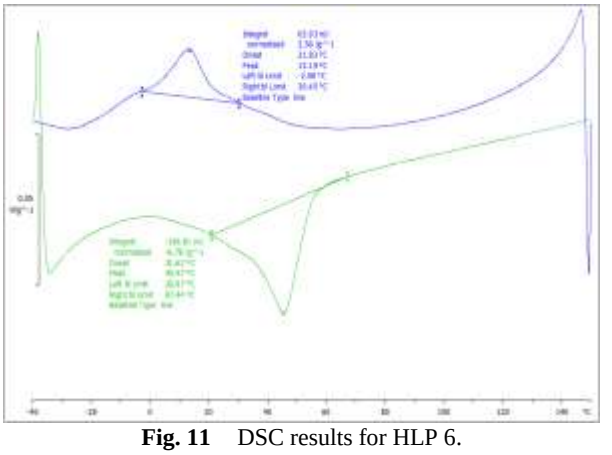

Fig. 11 DSC results for HLP 6.

Table 7 Critical temperatures of HLP 6

	Transformation and Peak Temperatures, °C					
Sample	M_f	M_s	A_s	A_f	M_p	A_p
HLP 6	- 3	30.5	20.9	67.4	13.2	45.5

Recalling reference temperatures in "Table 1", it can be noticed that the transformation peak temperatures of HLP 6 increase by about 50 °C compared to those of HBM sample. The transformation temperatures, showing scattered data, increase by a range of 40 – 60 °C compared to the reference ones. Consequently, an almost constant increase of 50 °C, can be considered for all the transformation temperatures. This confirms the successful application of Nd:YAG laser processing accompanied by post-heat treatment to alter the transformation temperatures of the thick NiTi wire.Although the base material exhibits PE at room temperature, 50 °C increase in the transformation temperatures causes a phase conversion in HLP 6 specimen so that it shows SME at room temperature.

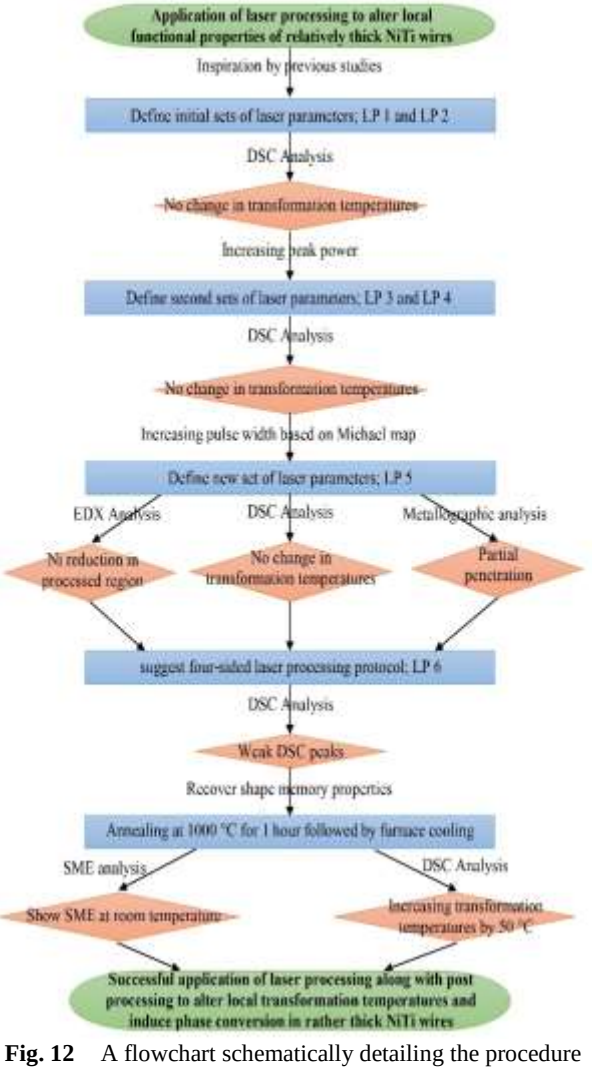

Fig. 12 A flowchart schematically detailing the procedure of altering the transformation properties of thick NiTi wires.

This can be verified by simply bending the HLP 6 to induce a small amount of residual strain and then heating it above A_f. The bent wire recovers almost all the residual strains and regains its initial straight condition upon heating. Hence, the four-sided laser processing protocol can locally alter the transformation temperatures, which can be applied to impart additional memories into a monolithic NiTi wire and to produce multiple memory materials. The corresponding

flowchart, which schematically details the procedure of altering the transformation properties of thick NiTi wires, is shown in “Fig. 12”. To study the influence of laser processing on mechanical properties of NiTi samples, tensile tests were carried out for both HLP 6 and HBM, and the results are compared in “Fig. 13”.

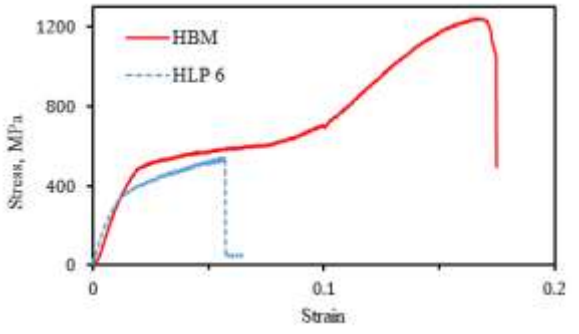

Fig. 13 Stress-strain curves for HBM and HLP 6 samples.

As depicted, the ultimate tensile stress and strain decreased significantly for HLP 6 compared to those of HBM. This reduction can be attributed to several factors including dislocation destruction, grain growth [2], segregation of solute in the course of solidification, and dendritic structure [14] in the processed metal. However, the strength and other mechanical features of the processed wire may be improved by cold working such as wire drawing.

It is worth mentioning that, the critical stress to form the stress induced martensite for HLP 6 is lower than that of HBM. This is consistent with increasing in transformation temperatures of the laser processed specimen. Referring to an SMA phase diagram [31], higher transformation temperatures lead to lower critical stresses required for phase transition to stress-induced martensite at a specific temperature.

4 CONCLUSIONS

Nd:YAG laser processing followed by post-processing heat treatment is successfully applied in current study to alter local functional properties of relatively thick NiTi wires. To this end, various laser parameters are applied, and the effects of pulse width and peak power are studied. DSC results reveal that no transformation temperature variations occur in one-sided laser processed thick wires. Further EDS analyses confirmed that preferential Nickel vaporization occurred in the processed region of the NiTi wire. However, based on metallographic results, laser beam processed a small part of cross section of the wire whereas these laser parameters provide the maximum input energy while preserving the structural integrity of the wire. It can be concluded that one-sided laser processing cannot affect the transformation temperatures of such thick NiTi wires because of the low energy density of the laser beam. To address this issue, a four-sided laser processing technique is presented which processes the four equal-angle sides of the wire.

After such four-sided processing, however, the shape memory properties weaken due to the generation of internal strains/stresses as a result of rapid solidification after laser processing. Post-processing annealing treatment at 1000 °C followed by furnace cooling was applied to recover the shape memory properties and ductility of the processed specimen. Finally, a heat-treated laser-processed NiTi wire was produced with 50 °C higher transformation temperatures and stable martensite phase at room temperature. Deformation of the processed wire reveals that the strength and ductility decrease considerably compared to the unprocessed base material. It shows that, despite unique advantages, laser processing has several detrimental influences including dislocation destruction, grain growth, and solute segregation that lead to a lower mechanical strength. The present work proposes an approach to produce multiple shape memory effects in thick NiTi wires.

REFERENCES

[1] Khan, M. I., Pequegnat, A., and Zhou, Y. N., Multiple Memory Shape Memory Alloys, Advanced Engineering Materials, Vol. 15, No. 5, 2013, pp. 386-393.

[2] Pequegnat, A., Panton, B., Zhou, Y. N., and Khan, M. I., Local Composition and Microstructure Control for Multiple Pseudoelastic Plateau and Hybrid Self-Biasing Shape Memory Alloys, Materials and Design, Vol. 92, 2016, pp. 802-813.

[3] Miura, F., Mogi, M., and Ohura, Y., Japanese NiTi Alloy Wire: Use of The Direct Electric Resistance Heat Treatment Method, The European Journal of Orthodontics, Vol. 10, No. 1, 1988, pp. 187-191.

[4] Mahmud, A. S., Liu, Y., and Nam, T. H., Design of Functionally Graded NiTi by Heat Treatment, Physica Scripta, T129, 2007, pp. 222.

[5] Sevilla, P., Martorell, F., Libenson, C., Planell, J. A., and Gil, F. J., Laser Welding of NiTi Orthodontic Archwires for Selective Force Application, Journal of Materials Science: Materials in Medicine, Vol. 19, 2008, pp. 525-529.

[6] Kang, S. W., Cho, G. B., Yang, S. Y., Liu, Y., Yang, H., Miyazaki, S., and Nam, T. H., Transformation Temperatures and Shape Memory Characteristics of a Ti–45Ni–5Cu (at%) Alloy Annealed by Joule Heating, Physica Scripta, T139, 2010, pp. 014068.

[7] Tang, C., Huang, W. M., Wang, C. C., and Purnawali, H., The Triple-Shape Memory Effect in NiTi Shape

Memory Alloys, Smart Materials and Structures, Vol. 21, No. 8, 2012, pp. 085022.

[8] Shariat, B. S., Liu, Y., and Rio, G., Mathematical Modelling of Pseudoelastic Behaviour of Tapered NiTi Bars, Journal of Alloys and Compounds, Vol. 577, 2013, pp. 76-82.

[9] Shariat, B. S., Liu, Y., and Rio, G., Modelling and Experimental Investigation of Geometrically Graded NiTi Shape Memory Alloys, Smart Materials and Structures, Vol. 22, No. 2, 2013, pp. 025030.

[10] Shariat, B. S., Liu, Y., and Bakhtiari, S., Modelling and Experimental Investigation of Geometrically Graded Shape Memory Alloys with Parallel Design Configuration, Journal of Alloys and Compounds, Vol. 791, 2019, pp. 711-721.

[11] Shariat, B. S., Bakhtiari, S., Yang, H., ansd Liu, Y., Computational and Experimental Analyses of Martensitic Transformation Propagation in Shape Memory Alloys, Journal of Alloys and Compounds, Vol. 806, 2019, pp. 1522-1528.

[12] Shariat, B. S., Bakhtiari, S., Yang, H., and Liu, Y., Controlled Initiation and Propagation of Stress-Induced Martensitic Transformation in Functionally Graded NiTi, Journal of Alloys and Compounds, Vol. 851, 2021, pp. 156103.

[13] Meng, Q., Wu, Z., Bakhtiari, R., Shariat, B. S., Yang, H., Liu, Y., and Nam, T. H., A Unique "Fishtail-Like" Four-Way Shape Memory Effect of Compositionally Graded NiTi, Scripta Materialia, Vol. 127, 2017, pp. 84-87.

[14] Khan, M. I., Pulsed Nd: YAG Laser Processing of Nitinol, Ph.D. Dissertation, Mechanical and Mechatronics Engineering Dept., University of Waterloo, Waterloo, Ontario, Canada, 2011.

[15] Daly, M., Pequegnat, A., Zhou, Y. N., and Khan, M. I., Fabrication of a Novel Laser-Processed NiTi Shape Memory Microgripper with Enhanced Thermomechanical Functionality, Journal of Intelligent Material Systems and Structures, Vol. 24, No. 8, 2013, pp. 984-990.

[16] Panton, B., Zhou, Y. N., and Khan, M. I., A Stabilized, High Stress Self-Biasing Shape Memory Alloy Actuator, Smart Materials and Structures, Vol. 25, No. 9, 2016, pp. 095027.

[17] Zeng, Z., Oliveira, J. P., Ao, S., Zhang, W., Cui, J., Yan, S., and Peng, B., Fabrication and Characterization of a Novel Bionic Manipulator Using a Laser Processed NiTi Shape Memory Alloy, Optics and Laser Technology, Vol. 122, 2020, pp. 105876.

[18] Ge, F., Peng, B., Ke, W., Teshome, F. B., Du, X., and Zeng, Z., Design and Fabrication of Bionic Finger Driven by NiTi Shape Memory Alloys, Proceedings of the Eighth Asia International Symposium on Mechatronics, Springer Nature Singapore, Singapore, 2022, pp. 616-627.

[19] Khan, M. I., Zhou, Y., Effects of Local Phase Conversion on The Tensile Loading of Pulsed Nd: YAG Laser Processed Nitinol, Materials Science and Engineering: A, Vol. 527, No. 23, 2010, pp. 6235-6238.

[20] Michael, A., Pequegnat, A., Wang, J., Zhou, Y. N., and Khan, M. I., Corrosion Performance of Medical Grade NiTi After Laser Processing, Surface and Coatings Technology, Vol. 324, 2017, pp. 478-485.

[21] Mehrpouya, M., Gisario, A., Brotzu, A., and Natali, S., Laser Welding of NiTi Shape Memory Sheets Using a Diode Laser, Optics and Laser Technology, Vol. 108, 2018, pp. 142-149.

[22] Michael, A., Laser Processing and Modelling of Multiple Memory Shape Memory Alloys, Ph.D. Dissertation, Mechanical and Mechatronics Engineering Dept., University of Waterloo, Waterloo, Ontario, Canada, 2018.

[23] Panton, B., Laser Processing, Thermomechanical Processing, and Thermomechanical Fatigue of NiTi Shape Memory Alloys, Ph.D. Dissertation, Mechanical and Mechatronics Engineering Dept., University of Waterloo, Waterloo, Ontario, Canada, 2016.

[24] Pequegnat, A., Novel Laser Based NiTi Shape Memory Alloy Processing Protocol for Medical Device Applications, Ph.D. Dissertation, Mechanical and Mechatronics Engineering Dept., University of Waterloo, Waterloo, Ontario, Canada, 2014.

[25] Shamsolhodaei, A., Zhou, Y. N., and Michael, A., Enhancement of Mechanical and Functional Properties of Welded NiTi by Controlling Nickel Vapourisation, Science and Technology of Welding and Joining, Vol. 24, No. 8, 2019, pp. 706-712.

[26] Shamsolhodaei, A., Razmpoosh, M. H., Maletta, C., Magarò, P., and Zhou, Y. N., A Comprehensive Insight into The Superelasticity Measurement of Laser Welded NiTi Shape Memory Alloys, Materials Letters, Vol. 287, 2021, pp. 129310.

[27] Vâlsan, D. D., Bolocan, V. M., Novac, A., Chilnicean, G. A., and Crăciunescu, C. M., Analysis of Pulsed Laser Spot Effects on NiTi Wires, Solid State Phenomena, Vol. 332, 2022, pp. 59-66.

[28] Ge, F., Zeng, Z., Peng, B., Teshome, F. B., and Chen, L., Study on The Effect of Double-Sided Laser Welding of NiTi Shape Memory Alloys Wire, The International Journal of Advanced Manufacturing Technology, Vol. 120, No. 11-12, 2022, pp. 8201-8209.

[29] Amrollahipour, R., Kadkhodaei, M., Influence of Strain Rate on Stress–Strain Response of Ni–Mn–Ga Ferromagnetic Shape Memory Alloy Single Crystals, Iranian Journal of Science and Technology, Transactions of Mechanical Engineering, Vol. 41, 2017, pp. 265-268.

[30] Jamalimehr, A., Ravanbakhsh, H., Kadkhodaei, M., and Kamrani, M., Investigation of Dog-Bone Geometry for Simple Tensile Test of Pseudoelastic Shape Memory Alloys, Iranian Journal of Science and Technology, Transactions of Mechanical Engineering, Vol. 40, 2016, pp. 337-345.

[31] Brinson, L. C., One-Dimensional Constitutive Behavior of Shape Memory Alloys: Thermomechanical Derivation with Non-Constant Material Functions and Redefined Martensite Internal Variable, Journal of Intelligent Material Systems and Structures, Vol. 4, No. 2, 1993, pp. 229-242.

[32] He, X., Deb Roy, T., and Fuerschbach, P. W., Composition Change of Stainless Steel During Microjoining with Short Laser Pulse, Journal of Applied Physics, Vol. 96, No. 8, 2004, pp. 4547-4555.

[33] Jandaghi, M., Parvin, P., Torkamany, M. J., and Sabbaghzadeh, J., Alloying Element Losses in Pulsed Nd: YAG Laser Welding of Stainless Steel 316, Journal of Physics D: Applied Physics, Vol. 41, No. 23, 2008, pp. 235503.

[34] Sadiq, H., Wong, M. B., Al-Mahaidi, R., and Zhao, X. L., The Effects of Heat Treatment on The Recovery Stresses of Shape Memory Alloys, Smart Materials and Structures, Vol. 19, No. 3, 2010, pp. 035021.

Int. J. Advanced Design and Manufacturing Technology, 2024, Vol. 17, No. 1, pp. 51-57

DOI: ***ISSN: 2252-0406*** ***https://sanad.iau.ir/journal/admt***

Numerical Motion Analyzing Based on Recorded Empirical Data by Smartphone Features

Bahador Abolpour*
Department of Chemical Engineering,
Sirjan University of Technology, Sirjan, Iran
E-mail: bahadorabolpor1364@yahoo.com
*Corresponding author

Yasser Taghipour
Department of Mechanical Engineering,
Sirjan University of Technology, Sirjan, Iran
E-mail: ytaghipour@sirjantech.ac.ir

Received: 22 December 2022, Revised: 26 February 2023, Accepted: 10 March 2023

Abstract: This study presents a new method to analyse the motion of moving objects. The novelty of this study is that the presented work obtains your location based on the coupled measured data using the GPS and other motion sensors of a smart phone. This method can be used for GPS free navigations in future studies. The smartphone sensors measure the desired values and a developed Android application records this data. A developed MATLAB code analyses these values for car road travel using multiple coordinate transformations and removes the effects of Earth's gravity from the measured acceleration. It is recognized that the presented method can be used to analyse the movement and performance of the studied material. The obtained results show that the integration of data recorded by the accelerometer sensor integrates the effects of noise and this sensor is not a convenient feature to obtain the instantaneous location. Calculating the acceleration using GPS data may also not be accurate in this case. Getting the location and acceleration using a GPS sensor and accelerometer is more accurate.

Keywords: Global Positioning System, Motion Analysis, Sensor, Smartphone

Biographical notes: Bahador Abolpour received his PhD in Chemical Engineering from Shahid Bahonar University of Kerman of Iran in 2017. He is currently Associate Professor at the Department of Chemical Engineering, Sirjan University of Technology, Sirjan, Iran. His current research interest includes Rapid prototyping and Rapid Tooling. **Yasser Taghipour** is Assistant Professor of Mechanical Engineering at the Sirjan University of Technology, Iran. He received his PhD in Mechanical engineering from Shahid Bahonar University of Kerman of Iran in 2017 and MSc in Mechanical Engineering from University of Tehran of Iran in 2004. His current research focuses on the computational and solid mechanics.

Research paper

1 INTRODUCTION

Advances in computer and electronic science in recent years have made smartphones an essential part of people's daily lives. Competition among manufacturers to improve performance and services has made it possible to use these devices in various fields. On the other hand, the development of the space industry helped with human transportation and exploration. There are no Global Positioning System (GPS) blind spots on the planet today. Industry Science Research Business Navigation is essential for most human activities such as transportation and travel. Autonomous devices in particular need navigation to manage constant motion. Motion analysis using smartphone sensors is a simple solution to this problem. So, computer electronics and aerospace technology have come together to solve this problem. The smartphone includes an on-screen display, haptic feedback system, processor, graphics and audio chipset and advanced connectivity as standard features. Some of these phones have additional features such as barometer and thermometer, or inertial motion unit (IMU) containing magnetometer, 3D accelerometer and gyroscope. This type of smartphone is great for analysing motion.

Several studies have investigated postural and gait control [1-2] or joint goniometry [3-4]. However, some researchers use expensive equipment such as aircraft black boxes or stationary equipment for laboratory studies [5]. Some researchers use smartphones for static and dynamic measurements in objects moving analysis. Rapid location acquisition [6] and data recording are important factors for intelligent transportation. Sensor networks are needed to observe traffic [7] or to detect traffic quality [8]. This is a new use of smartphones in the topic of traffic control. Then they analyse driver behaviour [9] or detect car accidents [10] using smartphone capabilities. Some reasons to explore new motion analysis methods are controlling an intelligent car, designing an autopilot system for an airplane or drone, testing the performance of a moving vehicle, controlling a multirotor self-balancing system for a bicycle or motorcycle system design, and clinical analysis using human behaviour. Smartphones are accessible and convenient devices, containing several sensors that can measure valuable data for motion analyzing purposes. It is important to study its ability to record data and motion analysis. In our previous study, we presented a novel approach for navigation of a vehicle using the smartphone sensors, with a low dependency to the GPS data [11].

The present study describes a new method for analyzing the motion of moving objects such as buses, cars, ships, motorcycles, multirotor, boats, helicopters, or airplanes. In this study, we present a new method to analyze the motion of these moving objects. The novelty of this study is that the presented work obtains the location of moving object based on the coupled measured data using the GPS and other motion sensors of a smart phone. It should be noted that in this method, it is possible to calibrate the sensors measurements using the converted data from GPS signals, and then this method can be used for GPS free navigations in future studies. Previous studies in this field have no attention to this matter. A JavaScript code has been generated and then the developed Android application is installed on a smartphone to record the values measured by its sensors for utilizing by a generated MATLAB code to analyze a car's trip.

2 METHODOLOGIES

2.1. Experiment

A Samsung smartphone (Galaxy S III I9300) was used in this study. The sensor measured parameters essential for analyzing the road journey of a Peugeot car (405 GLX) from Estahban to Neyriz in Iran. Android application is developed with homemade code using JavaScript. This application installed on the smartphone displays the necessary information on the screen, and writes it to an external memory. These data are time, data logging rate, latitude, longitude, altitude, acceleration in x_s, y_s, and z_s directions, roll and yaw, pressure, and temperature. The phone is mounted at the estimated center of gravity of the vehicle. Figure 1 shows the smartphone coordinate system (x_s, y_s and z_s directions) and the roll, pitch and yaw directions.

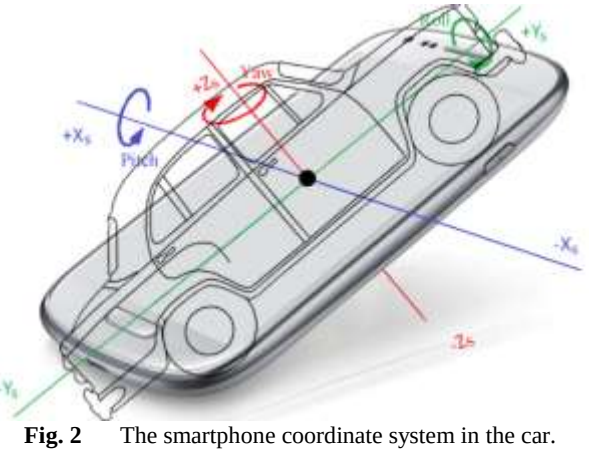

Fig. 2 The smartphone coordinate system in the car.

2.2. Coordinate Transformation

The coordinate transformation has been presented in "Fig. 2", schematically. GPS data is in the world coordinate system, which designates each point with 3 elements as [12]:

$$\vec{P_g} = \begin{pmatrix} \lambda \\ \phi \\ h \end{pmatrix} \quad (1)$$

Where, λ, φ and h are the longitude, latitude and height, respectively. The Earth-centered Earth-fixed coordinate system (ECEF) expresses this as [13]:

$$\vec{P_e} = \begin{pmatrix} x_e \\ y_e \\ z_e \end{pmatrix} = \begin{pmatrix} (N_e + h)Cos\phi Cos\lambda \\ (N_e + h)Cos\phi Sin\lambda \\ [N_e(1 - e^2) + h]Sin\phi \end{pmatrix} \quad (2)$$

The origin of the coordinate system (x_e, y_e, and z_e) is located at the Earth's center of mass (see "Fig. 2"), which is not a sphere but a biaxial ellipse, therefore, $N_e = r_e/\sqrt{(1 - e^2)Sin^2\phi}$ and $e=0.081819190842622$ are inserted for correction. Where, r_e=6378137 m is the Earth's mean radius.

This point in the north east down (NED) coordinate system has been represented as [13]:

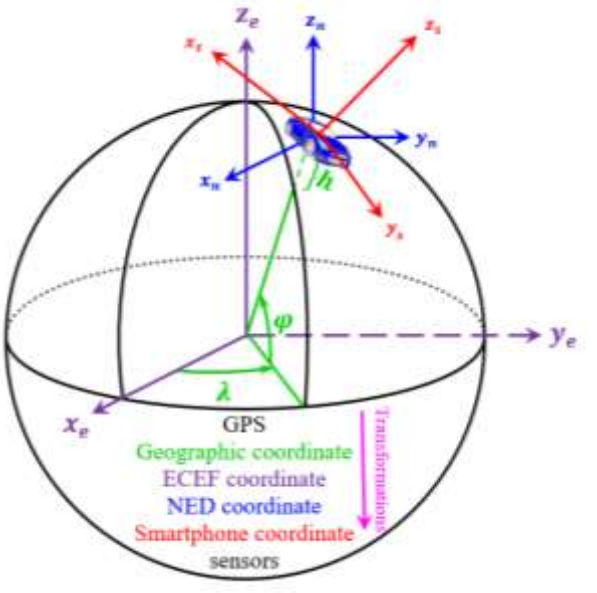

Fig. 2 The coordinate transformations.

$$\vec{P_n} = \begin{pmatrix} x_n \\ y_n \\ z_n \end{pmatrix} = \begin{pmatrix} -Sin\phi^{ref}Cos\lambda^{ref} & -Sin\phi^{ref}Sin\lambda^{ref} & Cos\phi^{ref} \\ -Sin\lambda^{ref} & Cos\lambda^{ref} & 0 \\ -Cos\phi^{ref}Cos\lambda^{ref} & -Cos\phi^{ref}Sin\lambda^{ref} & -Sin\phi^{ref} \end{pmatrix} \cdot \begin{pmatrix} x_e - x_e^{ref} \\ y_e - y_e^{ref} \\ z_e - z_e^{ref} \end{pmatrix} \quad (3)$$

As shown in the "Fig. 2", The origin of the vehicle-mounted NED coordinate system (x_n, y_n, and z_n) is on the smartphones center of mass. The starting point and angle of the smartphone in this road trip in the local NED coordinate system is x_e^{ref},y_e^{ref}, z_e^{ref}, ϕ^{ref}, and λ^{ref}. Each point in our trip now has a 3D displacement vector from the starting point, which the slope of this displacement vs. time defines the vehicle velocity (V_n, in the NED coordinate system). All coordinate conversion steps up to this section use only GPS data. We can use position measurements and convert them to the phones coordinate system (V_s) using the following Equation [14].

$$\vec{V_s} = \begin{pmatrix} V_{sx} \\ V_{sy} \\ V_{sz} \end{pmatrix} = \begin{pmatrix} Cos\theta Cos\psi & Cos\theta Sin\psi & -Sin\theta \\ Sin\varphi Sin\theta Cos\psi - Cos\varphi Sin\psi & Sin\varphi Sin\theta Sin\psi + Cos\varphi Cos\psi & Sin\varphi Cos\theta \\ Cos\varphi Sin\theta Cos\psi + Sin\varphi Sin\psi & Cos\varphi Sin\theta Sin\psi - Sin\varphi Cos\psi & Cos\varphi Cos\theta \end{pmatrix} \cdot \begin{pmatrix} V_{nx} \\ V_{ny} \\ V_{nz} \end{pmatrix} \quad (4)$$

As shown in "Figs. 1 and 2", V_{sx}, V_{sy}, and V_{sz} are components of the car velocity vector in the x_s, y_s and z_s directions, and ϕ, θ and ψ are roll, pitch and yaw angles, respectively. The slope of V_s vs. t defines the car acceleration (a_{GPS}, in the smartphone coordinate system) which is in a same coordinate system with $a_{accelerometer}$ (the measured acceleration using the accelerometer sensor). Calculating a_{GPS} requires double differentiation (the slope of the displacement vs. time gives the velocity and the slope of the velocity vs. time gives the acceleration), but, $a_{accelerometer}$ has been measured directly. Therefore, we can validate the a_{GPS} and clear its immediate error. As shown in "Figs. 1 and 2", accelerometer sensors provide acceleration vector components (a_{sx}, a_{sy} and a_{sz}) in the smartphone coordinate system, which are affected by the local gravitational acceleration (g) that has the following various with changing altitudes [15]:

$$g = g^{ref}\left(\frac{r_e + h^{ref}}{r_e + h}\right)^2 \quad (5)$$

Where, g^{ref} is the gravitational acceleration at the beginning of the road trip (at h^{ref}). To remove this effect, a_{sx}, a_{sy}, and a_{sz} were transformed from the smartphone coordinate system to the NED coordinate system (see "Fig. 2"), using φ, θ and ψ angles, as below [15]:

$$\vec{a_n} = \begin{pmatrix} a_{nx} \\ a_{ny} \\ a_{nz} \end{pmatrix} = \begin{pmatrix} Cos\psi Cos\theta & Cos\psi Sin\theta Sin\varphi - Sin\psi Cos\varphi & Cos\psi Sin\theta Cos\varphi + Sin\psi Sin\varphi \\ Sin\psi Cos\theta & Sin\psi Sin\theta Sin\varphi + Cos\psi Cos\varphi & Sin\psi Sin\theta Cos\varphi - Cos\psi Sin\varphi \\ Sin\theta & Cos\theta Sin\varphi & Cos\theta Cos\varphi \end{pmatrix} \cdot \begin{pmatrix} a_{sx} \\ a_{sy} \\ a_{sz} \end{pmatrix} \quad (6)$$

Attending to the parallel directions of a_{nz} and g vectors, it is possible to remove the mentioned effect as $a_{nz}^{cor} = a_{zn} - g$, and then, transfer the corrected acceleration from the NED coordinate system to the smartphone coordinate system (see "Fig. 2"):

$$\vec{a_s^{cor}} = \begin{pmatrix} a_{sx}^{cor} \\ a_{sy}^{cor} \\ a_{sz}^{cor} \end{pmatrix} = \begin{pmatrix} Cos\theta Cos\psi & Cos\theta Sin\psi & -Sin\theta \\ Sin\varphi Sin\theta Cos\psi - Cos\varphi Sin\psi & Sin\varphi Sin\theta Sin\psi + Cos\varphi Cos\psi & Sin\varphi Cos\theta \\ Cos\varphi Sin\theta Cos\psi + Sin\varphi Sin\psi & Cos\varphi Sin\theta Sin\psi - Sin\varphi Cos\psi & Cos\varphi Cos\theta \end{pmatrix} \cdot \begin{pmatrix} a_{nx}^{cor} \\ a_{ny} \\ a_{nz} \end{pmatrix} \quad (7)$$

It should be noted that a_{nx} and a_{ny} are perpendicular to the g direction, and therefore these parameters are free from the g effects.

2.3. Predictions of Pressure and Temperature

Pressure and temperature sensors are a common feature of today's smartphones. The used smartphone has a pressure sensor. Nevertheless, this phone does not have a temperature sensor. Therefore, the external thermometer (Testo 905i) is connected to the smartphone using a Bluetooth connection. Sometimes the measured temperature and pressure are ambient (external) values, e.g., a bicycle or car with the windows open. In this case, these values can be used to calculate outdoor air properties such as density or viscosity. In other cases, such as in jet aircraft, this measurement is an indoor value. Comparing the indoor and outdoor values of this parameter yields some of the stresses contained within the material body, such as normal and thermal stresses. The following Equations estimate the outdoor values of temperature and pressure at each altitude [16]:

$$\begin{bmatrix} T^{est} \\ P^{est} \end{bmatrix} = \begin{cases} \begin{bmatrix} T^{ref} - 0.0065h \\ P^{ref}\left(\frac{T^{est}+273.15}{288.16}\right) \end{bmatrix} & h < 11000 \\ \begin{bmatrix} -56.49 \\ P^{ref}\left(\frac{T^{est}+273.15}{216.16}\right) \end{bmatrix} & 11000 < h < 25000 \\ \begin{bmatrix} -56.49 + 0.003(h - 25000) \\ P^{ref}\left(\frac{T^{est}+273.15}{216.16}\right) \end{bmatrix} & 25000 < h < 47000 \\ \begin{bmatrix} -9.51 \\ P^{ref}\left(\frac{T^{est}+273.15}{282.66}\right) \end{bmatrix} & 47000 < h < 53000 \\ \begin{bmatrix} -9.51 + 0.0045(h - 53000) \\ P^{ref}\left(\frac{T^{est}+273.15}{282.66}\right) \end{bmatrix} & 53000 < h < 79000 \\ \begin{bmatrix} -107.49 \\ P^{ref}\left(\frac{T^{est}+273.15}{165.66}\right) \end{bmatrix} & 79000 < h < 90000 \\ \begin{bmatrix} -107.49 + 0.004(h - 90000) \\ P^{ref}\left(\frac{T^{est}+273.15}{165.66}\right) \end{bmatrix} & 90000 < h \end{cases} \quad (8)$$

3 RESULTS AND DISCUSSION

Figure 3 shows the data recorded in the external memory in a road trip, i.e., rate of data recording, pressure, temperature, role, pitch, yaw, three components of acceleration vector, altitude, latitude and longitude. This Figure shows that this smartphone records about 25 data in external memory every second in its normal activity mode. Increasing the data logging rate increases power consumption and reduces the time available to experience a fully charged battery. This is the average value measured by the speed sensor and the data received from the GPS unit. As mentioned earlier, the speed of measuring values by the sensor is about 200 samples per second in the normal activity mode of the smartphone used. However, the speed (and accuracy) of receiving data from a GPS unit depends on the number of visible satellites. As the number of visible satellites during the flight varies from 4 to 12, the rate (as well as the accuracy) is low in some locations. There is apparently reasonable agreement between the values

recorded for pressure altitude and temperature. It agreed on the dependence of pressure and temperature on altitude.

Figure 4 shows the *x-y* plot obtained for this trip. A satellite image is applied to the background. The *x-y* plot taken in the NED coordinate system exactly matches the path on the map. This proves the validity of this method.

Common navigation applications map your trip by comparing GPS data of your location and pre-recorded values for each point on the map. This study is not an exploratory method test. This paper presents a new and simple method to analyze the motion of moving objects. For this purpose, smartphones are a cheap combination of expensive sensors. This study confirms this ability.

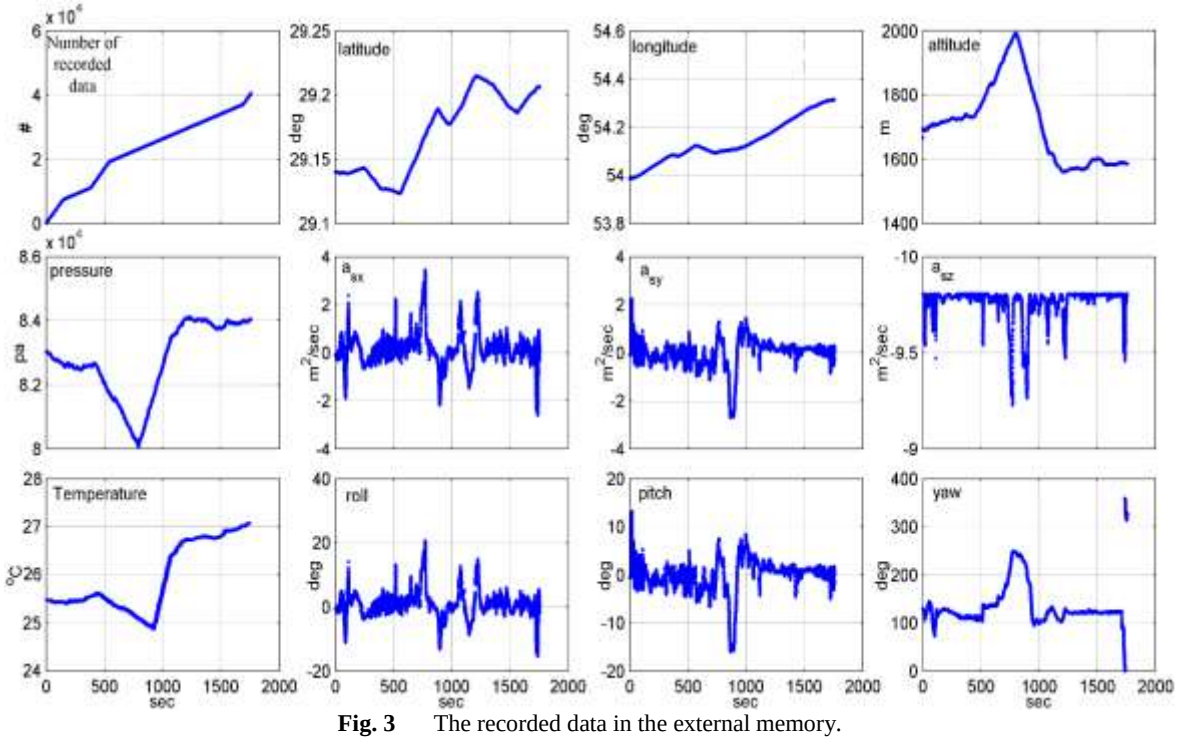

Fig. 3 The recorded data in the external memory.

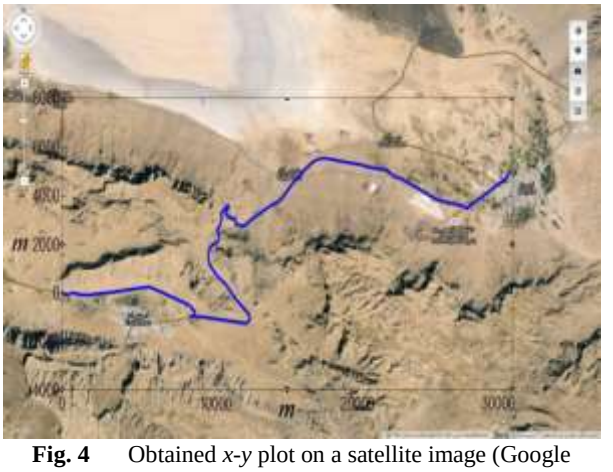

Fig. 4 Obtained *x-y* plot on a satellite image (Google Maps).

In geodetic measurements, a distance between two points can be calculated using the length of a straight line that connects these two points ($d = \sqrt{x_n^2 + y_n^2 + z_n^2}$) or using the length of the existed road between these two points ($d_t = \sum d$). Figure 5 compares these values in the road trip test. Comparing d_t with d clears that the mazes of the road increase the mentioned distance. The slopes of this curve show the mean value for the car speed (about 90 *km/hr*). The instantaneous car speed vector has been presented in "Fig. 6". These two values have been calculated based on the GPS data. Attending to the forward motion of the car, it was expected that V_{sy} and V_s would be similar, except in some climbing or turning around cases.

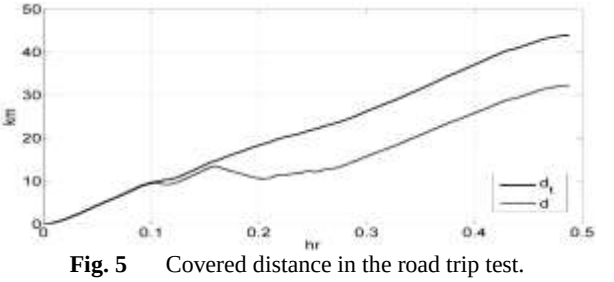

Fig. 5 Covered distance in the road trip test.

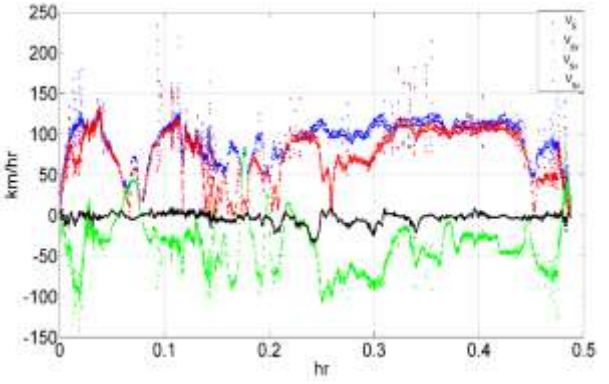

Fig. 6 Instantaneous speed in the road trip test.

Figure 7 compares the uncorrected and corrected values of the measured accelerations. It is observed that the corrected a_{sz} is smaller than the corrected values of a_{sx} and a_{sy}, attending to the low acceleration of the car in the vertical direction in this road test. Figure 8 compares $a_{GPS} = d^2(d_t)/dt^2$ with $a_{Accelerometer} = (a_{sx}^{cor2} + a_{sy}^{cor2} + a_{sz}^{cor2})^{0.5}$, which are near together, occasionally. Nevertheless, the noisy GPS data have low accuracy for calculating the acceleration. Therefore, obtaining a location using the GPS and obtaining acceleration using accelerometer sensor are more accurate.

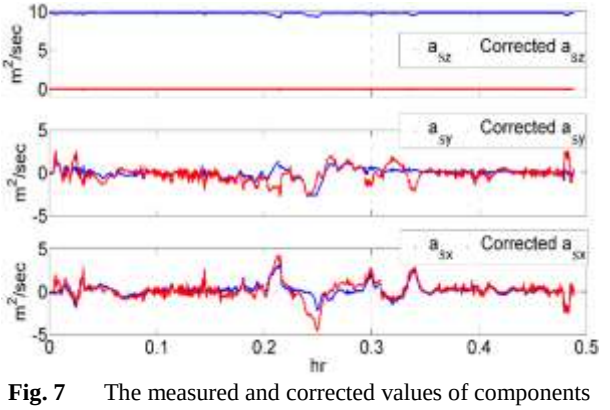

Fig. 7 The measured and corrected values of components of acceleration vector (using accelerometer sensor).

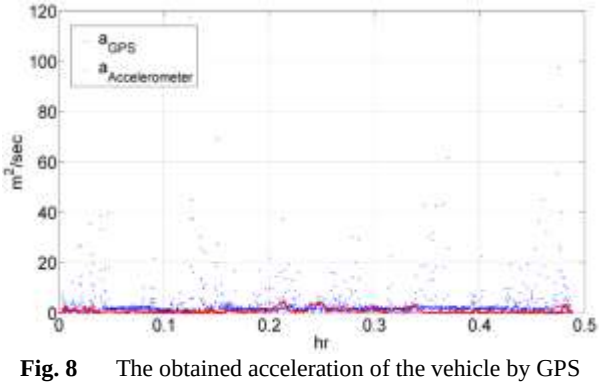

Fig. 8 The obtained acceleration of the vehicle by GPS and Accelerometer sensor.

Temperature and pressure are two valuable parameters for analyzing the performance of vehicles. The influence of the atmospheric conditions on the performance of a vehicle was studied previously [17]. It is resulted that this performance to be more affected by changes in the atmospheric pressure than in the temperature. In addition, effect of the atmosphere on the performances of aviation turbine engines were investigated [18]. In the open cabin vehicles, such as multirotor, bicycle or the used car, the sensed values of these parameters are equal to outside values. The outside values are usable for investigating the performance of multirotor propellers or a car's motor. This is a simple method for validating estimating Equations for these values. Figures 9 and 10 compare the measured temperature and pressure using the external thermometer and smartphone's pressure sensors, respectively, with the estimated values using Equation (8). A low variation of altitude in this road trip caused low variation in these two parameters. Nevertheless, there are acceptable accordance between these values and their estimations. This comparison gives valuable information in a long travel using a jet airplane, which compares the indoor and outdoor environments of a close cabin. These parameters have different values for inside and outside closed cabins. The sensors measure the inside values and the outside values are estimated using suitable Equations. The differences between the inside and outside values obtain the entered stresses on the physical structure of cabins.

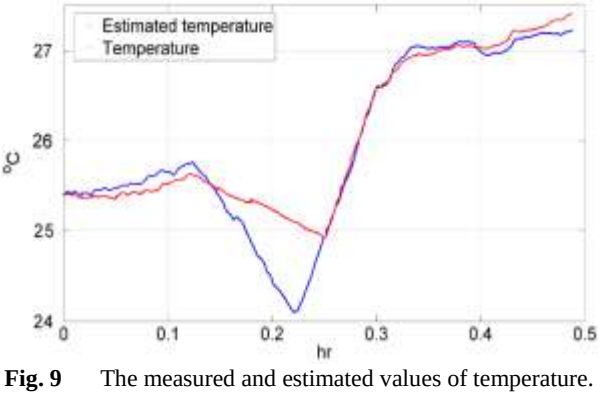

Fig. 9 The measured and estimated values of temperature.

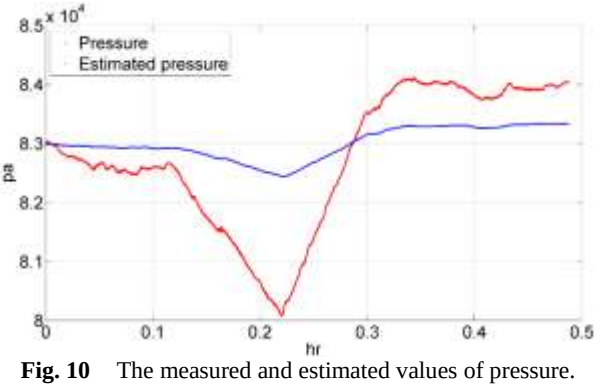

Fig. 10 The measured and estimated values of pressure.

4 CONCLUSIONS

In this study, a novel method for objects motion analyzing was defined. A JavaScript code was developed as an Android application that was installed on a smartphone to record the measured values by its sensors. In addition, a MATLAB homemade code was developed to analyze a road trip test using a car. Several coordinate transformations were utilized for this purpose. The effects of the gravitational acceleration were removed from the measured accelerations. It is observed that the obtained *x-y* plot had been matched on the road. It is concluded that the integration or differentiation improves the noises effects in the obtaining of the car location and acceleration using the accelerometer sensor and GPS unit of the smartphones, respectively. Considering low variation of altitude in this road trip, there was acceptable accordance between the measured and estimated values of temperature and pressure.

REFERENCES

[1] Kosse, N. M., Caljouw, S., Vervoort, D., Vuillerme, N., and Lamoth, C. J., Validity and Reliability of Gait and Postural Control Analysis Using the Tri-Axial Accelerometer of the iPod Touch, Annals of Biomedical Engineering, Vol. 43, 2015, pp. 1935-1946, Doi: 10.1007/s10439-014-1232-0.

[2] Muro-de-la-Herran, A., Garcia-Zapirain, B., and Mendez-Zorrilla, A., Gait Analysis Methods: an Overview of Wearable and Non-Wearable Systems, Highlighting Clinical Applications, Sensors, Vol. 14, No. 2, 2014, pp. 3362-3394, DOI: 10.3390/s140203362.

[3] Milani, P., Coccetta, C. A., Rabini, A., Sciarra, T., Massazza, G., and Ferriero, G., Mobile Smartphone Applications for Body Position Measurement in Rehabilitation: A Focus on Goniometric Tools, Physical Medicine and Rehabilitation, Vol. 6, No. 11, 2014, pp. 1038-1043, DOI: 10.1016/j.pmrj.2014.05.003.

[4] Mourcou, Q., Fleury, A., Franco, C., Klopcic, F., and Vuillerme, N., Performance Evaluation of Smartphone inertial Sensors Measurement for Range of Motion, Sensors, Vol. 15, No. 9, 2015, pp. 23168-23187, DOI: 10.3390/s150923168.

[5] Verghese, J., Holtzer, R., Lipton, R. B., and Wang, C., Quantitative Gait Markers and Incident Fall Risk in Older Adults, Journals of Gerontology Series A: Biological Sciences and Medical Sciences, Vol. 64, No. 8, 2009, pp. 896-901, DOI: 10.1093/gerona/glp033.

[6] Zhao, Y., Mobile Phone Location Determination and Its Impact on Intelligent Transportation Systems, IEEE Transactions on Intelligent Transportation Systems, Vol. 1, No. 1, 2000, pp. 55-64, DOI: 10.1109/6979.869021.

[7] Weiland, R., Purser, L., Intelligent Transportation Systems, Transportation Research, Vol. 1, 2009, pp: 40-53.

[8] Xia, H., Qiao, Y., Jian, J. and Chang, Y., Using Smart Phone Sensors to Detect Transportation Modes, Sensors, Vol. 14, No. 11, 2014, pp. 20843-20865, DOI: 10.3390/s141120843.

[9] Kalra, N., Bansal, D., Analyzing Driver Behavior Using Smartphone Sensors: a Survey, International Journal of Electronic and Electrical Engineering, Vol. 7, No. 7, 2014, pp. 697-702.

[10] Thompson, C., White, J., Dougherty, B., Albright, A., and Schmidt, D.C., Using Smartphones to Detect Car Accidents and Provide Situational Awareness to Emergency Responders, Mobile Wireless Middleware, Operating Systems and Applications, Vol. 48, 2010, pp. 29-42, DOI: 10.1007/978-3-642-17758-3_3.

[11] Abolpour, B., Abolpour, R., and Hekmatkhah R., GPS-Independent Navigation Using Smartphone Sensors, SN Applied Sciences, Vol. 1 No. 11, 2019, pp. 1-9, DOI: 10.1007/s42452-019-1401-8.

[12] El-Rabbany, A. D., Coordinate Systems, and Map Projections, London, England: Artech House Publishers, 2002, pp. 47-68.

[13] Cai, G., Chen, B. M., and Lee, T. H., Coordinate Systems and Transformations, In Unmanned Rotorcraft Systems; London, England: Springer-Verlag, 2011, pp. 23-34, DOI: 10.1007/978-0-85729-635-1_2.

[14] Cook, M. V., Systems of Axes and Notation, Oxford, England: Elsevier, 2013, pp. 13-32, DOI: 10.1016/B978-0-08-098242-7.00002-X.

[15] Serway, R. A., Jewett, J. W., Universal Gravitation. Boston, USA: Brooks Cole, 1999, pp. 388-416.

[16] Champion, K. S. W., Cole, A. E., and Kantor, A. J., Standard and Reference Atmospheres, USA: Air Force Geophysics Laboratory, 1985, pp. 1-43.

[17] Soares, S. M. C., Sodre, J. R., Effects of Atmospheric Temperature and Pressure on the Performance of a Vehicle, Proceedings of the Institution of Mechanical Engineers Part D: Journal of Automobile Engineering, Vol. 216, No. 6, 2002, pp, 473-477, DOI: 10.1243/09544070260137499.

[18] Balicki, W., Glowacki, P., Szczecinski, S., Chachurski, R., and Szczecinski, J., Effect of the Atmosphere on the Performances of Aviation Turbine Engines. Acta Mechanica et Automatica, Vol. 8, No. 2, 2014, DOI: 10.2478/ama-2014-0012.